IDŐJÁRÁS

QUARTERLY JOURNAL
OF THE HUNGARIAN METEOROLOGICAL SERVICE

CONTENTS

IDŐJÁRÁS

Quarterly Journal of the Hungarian Meteorological Service

IDŐJÁRÁS

Long-term relationships between air flow indices and air temperature over Southeast Poland

Krzysztof Bartoszek

Department of Meteorology and Climatology,
Maria Curie-Sklodowska University in Lublin
Postal address: Al. Krasnicka 2D, 20-718 Lublin, Poland
E-mail:k.bartoszek@umcs.pl

Abstract—This paper concerns the relationships between selected circulation indices and air temperature over Southeast Poland between 1871-2010. The geostrophic wind speed and the resultant vorticity were computed based on daily gridded fields of mean sea-level pressure over an area defined from 5°20' to 40°20'E and from 41°15' to 61°15'N. The highest daily mean geostrophic wind speed over Southeast Poland is observed from December to February. In turn, the maximum (positive) values of the resultant vorticity occur in April and May, while the minimum (negative) values are observed in January. Mean air temperature from November to February has a strong positive correlation with the geostrophic wind speed. Moreover, the occurrence of the highest coefficients regarding the correlation between the geostrophic wind speed and air temperature in winter as well as the NAO index was recorded at the beginning of the 21st century. This suggests that the range of impact of sea-level pressure distribution over the North Atlantic on the winter air temperature over Southeast Poland may have increased over the last decades. One of the causes may be an eastward shift of the position of the center of the Icelandic Low and the Azores High in the period from December to February.

Key-words: geostrophic flow, resultant vorticity, air temperature, NAO index, Southeast Poland

1. Introduction

One of the primary factors affecting climate is the large-scale atmospheric circulation that develops as a result of uneven distribution of solar radiation, the Earth's rotation, and interactions between the atmosphere and geosphere (*Klavins* and *Rodinov*, 2010). It determines the spatial distribution of air temperature and humidity, cloudiness, or precipitation among others. Therefore,

it largely influences the weather conditions over a given area (*Post et al.*, 2002). A particularly high variability of weather patterns is observed at the European mid-latitudes – i.e., in the region where polar air masses collide with arctic or tropical air masses (*Sepp* and *Jaagus*, 2002). Over a longer time span, the character of atmospheric circulation is also subject to changes, as demonstrated by the results of research carried out by many authors (e.g., *Bárdossy* and *Caspary*, 1990; *Kyselý* and *Huth*, 2006; *Rogers*, 1990; *Slonosky et al.*, 2000).

Large-scale atmospheric circulation can be described, among others, by means of physical parameters, including the geostrophic wind speed and the resultant vorticity (*Maraun et al.*, 2010). These circulation indices can be useful tools for the determination of both the annual and interannual variability of air flow strength as well as cyclonic and anticyclonic circulation activity in a given area (*Conway et al.*, 1996; *Flocas et al.*, 2001). The relationship between the synoptic scale air flow strength and the resultant vorticity including air temperature as well as precipitation has been analyzed a number of times (*Brandsma* and *Buishand*, 1997; *Kilsby et al.*, 1998; *Wilby*, 1999). The circulation indices under discussion can be calculated based on the values of mean sea-level pressure and have been deemed applicable and useful in the classification of circulation types (*Chen*, 2000; *Linderson*, 2001; *Post et al.*, 2002; *Trigo* and *Da Camara*, 2000).

The climate of Poland is largely determined by the physical properties of air masses, inflowing from the west (from the Atlantic Ocean), east (from the Eurasian continent), north (from the Arctic), and south (from the Mediterranean Sea or North Africa). In addition to the direction of the air flow, weather conditions in this part of Europe can also be affected by air flow speed. Polish climatological literature analyzes the correlation between the geostrophic wind speed, among others, with air temperature (*Degirmendžić et al.*, 2002), precipitation (*Miętus*, 1996), snow cover (*Nowosad*, 2012), as well as water level fluctuations along the southern Baltic Sea Coast (*Olechwir*, 2008). However, no detailed studies exist so far concerning long-term changes in the geostrophic wind speed and vorticity, and its relationships with air temperature on a centennial time-scale over South-East Europe. Such an analysis may prove to be highly significant, because it could be used in research on climate change in this part of the continent.

The objective of this paper is to provide a comprehensive determination of the annual and interannual variability of the geostrophic wind speed and vorticity over the area of Southeast Poland, and an assessment of the strength of the correlation between the circulation indices and air temperature between 1871 and 2010.

2. Material and methods

Circulation indices over Southeast Poland were calculated on the basis of equations adapted from *Jenkinson* and *Collison* (1977). In this paper, daily gridded fields (5° × 5° longitude-latitude) of mean sea-level pressure (MSLP) were used over an area centered at 51°15'N and 22°50'E (*Fig. 1*). MSLP values covered the period from 1871 to 2010, and were obtained from the Twentieth Century Reanalysis version 2 (20CRv2). The historical reanalysis dataset generated by NOAA Earth System Research Laboratory and the University of Colorado CIRES is a comprehensive global atmospheric circulation dataset spanning 1871–2010, assimilating only surface pressure and using monthly Hadley Center SST and sea ice distributions (HadISST1.1) as boundary conditions (*Compo et al.*, 2011). It should be mentioned that there may be data quality issues in the nineteenth century, but this problem is also implicit in the early gridded chart products (*Jones et al.*, 2013). Therefore, prior to 1950, measured trends in the 20CR data should be treated with caution (*Brönnimann et al.*, 2013; *Bett et al.*, 2017). However, the time series of seasonal geostrophic wind speeds derived from the observations and from 20CR are in good agreement starting in 1893 (*Wang et al.*, 2013).
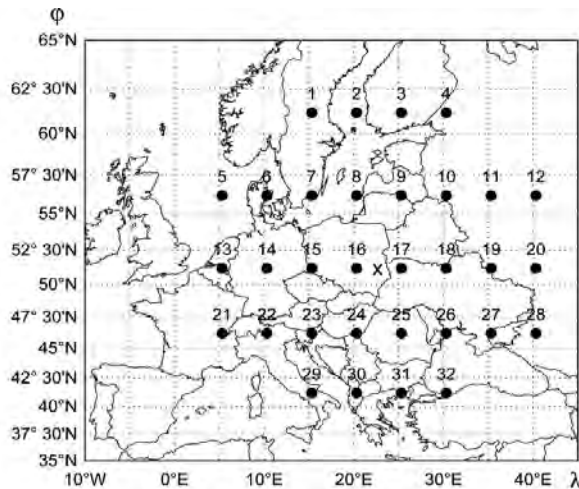

Fig. 1. Location of grid points centered over the Lublin Region (central point at 51°15'N and 22°50'E). The numbers refer to the grid points used in the equations.

The geostrophic flow (F) was calculated on the basis of two air flow indices – i.e., westerly flow (W) and southerly flow (S):

$$W = 0.25 \times (p_{23} + p_{24} + p_{25} + p_{26}) - 0.25 \times (p_7 + p_8 + p_9 + p_{10}), \tag{1}$$

$$S = 1.596[0.125 \times (p_{10} + 2 \times p_{18} + p_{26} + p_9 + 2 \times p_{17} + p_{25}) - 0.125 \times (p_7 + 2 \times p_{15} + p_{23} + p_8 + 2 \times p_{16} + p_{24})], \tag{2}$$

$$F = \sqrt{W^2 + S^2}. \tag{3}$$

The direction of the geostrophic flow was determined for days on which $F > 2$ ms^{-1}:

$$D = \arctan(S/W), \quad \text{if } W \leq 0, \tag{4}$$

$$D = \arctan(S/W) + 180, \quad \text{if } W > 0. \tag{5}$$

The resultant vorticity (Z) was calculated on the basis of zonal shear vorticity (ZW) and meridional shear vorticity (ZS):

$$ZW = 1.079 \times [0.25 \times (p_{29} + p_{30} + p_{31} + p_{32}) - 0.25 \times (p_{15} + p_{16} + p_{17} + p_{18})] - 0.938 \times [0.25 \times (p_{15} + p_{16} + p_{17} + p_{18}) - 0.25 \times (p_1 + p_2 + p_3 + p_4)], \tag{6}$$

$$ZS = 1.273 \times [0.125 \times (p_{12} + 2 \times p_{20} + p_{28} + p_{11} + 2 \times p_{19} + p_{27}) - 0.125 \times (p_{10} + 2 \times p_{18} + p_{26} + p_9 + 2 \times p_{17} + p_{25})] - 1.273 \times [0.125 \times (p_8 + 2 \times p_{16} + p_{24} + p_7 + 2 \times p_{15} + p_{23}) - 0.125 \times (p_6 + 2 \times p_{14} + p_{22} + p_5 + 2 \times p_{13} + p_{21})], \tag{7}$$

$$Z = ZW + ZS. \tag{8}$$

The coefficients in the formulas differ from those used by *Jenkinson* and *Collison* (1977), as the latitude is different. The grid points from p_1 to p_{32} correspond to the sea-level pressure values (hPa). The flow units (F) are geostrophic, expressed as hPa per 10° latitude at the central latitude (51°15'N); each unit is equivalent to 0.62 ms^{-1}. It should be note that the geostrophic wind direction does not always correspond to real air flow direction near the surface. The resultant vorticity (Z) units are expressed as hPa per 10° latitude at the central latitude (51°15'N), per 10° latitude; 1 unit is equivalent to 0.7 x 10^{-6} s^{-1}.

The monthly and seasonal North Atlantic Oscillation Index from 1871 to 2010 (*Jones et al.*, 1997) was applied to evaluate the correlations between the strength of the zonal flow over Southeast Poland and the North Atlantic

Ocean. The NAO index is defined as the difference between the normalized sea-level pressure over Gibraltar and Southeast Iceland. In order to determine the correlations between the air circulation indices and thermal conditions in the analyzed area, a long-term homogeneous series of mean monthly temperature measurements in Puławy was applied (*Górski* and *Marciniak*, 1992). Dataset after the 1980s were obtained from the Polish Institute of Meteorology and Water Management (IMGW-PIB). The meteorological station is located in Southeast Poland ($\varphi=51°25'N$, $\lambda=21°58'E$, $h=142$ m a.s.l.), and belongs to the Institute of Soil Science and Plant Cultivation in Puławy.

In order to identify periods manifesting an increased or reduced strength of correlation between the variables, correlation coefficients were determined for each of the subsequent 30-year periods within the period from 1871 to 2010.

3. Results

3.1. Frequency distributions and annual variability of air flow indices

In the period from 1871 to 2010, the daily mean geostrophic wind speed over Southeast Poland ranged from 3 to 6 ms^{-1} in the majority of cases (*Fig. 2a*). The lowest values ($F <1$ ms^{-1}) occurred over 9 days in a year on average, while the highest ($F \geq 15$ ms^{-1}) would occur over 5 days in a given year (*Fig. 2a*). In the case of daily mean resultant vorticity, the distribution of days was distinguished by an occurrence of the maximum in the domain of negative vorticity values (*Fig. 2b*). The contribution of days with negative and positive vorticity values over Southeast Poland amounted to 67.2% and 32.8%, respectively, whereas 10.9% corresponded to days with a stronger anticyclonic circulation ($Z < -15 \times 10^{-6}s^{-1}$), and only 3.6% to a stronger cyclonic circulation ($Z \geq 15 \times 10^{-6}s^{-1}$).

Over Southeast Poland, the highest daily mean geostrophic wind speed ($7 \leq F <9$ ms-1) is recorded from December to February (Fig. 3a). This results from the occurrence of large horizontal air pressure gradients in the North Atlantic/European sector at this time of the year. Additionally, in winter, a higher variability in the monthly mean geostrophic wind speed is observed on the annual scale (Fig. 4a). From the beginning of March until the end of the summer season, the daily mean geostrophic wind speed rapidly decreases, and the minimum occurs from June to August ($F \approx 4.0$ ms-1), when monthly mean values do not reach the lowest value from January (Fig. 4a).
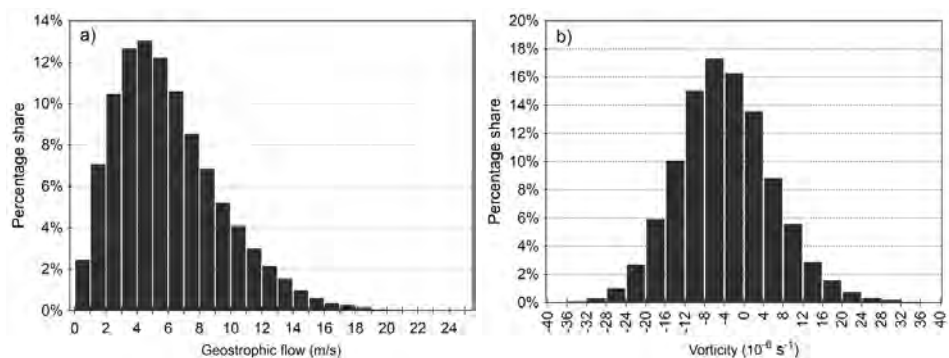
Fig. 2. Frequency distributions of daily mean values of (a) the geostrophic wind speed and (b) the resultant vorticity over Southeast Poland from 1871 to 2010.

Variability in daily mean vorticity values over Southeast Poland is distinguished by its irregularity during the course of a year (*Fig. 3b*). Their minimum occurs in the middle of January, while they peak from April to May. The second annual minimum of daily mean vorticity occurs from September to October, followed by an increase in the values towards those recorded in summer (*Fig. 3b*). Similarly as in the case of the geostrophic wind speed, the highest variability of monthly mean vorticity values over Southeast Poland is observed in winter, and the lowest in summer (*Fig. 4b*).
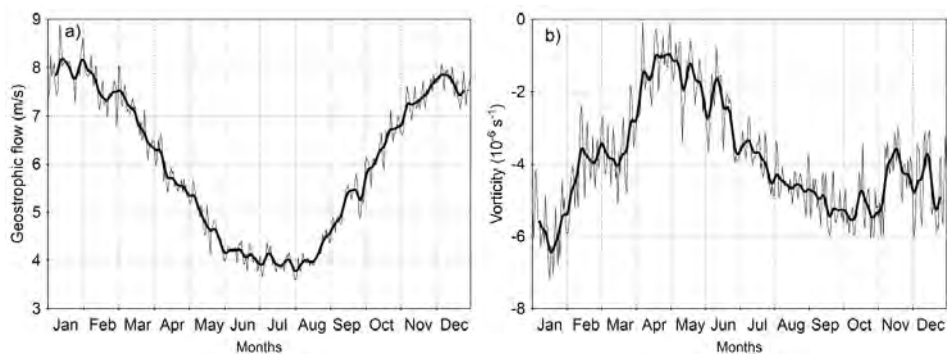
Fig. 3. Annual course of the daily mean (a) geostrophic wind speed and (b) resultant vorticity values over Southeast Poland in the period 1871–2010.
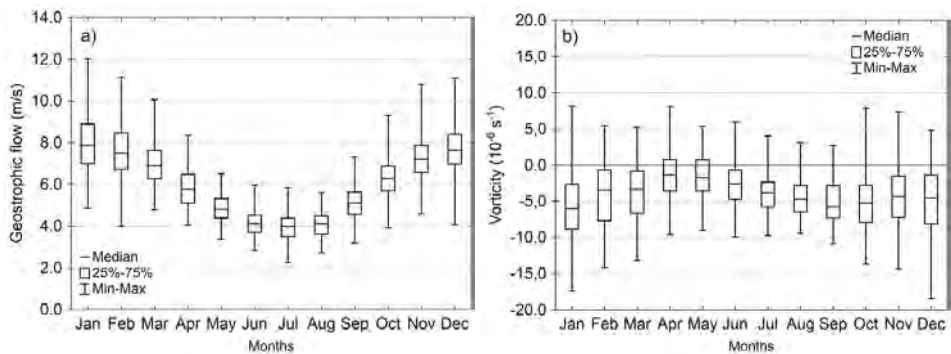
Fig. 4. Features of the empirical distribution of the monthly mean (a) geostrophic wind speed and (b) resultant vorticity values over Southeast Poland in the period 1871–2010.

3.2. *Interannual variability of air flow indices over Southeast Poland*

In winter, the highest mean geostrophic wind speed values were recorded in the years 1896–1910 and at the turn of the 1980's and 1990's, whereas the lowest was noted between 1963 and 1970 (*Fig. 5*). In spring, higher values occurred at the end of the 19th century and at the turn of the 1930's and 1940's, with lower figures in the 1920's and 1950's, as well as in the first decade of the 21st century. In summer, mean air flow speed often reached low values in the last three decades; the absolute minimum was recorded in 2000 ($F = 3.1$ ms^{-1}). In autumn, no occurrence of longer periods with higher or lower wind speed was recorded. In the case of annual means, higher values were the most evident in the first decade of the 20th century, whereas they were lower in the 1960's, (*Fig. 5*). In the period from 1871 to 2010, the highest mean annual value was recorded in 1993 ($F = 6.7$ ms^{-1}), and the lowest in 1982 ($F = 5.3$ ms^{-1}).

The lowest mean vorticity values in winter occurred between 1925 and 1934, and from the end of the 1980's to the beginning of the 21st century (Fig. 6). In spring, the minimum occurred in the period 1942-1969, with the maximum occurring at the turn of the 19th and 20th century. In summer and autumn, as well as annually, the highest mean vorticity values (intensified cyclonic circulation) were recorded between 1900 and 1915. Out of all of the analyzed years, the highest mean annual vorticity value was recorded in 2010 ($Z = -0.8 \times 10^{-6}$s^{-1}). The maximum for May and November also occurred in the same year ($Z = 5.3 \times 10^{-6}$s^{-1} and 7.4×10^{-6}s^{-1}, respectively). The lowest annual mean was recorded in 1961 ($Z = -7.4 \times 10^{-6}$s^{-1}). The minimum for the summer period was also recorded for that year ($Z = -7.5 \times 10^{-6}$s^{-1}).
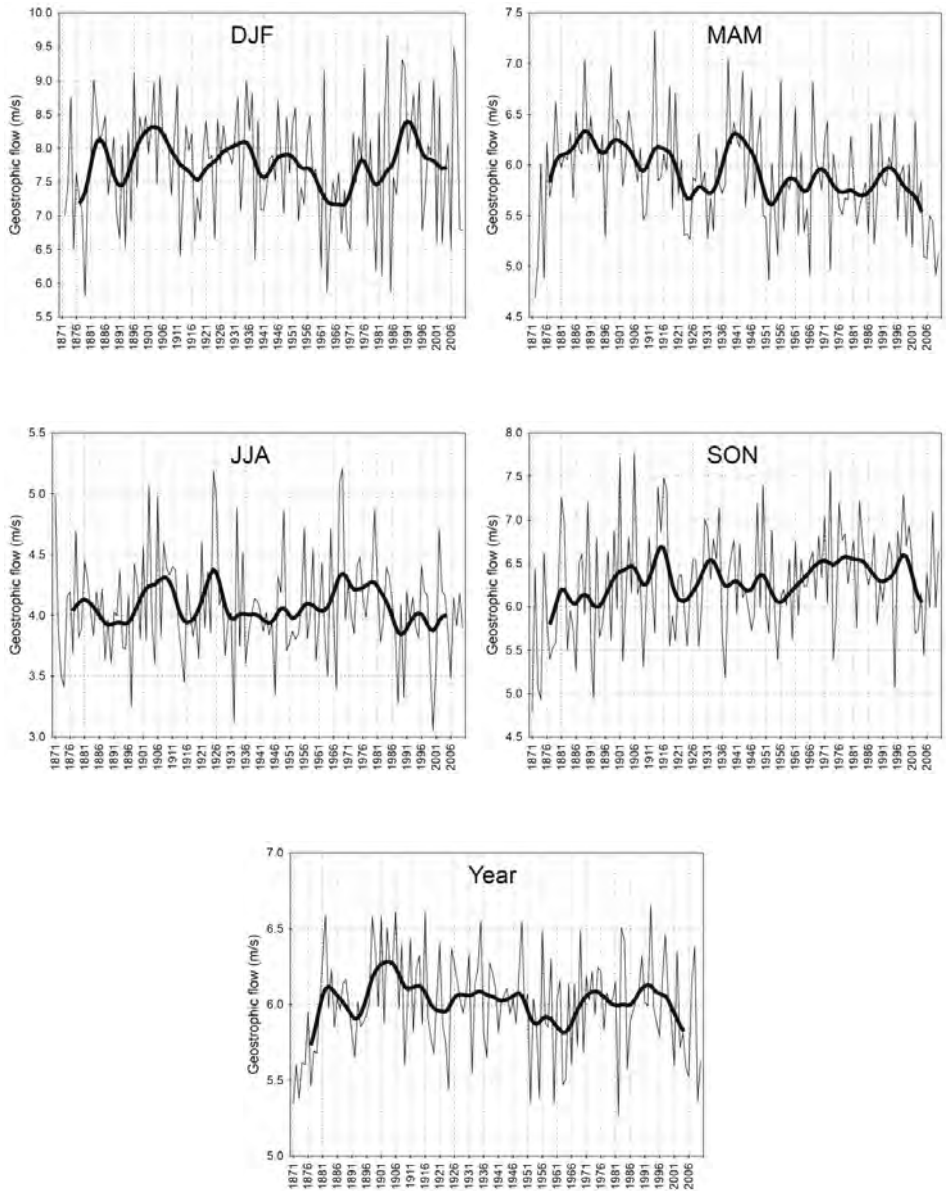
Fig. 5. Long-term variability of the mean values of the geostrophic wind speed in winter (DJF), spring (MAM), summer (JJA), autumn (SON), and the year. Values are smoothed by 13-element Gaussian filter (bold line).
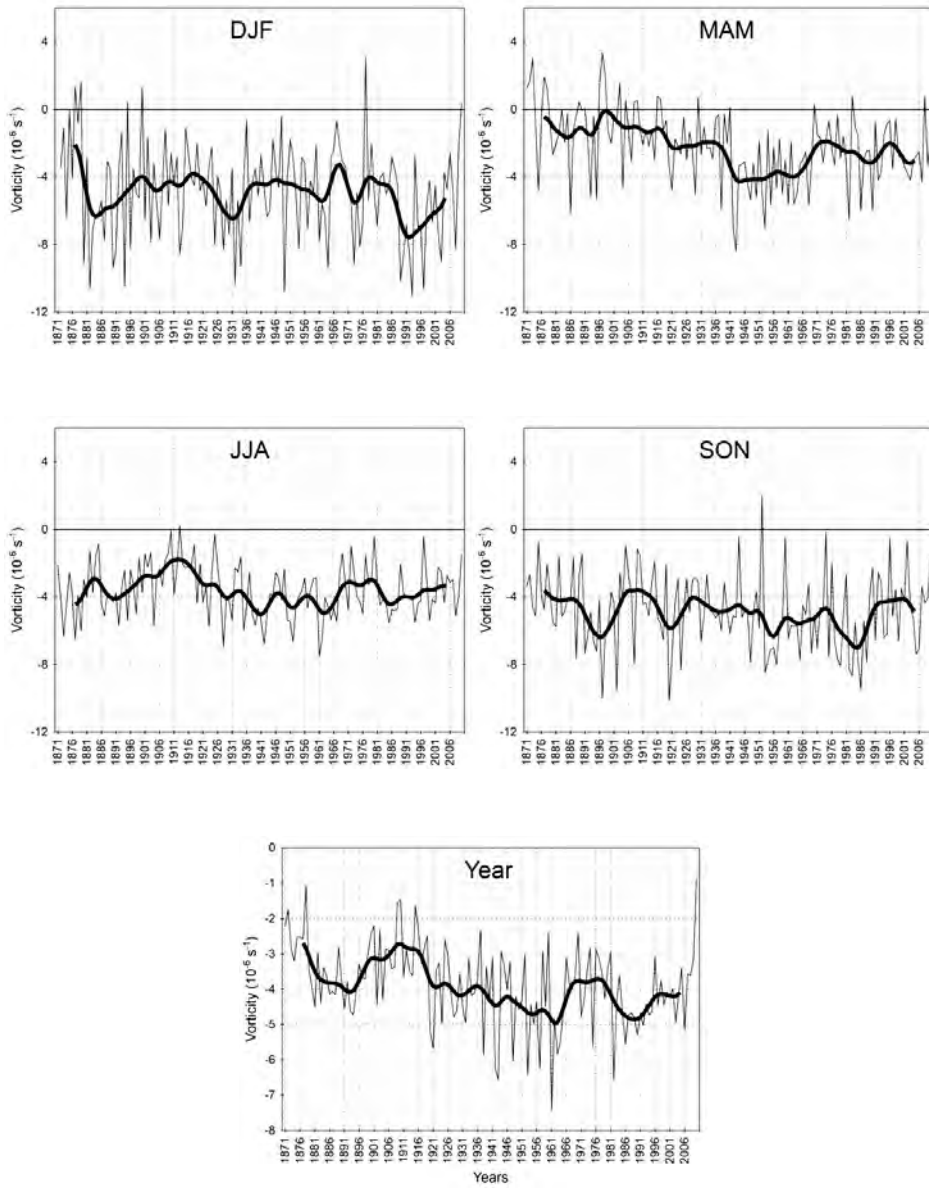
Fig. 6. Long-term variability of the mean values of the resultant vorticity in winter (DJF), spring (MAM), summer (JJA), autumn (SON), and the year. Values are smoothed by a 13-element Gaussian filter (bold line).

3.3. Relationships between air flow indices and air temperature

The mean geostrophic wind speed over Southeast Poland shows no evident correlation with mean sea-level pressure values (*Table 1*). Statistically significant correlation is recorded only in June and September – i.e., decreases (increases) in MSLP are accompanied by a stronger (weaker) air flow. Throughout the year, decreases (increases) in MSLP are accompanied by an increase (decrease) in vorticity. With the exception of the July to September period, the correlation coefficient (r) between vorticity and air pressure reaches a value of approximately –0.80 (*Table 1*).

Table 1. The linear correlation coefficients between the mean sea-level pressure and the geostrophic wind speed (*F*), as well as the resultant vorticity (*Z*) at grid point 51°15'N; 22°50'E, in the period 1871–2010

Index	Jan	Feb	Mar	Apr	May	Jun	Jul	Aug	Sep	Oct	Nov	Dec	Year
F	-0.05	-0.03	0.07	-0.08	-0.04	-0.32[a]	-0.18	-0.11	-0.24[b]	-0.14	-0.15	-0.07	0.04
Z	-0.78[a]	-0.78[a]	-0.79[a]	-0.77[a]	-0.80[a]	-0.81[a]	-0.71[a]	-0.62[a]	-0.62[a]	-0.77[a]	-0.79[a]	-0.82[a]	-0.76[a]

[a], [b] – significant at $p < 0.01$, $p < 0.05$, respectively

From October to February, a statistically significant correlation is observed in the study area between the geostrophic air flow speed and the NAO index (*Table 2*). High positive NAO index values and, therefore, the occurrence of large horizontal air pressure gradients between Gibraltar and Iceland suggest an increasing intensity of the western zonal circulation over a large part of Europe. In the case of Southeast Poland, the highest positive correlation coefficients occur in the winter months (*Table 2*). This confirms that at this time of the year, the strength of air flow over the European continent is largely determined by two centers of atmospheric activity in the Northeast Atlantic Ocean – i.e., the Icelandic Low and the Azores High.

The resultant vorticity shows a statistically significant correlation with the NAO index in all months, whereas the correlation is the strongest in the winter season (*Table 2*). A negative correlation coefficient value suggests that increases (decreases) in the air pressure gradients over the North Atlantic correspond to a strengthening of anticyclonic (cyclonic) circulation over Southeast Poland. This may result from the fact that during winters with high positive NAO index values, the Azores High pressure system is strongly extended northeastwards towards East Europe (*Fig. 7a–b*). The strengthening of anticyclonic circulation over the analysed area can also occur during winters with negative NAO index values, if the atmospheric circulation in East Europe is affected by the ridge of the Siberian High (*Fig. 7c*). However, low negative NAO index values usually correspond to the weakening of anticyclonic circulation in this part of the continent (*Fig. 7d*).

Table 2. The linear correlation coefficients between the NAO index and the geostrophic wind speed (F), as well as the resultant vorticity (Z) in the period 1871–2010

	Jan	Feb	Mar	Apr	May	Jun	Jul	Aug	Sep	Oct	Nov	Dec	Year
F	0.52[a]	0.33[a]	0.14	-0.01	-0.18	-0.07	0.16	0.03	-0.04	0.22[b]	0.24[b]	0.36[a]	0.30[a]
Z	-0.37[a]	-0.38[a]	-0.38[a]	-0.22[b]	-0.39[a]	-0.28[a]	-0.24[b]	-0.49[a]	-0.51[a]	-0.33[a]	-0.36[a]	-0.28[a]	-0.31[a]

[a], [b] – significant at $p < 0.001$, $p < 0.01$, respectively
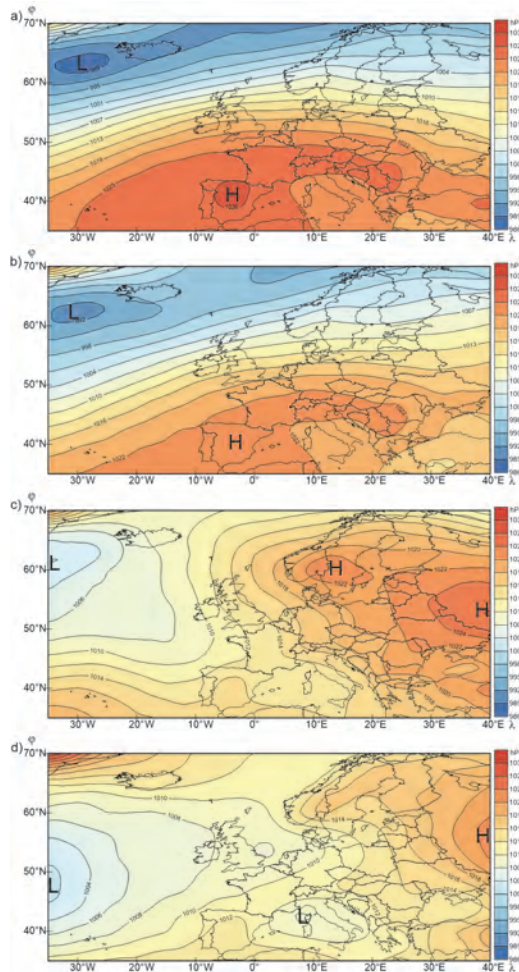
Fig. 7. Mean sea-level pressure fields from December to February at the Euro-Atlantic sector in the winter seasons of (a) 1988-89 (NAO$_{DJF}$ = +2,99), (b) 1974-75 (NAO$_{DJF}$ = +1,96), (c) 1995-96 (NAO$_{DJF}$ = –2,24), and (d) 2009-10 (NAO$_{DJF}$ = –3,12). Data from the NCEP/NCAR Reanalysis (*Kalnay et al.*, 1996).

Mean air temperature in the period from November to February has a strong positive correlation with the geostrophic wind speed (*Table 3*). As it was previously mentioned, the occurrence of large horizontal air pressure gradients over the North Atlantic in winter is responsible for the intensified western zonal circulation. Therefore, the occurrence of mild winters in Southeast Poland is determined in particular by a strong advection of relatively warm air at this time of the year from westerly and northwesterly directions – i.e., from the Atlantic Ocean (*Table 4*). In turn, a higher frequency of days with northeasterly and easterly circulation – i.e., from the cool interior of the Eurasian continent – corresponds to the occurrence of severe winters. In June, July, and September, the geostrophic wind speed is negatively correlated with air temperature (*Table 3*). At this time of the year, the temperature of the Atlantic is lower than that of the surface of the continent. Therefore, cooler summer seasons over Southeast Poland occur in tandem with an increased frequency of westerly and northwesterly circulation, whereas warmer summers are experienced if days with easterly and southeasterly circulation are prevalent (*Table 4*).

Table 3. The linear correlation coefficients between the air temperature and the geostrophic wind speed (*F*), as well as the resultant vorticity (*Z*) in the period 1871–2010

	Jan	Feb	Mar	Apr	May	Jun	Jul	Aug	Sep	Oct	Nov	Dec	Year
F	0.54[a]	0.28[a]	0.12	-0.02	0.00	-0.31[a]	-0.35[a]	-0.20	-0.28[a]	0.16	0.22[b]	0.30[a]	0.17
Z	-0.02	-0.03	-0.05	-0.05	-0.13	-0.32[a]	-0.21	-0.02	-0.27[b]	0.03	0.27[b]	0.19	-0.14

[a], [b] – significant at $p < 0.001$, $p < 0.01$, respectively

Table 4. The linear correlation coefficients between the frequency of air flow directions and the geostrophic wind speed (*F*), as well as air temperature (*T*) in winter and summer (1871–2010)

	Winter (DJF)							
	N	NE	E	SE	S	SW	W	NW
F	0.11	-0.28[a]	-0.34[a]	-0.18	-0.05	0.09	0.51[a]	0.39[a]
T	0.08	-0.36[a]	-0.62[a]	-0.45[a]	-0.02	0.48[a]	0.48[a]	0.32[a]
	Summer (JJA)							
	N	NE	E	SE	S	SW	W	NW
F	0.07	0.18	0.15	0.05	-0.11	-0.05	0.18	0.08
T	-0.18	0.09	0.34[a]	0.28[a]	0.11	-0.06	-0.31[a]	-0.34[a]

[a], [b] – significant at $p < 0.001$, $p < 0.01$, respectively

The strength of the correlation between the geostrophic wind speed in winter and the NAO index has recently been subject to a considerable change (*Fig. 8*). In each of the subsequent 30-year periods, the lowest correlation coefficients ($0.2 < r < 0.3$) occurred in the second decade of the 20th century and in the first half of the 1960's. A weak correlation was also determined from the 1930's to the 1960's between air flow speed and air temperature. In both cases, a very rapid increase in the correlation coefficient values from the 1980's to the end of the analyzed period was significant. In the first decade of the 21st century, more than 50% of the variance of the mean air temperature in winter was explained by the geostrophic wind speed. In the case of correlations between the air temperature and the winter NAO index, reasonably high correlation coefficient values ($0.6 < r < 0.7$) have been recorded since the mid 1960's (*Fig. 8*).
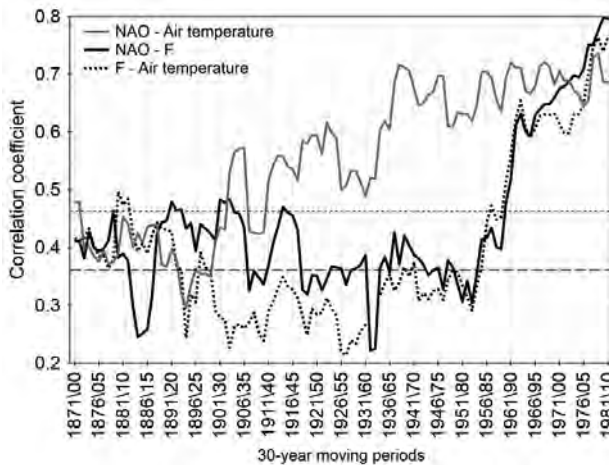
Fig. 8. Long-term variability of correlation coefficient for each of the 30-year moving periods between the geostrophic wind speed (*F*), the NAO index, and the mean air temperature in winter (DJF). Horizontal dotted lines indicate correlation significant at a *p*-value of 0.01; horizontal dashed lines at a *p*-value of 0.05.

Over recent decades, a considerable increase has been also noted in the strength of the correlation between the geostrophic wind speed and the number of days with westerly and easterly air flow in winter (*Fig. 9a* and *c*). A higher correlation than in previous years has also been recorded since the end of the 1980's between the frequency of western zonal circulation and the NAO index as well as the air temperature in winter (*Fig. 9a*). Moreover, in the 1988–2002 period, a maximum (minimum) frequency of westerly (easterly) zonal circulation in winter was recorded over Southeast Poland (*Fig. 9b* and *d*).
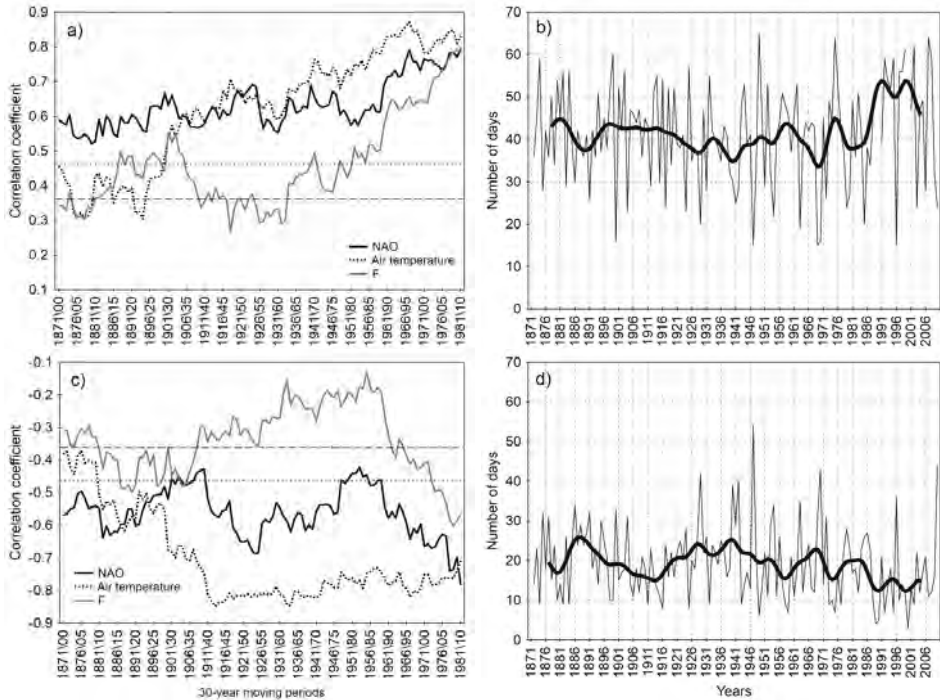
Fig. 9. Long-term variability of correlation coefficient for each of the 30-year moving periods among the geostrophic wind speed (*F*), the NAO index and the mean air temperature, and the frequency of (a) westerly (SW+W+NW) and (c) easterly air flow (NE+E+SE) in winter (DJF). Horizontal dotted lines indicate correlation significant at a p-value of 0.01; horizontal dashed lines at a p-value of 0.05. The interannual frequency of (b) westerly and (d) easterly air flow is also presented. Values are smoothed by a 13-element Gaussian filter (bold line).

4. Discussion and conclusions

The present study has revealed that the daily mean geostrophic wind speed over Southeast Poland ranged from 3 to 6 ms^{-1}. For comparison, in the area of the British Isles, the maximum frequency of days corresponded with a range of values from 6 to 7.5 ms^{-1} (*Conway et al.*, 1996). The highest values occur from December to March, and the lowest ones from June to August. In Central Europe the occurrence of the highest mean geostrophic wind speed in winter and the lowest in summer was also revealed by the results of research undertaken by *Marosz* and *Miętus* (2012) as well as *Brandsma* and *Buishand* (1998). In the case of daily mean resultant vorticity, the distribution of days over Southeast Poland and British Isles was approximate.

The first decade of the 21st century was distinguished by a lower geostrophic mean wind speed than in the 1980's and 1990's. A strengthening of the westerly zonal circulation in the final decades of the 20th century in the North Atlantic/European sector was also noted in several climatological studies (e.g., *Bárdossy* and *Caspary*, 1990; *Degirmendžić et al.*, 2000; *Keevallik et al.*, 1999; *Kyselý* and *Huth*, 2006; *Werner et al.*, 2000). Furthermore, higher annual mean values were the most evident in the first decade of the 20th century, and lower in the 1960's. Similar occurrences of maximum and minimum wind speed values were found in Switzerland (*Brönnimann et al.*, 2012). In turn, the decade of the 1960's was analyzed by *Ustrnul* (1997) and *Degirmendžić et al.* (2000). According to the studies, exceptionally weakened western zonal circulation was observed over the European continent at this time.

The highest mean values of resultant vorticity occurred at the beginning of the 20th century (a period with intensified cyclonic circulation). The evident prevalence of cyclonic over anticyclonic frequency at the beginning of the 20th century is also confirmed by the results of research conducted by *Przybylak* and *Maszewski* (2009), referring to the western area of Central Poland. On an annual scale, the maximum values of vorticity over Southeast Poland occur in April and May, and the minimum in January. Considerably weakened anticyclonic circulation in the spring season was also recorded in the eastern part of Germany (*Brandsma* and *Buishand*, 1998).

Geostrophic wind speed over Southeast Poland affects air temperature to the greatest extent during the period from December to February. This confirms the earlier results obtained for Poland by *Kożuchowski* and *Żmudzka* (2002). The warmest winters are accompanied by a greater than average number of days with westerly circulation and a stronger zonal flow. In contrast to air flow speed and direction, no clear correlations were found between vorticity and air temperature.

The highest strength of the correlation ($r = 0.80$) between the air flow speed and frequency of days with a westerly circulation as well as the NAO index values in winter has also been observed recently. This suggests that the range of impact of sea-level pressure distribution on the character of the atmospheric circulation over the North Atlantic and air temperature during winter over Southeast Poland may have increased in the recent years. One of the causes may be an eastward shift of the position of the center of the Icelandic Low and the Azores High in the period from December to February that began in the late 1970s (*Hilmer* and *Jung*, 2000; *Johnson et al.*, 2008). It was reported that the relationship between the air temperature over Eastern Europe and the winter NAO has strengthened considerably since then because of NAO-related intensified zonal flow anomalies over this region (*Jung et al.*, 2003).

References

Bárdossy, A. and *Caspary, H.J.*, 1990: Detection of climate change in Europe by analyzing European atmospheric circulation patterns from 1881 to 1989. *Theor. Appl. Climatol. 42*, 155–167. https://doi.org/10.1007/BF00866871

Bett, P.E., *Thornton, H.E.*, and *Clark, R.T.*, 2017: Using the Twentieth Century Reanalysis to assess climate variability for the European wind industry. *Theor. Appl. Climatol. 127*, 61–80. https://doi.org/10.1007/s00704-015-1591-y

Brandsma, T., and *Buishand, T.A.*, 1997: Statistical linkage of daily precipitation in Switzerland to atmospheric circulation and temperature. *J. Hydrol. 198*, 98–123. https://doi.org/10.1016/S0022-1694(96)03326-4

Brandsma, T., and *Buishand, T.A.*, 1998: Simulation of extreme precipitation in the Rhine basin by nearest neighbour resampling. *Hydrol. Earth Syst. Sci. 2*, 195–209. https://doi.org/10.5194/hess-2-195-1998

Brönnimann, S., Martius, O., von Waldow, H., Welker, C., Luterbacher J., Compo G.P., Sardeshmukh P.D., and *Usbeck T.*, 2012: Extreme winds at northern mid-latitudes since 1871. *Meteorol. Zeit. 21*, 13–27. https://doi.org/10.1127/0941-2948/2012/0337

Brönnimann, S., *Wegmann M.*, *Wartenburger R.*, and *Stickler A.*, 2013: Arctic Winds in the Twentieth Century Reanalysis. In: *Weather extremes during the past 140 years* (S. Brönnimann and O. Martius, Eds.). Geographica Bernensia G89, 59–67.

Chen, D., 2000: A monthly circulation climatology for Sweden and its application to a winter temperature case study. *Int. J. Climatol. 20*, 1067–1076. https://doi.org/10.1002/1097-0088(200008)20:10<1067::AID-JOC528>3.0.CO;2-Q

Compo, G.P., Whitaker, J.S., Sardeshmukh, P.D., Matsui, N., Allan, R.J., Yin, X., Gleason, B.E., Vose, R.S., Rutledge, G., Bessemoulin, P., Brönnimann, S., Brunet, M., Crouthamel, R.I., Grant, A.N., Groisman, P.Y., Jones, P.D., Kruk, M.C., Kruger, A.C., Marshall, G.J., Maugeri, M., Mok, H.Y., Nordli, Ø., Ross, T.F., Trigo, R.M., Wang, X.L., Woodruff, S.D., and *Worley, S.*, 2011: The Twentieth Century Reanalysis Project. *Q. J. R. Meteorol. Soc. 137*, 1–28. https://doi.org/10.1002/qj.776

Conway, D., Wilby, R.L., and Jones, P.D., 1996: Precipitation and air flow indices over the British Isles. *Clim. Res. 7*, 169–183. https://doi.org/10.3354/cr007169

Degirmendžić, J., Kożuchowski, K., and *Żmudzka, E.*, 2002: Uwarunkowania cyrkulacyjne zmienności temperatury powietrza w Polsce w okresie 1951-2000. *Prz. Geof. 47*, 93–98 (in Polish).

Degirmendžić, J., Kożuchowski, K., and *Wibig, J.*, 2000: Epoki cyrkulacyjne XX wieku i zmienność typów cyrkulacji atmosferycznej w Polsce. *Prz. Geof. 45*, 221–238 (in Polish).

Flocas, H.A., Maheras, P., Karacostas, T.S., Patrikas, I., and *Anagnostopoulou, C.*, 2001: A 40-year climatological study of relative vorticity distribution over the Mediterranean. *Int. J. Climatol. 21*, 1759–1778. https://doi.org/10.1002/joc.705

Górski, T., and *Marciniak, K.*, 1992: Temperatura powietrza w Puławach w ciągu lat 1871-1990. *Pam. Puł. 100*, 7–26 (in Polish).

Hilmer, M., and *Jung, T.*, 2000: Evidence for a recent change in the link between the North Atlantic Oscillation and Arctic sea ice export. *Geophys. Res. Lett. 27*, 989–992. https://doi.org/10.1029/1999GL010944

Jenkinson, A.F., and *Collinson, F.P.*, 1977: An initial climatology of gales over the North Sea. Synoptic climatology branch memorandum 62, Meteorological Office, Bracknell.

Johnson, N.C., Feldstein, S.B., and *Trembley, B.*, 2008: The continuum of Northern Hemisphere teleconnection patterns and a description of the NAO shift with the use of self-organizing maps. *J. Clim. 21*, 6354–6371. https://doi.org/10.1175/2008JCLI2380.1

Jones, P.D., *Jonsson, T.*, and *Wheeler, D.*, 1997: Extension to the North Atlantic Oscillation using early instrumental pressure observations from Gibraltar and South-West Iceland. *Int. J. Climatol. 17*, 1433–1450. https://doi.org/10.1002/(SICI)1097-0088(19971115)17:13<1433::AID-JOC203>3.0.CO;2-P

Jones, P.D., Harpham, C., and Briffa, K.R., 2013: Lamb weather types derived from reanalysis products. *Int. J. Climatol. 33*, 1129–1139. https://doi.org/10.1002/joc.3498

Jung, T., Hilmer, M., Ruprecht, E., Kleppek, S., Gulev, S.K., and Zolina, O., 2003: Characteristics of the recent eastward shift of interannual NAO variability. *J. Clim. 16*, 3371–3382. https://doi.org/10.1175/1520-0442(2003)016<3371:COTRES>2.0.CO;2

Kalnay, E., Kanamistu, M., Kistler, R., Collins, W., Deaven, D., Gandin, L., Iredell, M., Saha, S., White, G., Woollen, J., Zhu, Y., Leetmaa, A., Reynolds, R., Chelliah, M., Ebisuzaki, W., Higgins, W., Janowiak, J., Mo, K.C., Ropelewski, C., Wang, J., Jenne, R. and Joseph, D., 1996: The NMC/NCAR 40-Year Reanalysis Project. *Bull. Amer. Meteor. Soc. 77*, 437–471. https://doi.org/10.1175/1520-0477(1996)077<0437:TNYRP>2.0.CO;2

Keevallik, S., Post, P. and Tuulik, J., 1999: European circulation patterns and meteorological situation in Estonia. *Theor. Appl. Climatol. 63*, 117–127. https://doi.org/10.1007/s007040050097

Kilsby, C.G., Cowpertwait, P.S., O'Connell, P.E., and Jones, P.D., 1998: Predicting rainfall statistics in England and Wales using atmospheric circulation variables. *Int. J. Climatol. 18*, 523–539. https://doi.org/10.1002/(SICI)1097-0088(199804)18:5<523::AID-JOC268>3.0.CO;2-X

Klavins, M., and Rodinov, V., 2010: Influence of Large-scale Atmospheric Circulation on Climate in Latvia. *Boreal Env. Res. 15*, 533–543.

Kożuchowski, K., and Żmudzka, E., 2002: Cyrkulacja atmosferyczna i jej wpływ na zmienność temperatury powietrza w Polsce. *Prz. Geogr. 74*, 591–604 (in Polish).

Kyselý, J., and Huth, R., 2006: Changes in atmospheric circulation over Europe detected by objective and subjective methods. *Theor. Appl. Climatol. 85*, 19–36. https://doi.org/10.1007/s00704-005-0164-x

Linderson, M.J., 2001: Objective classification of atmospheric circulation over Southern Scandinavia. *Int. J. Climatol. 21*, 155–169. https://doi.org/10.1002/joc.604

Maraun, D., Rust, H.W., and Osborn, T.J., 2010: Synoptic airflow and UK daily precipitation extremes. *Extremes 13*, 133–153. https://doi.org/10.1007/s10687-010-0102-x

Marosz, M., and Miętus, M., 2012: Opis lokalnych aspektów cyrkulacji atmosferycznej za pomocą wektora wiatru geostroficznego. In: *Rola cyrkulacji atmosfery w kształtowaniu klimatu* (Z. Bielec-Bąkowska, E. Łupikasza and A. Widawski, Eds.). Uniwersytet Śląski, Sosnowiec, 89–100 (in Polish).

Miętus, M., 1996: Zmienność lokalnej cyrkulacji atmosferycznej nad północną Polską i jej związek z elementami klimatu *Wiad. IMGW 20*, 9–29 (in Polish).

Nowosad, M., 2012: Zmiany grubości pokrywy śnieżnej w Lublinie i ich uwarunkowania cyrkulacyjne. *Pr. Wydz. NoZ Uniw. Śl. 74*, 157–166 (in Polish).

Olechwir, T., 2008: Wpływ kierunku i prędkości wiatru geostroficznego na wahania poziomów wody na Zalewie Szczecińskim. *Inż. Mor. i Geotech. 29*, 52–54.

Post, P., Truija, V., and Tuulik, J., 2002: Circulation weather types and their influence on temperature and precipitation in Estonia. *Boreal Env. Res. 7*, 281–289.

Przybylak, R., and Maszewski, R., 2009: Zmienność cyrkulacji atmosferycznej w regionie bydgosko-toruńskim w latach 1881-2005. *Acta Agroph. 14*, 427–447 (in Polish).

Rogers, J.C., 1990: Patterns of low-frequency monthly sea level pressure variability (1899–1986) and associated wave cyclone frequencies. *J. Clim. 3*, 1364–1379. https://doi.org/10.1175/1520-0442(1990)003<1364:POLFMS>2.0.CO;2

Sepp, M., and Jaagus J., 2002: Frequency of circulation patterns and air temperature variations in Europe. *Boreal Env. Res. 7*, 273–279.

Slonosky, V.C., Jones, P.D., and Davies, T.D., 2000: Variability of the surface atmospheric circulation over Europe, 1774–1995. *Int. J. Climatol. 20*, 1875–1897. https://doi.org/10.1002/1097-0088(200012)20:15<1875::AID-JOC593>3.0.CO;2-D

Trigo, R.M., and Da Camara, C.C., 2000: Circulation weather types and their influence on the precipitation regime in Portugal. *Int. J. Climatol. 20*, 1559–1581. https://doi.org/10.1002/1097-0088(20001115)20:13<1559::AID-JOC555>3.0.CO;2-5

Ustrnul, Z., 1997: *Zmienność cyrkulacji atmosfery na półkuli północnej w XX wieku*. Mat. Bad. IMGW Ser. Met. *27*, Warszawa. (in Polish).

Wang, X.L., Feng, Y., Compo, G.P., Zwiers, F.W., Allan, R.J., Swail, V.R., and *Sardeshmukhet, P.D.*, 2013: Is the storminess in the Twentieth Century Reanalysis really inconsistent with observations? A reply to the comment by Krueger et al. (2013b). *Clim. Dyn. 42*, 1113–1125. https://doi.org/10.1007/s00382-013-1828-3

Werner, P.C., Gerstengarbe, F.W., Fraedrich, K., and *Oesterle, H.*, 2000: Recent climate change in the North Atlantic/European sector. *Int. J. Climatol. 20*, 463–471. https://doi.org/10.1002/(SICI)1097-0088(200004)20:5<463::AID-JOC483>3.0.CO;2-T

Wilby, R.L., 1999: Statistical downscaling of daily precipitation using daily airflow and seasonal teleconnection indices. *Clim. Res. 10*, 163–178. https://doi.org/10.3354/cr010163

IDŐJÁRÁS

Evaluation of ozone deposition models over a subalpine forest in Niwot Ridge, Colorado

Dalma Szinyei[1,2], **Györgyi Gelybó***[3], **Alex B. Guenther**[4],
Andrew A. Turnipseed[5], **Eszter Tóth**[3] and **Peter J. H. Builtjes**[6,7]

[1] *MTA-PE Air Chemistry Research Group, University of Pannonia,
Egyetem u. 10, H-8200, Veszprém, Hungary*

[2] *Department of Geology and Meteorology,
University of Pécs, Ifjúság útja 6, H-7624, Pécs, Hungary*

[3] *Institute for Soil Sciences and Agricultural Chemistry,
Centre for Agricultural Research, Hungarian Academy of Sciences,
Herman Ottó út 15, H-1022, Budapest, Hungary*

[4] *Department of Earth System Science
University of California, Irvine CA 92697, USA*

[5] *Atmospheric Chemistry Division, National Center for Atmospheric Research,
P.O. Box 3000, Boulder, CO 80307-3000, USA*

[6] *TNO Built Environment and Geosciences, Air Quality and Climate Team,
Princetonlaan 6, 3508 TA, Utrecht, The Netherlands*

[7] *Institute of Meteorology, Freie Universität Berlin,
Carl-Heinrich-Becker Weg 6-10, 12165, Berlin, Germany*

*Corresponding author E-mail: gelybo.gyorgyi@agrar.mta.hu

Abstract—In this study, we evaluated three conceptually similar ozone gas deposition models. These dry deposition models are frequently used with chemical transport models for calculations over large spatial domains. However, large scale applications of surface-atmosphere exchange of reactive gases require modeling results as accurate as possible to avoid nonlinear accumulation of errors in the spatially representative results. In this paper, model evaluation and comparison against measured data over a coniferous forest at Niwot Ridge AmeriFlux site (Colorado, USA) is carried out. At this site, no previous model calibration took place for any of the models, therefore, we can test and compare their performances under similar conditions as they would perform in a spatial application. Our results show systematic model errors in all the three cases, model performance varies with time of the day, and the errors show a pronounced seasonal pattern as well. The introduction of soil moisture content stress in the model improved model performance regarding the magnitude of fluxes, but the correlation between measured and modeled ozone deposition values remains low. Our results suggest that ozone dry deposition model results should be interpreted carefully in large scale applications, where the accuracy can vary with land cover sometimes are biased.

Key-words: ozone fluxes, deposition model, big leaf models, coniferous forest

1. Introduction

Air quality monitoring and modeling is important not only to quantify the environmental stress on human health but also to understand the impact on terrestrial ecosystems. Many relevant studies, using field measurements and/or model results, have reported that tropospheric ozone can influence the health of the ecosystem (namely, *Fares et al.,* 2013; *Loreto* and *Fares,* 2007). Ozone (O_3) like some other trace gases passes through the stomata into the mesophyll cells of plants and is toxic since it reacts with the liquid components of the apoplast to create reactive oxygen species (*Fares et al.,* 2013). These can oxidize the cell walls to start a cascade of reactions which lead, at the final stage, to cellular death (*Fares et al.,* 2013). *Karnosky et al.* (2003; 2005) reported significant ecosystem scale responses to elevated carbon dioxide (CO_2) and O_3 levels in the Aspen FACE Experiment. The changes were reflected in several ecosystem properties, including photosynthesis. Their results suggest that elevated O_3 at relatively low concentrations can significantly reduce the growth enhancement by elevated CO_2.

As forests can be long-term sinks of carbon (*Pan et al.,* 2011), they play a key role in terrestrial ecosystem-atmosphere interactions. Any productivity changes caused, e.g., by detrimental effects of the ozone can have serious effects on atmospheric CO_2 concentrations as well (*Ashmore*, 2005; *Klinberg et al.,* 2011). *Anav et al.* (2011) investigated the effects of tropospheric O_3 on photosynthesis and leaf area index on European vegetation using a land surface model (ORCHIDEE) coupled with a chemistry transport model (CHIMERE). Their results showed that the effect of ozone on vegetation leads to a reduction in yearly gross primary productivity (*GPP*) of about 22% and a reduction in leaf area index (*LAI*) of 15–20%. Decrease in GPP probably becomes more acute due to the harmful effect of tropospheric ozone. Based on high methane level scenarios (RCP8.5, SRES A2) (*Kirtman et al.,* 2013), it is predicted that background surface ozone will increase about 8ppb on average by 2100 (25% of current levels) relative to scenarios with small methane changes (RCP4.5, RCP6.0). Background tropospheric ozone concentration in the northern hemisphere is recently in the range of 35–40 ppb (*Fowler et al.,* 2008). The resulting indirect radiative forcing of ozone via its effects on ecosystems could contribute to global warming. Based on a recent estimation, 2–8% of the radiative forcing of CO_2 between 1900 and 2004 can be attributed to the indirect effect of ozone (*Kvalevåg* and *Myhre,* 2013). Therefore, investigation of ozone deposition is of high relevance.

Although there is a global network of measurement sites (Ameriflux, Asiaflux, Euroflux) aiming at monitoring of fluxes of CO_2, a major greenhouse gas, this is not the case with other trace gas flux and deposition measurements, where – especially continuous long-term – measurements are not common. For research aiming at the quantification of tropospheric ozone-climate feedbacks,

reliable large scale information is required on ozone deposition. Besides direct flux measurements with limited availability and spatial representation, modeling efforts are of high importance, since they integrate field measurements of ozone concentration and fluxes to give a reliable estimation on ozone effects on ecosystems. Various 3-dimensional chemical transport models (CTMs) (e.g., AURAMS (*Smyth et al.,* 2009), CAMx (*Emery et al.,* 2012), CHIMERE (*Menut et al.,* 2013), EMEP MSC-W (*Simpson et al.,* 2012), GEOS-CHEM (*Bey et al.,* 2001), LOTOS-EUROS (*Schaap et al.,* 2008), OFIS (*Moussiopoulos* and *Douros,* 2005), RCG (RemCalGrid) (*Stern*, 2009), TAMP (*Hurley,* 2008), WRF-CHEM (*Grell et al.,* 2005) have been developed to estimate and investigate the environmental load of air pollutants. These models include embedded (1-dimensional) dry deposition modules (sub-models) that apply different approaches of parameterization schemes to calculate deposition of given trace gases or aerosols. The deposition models could be classified based on complexity of model in describing vegetation (one-, two-, or multi-layered) and in the description and parameterization of exchange/deposition processes between the atmosphere and the surface (K-theory, higher order closure, non-local closure). Deposition modules of CTMs are generally based on K-theory.

The choice is usually a compromise between application dependent requirements and data availability. The lack of measurements over different land use categories limits the validity of these modules (*Tuovinen*, 2009).

The deposition velocity (v_d) which is commonly used to model or estimate deposition rate is defined as

$$v_d = -\frac{F}{c - c_0},$$ (1)

where F is the atmosphere-surface flux of the given gas, and c and c_0 are the concentration, of the given gas at a specified reference height and at the surface, respectively (*Chamberlain,* 1967). Most of the global models available in the literature estimate ozone deposition using the resistance analogy (*Sitch et al.,* 2007), and calculate the stomatal resistance using multiplicative algorithms as a function of meteorological parameters (*Jarvis,* 1976), or use physiological schemes, which link stomatal resistance to photosynthesis, like the so-called BWB-algorithm (Ball-Woodrow-Berry) (*Ball et al.,* 1987). There are few studies aiming to compare ozone deposition modules based on different approaches (*Meyers* and *Baldocchi,* 1988; *Zhang et al.,* 2002), some studies compare different algorithms to estimate stomatal resistance (*Büker et al.,* 2007; *Misson et al.,* 2004; *Niyogi et al.,* 1998; *Uddling et al.,* 2005; *Van Wijk et al.,* 2000). In this study, three dry deposition models, all routinely applied in regional CTMs and characterized by different deposition schemes are evaluated. The investigated

one-dimensional dry deposition models are described in detail in *Zhang et al.* (2003) (the ZHANG model), in *Stern* (2009), and in *Schaap et al.* (2008) (the Deposition of Acidifying Compounds (DEPAC) model). For the evaluation of model results, measured ozone flux data were used for different time scales over the vegetation period. Since these ozone deposition models are widely used for estimation of ozone deposition over large areas, e.g., *Vautard et al.* (2007), it is important to investigate model applicability over different land use categories (LUCs). We choose a land use category (LUC), namely evergreen needleleaf forest, for which none of the investigated models were calibrated. The performance of the ZHANG model has been evaluated for certain land use types (deciduous-forest, mixed-forest, grassland, and vineyard) with correlation (R^2) 0.14–0.51 in summertime using 1–3-month-long datasets (*Zhang et al.,* 2002). They showed that the model overestimated measurements in general, but in the case of mixed forest they found a slight underestimation in the early morning hours. *Büker et al.* (2007) found a correlation (R^2) of 0.3 and overestimation for birch and an R^2 of 0.67 and underestimation for beech again, indicating the site specific behavior of models. The evaluation of the DEPAC model was carried out for sulfur-dioxide over deciduous-forest, coniferous-forest, grassland, and heathland categories with $R^2 = 0.01$–0.69 for wet and dry conditions using 1–10 months long datasets (*Erisman et al.,* 1994). DEPAC-Wesely model have been widely tested over e.g., grassland and temperate deciduous forest (*Pio et al.,* 2000; *Wu et al.,* 2011).

In order to explore discrepancies in results caused purely by the different deposition schemes, other basic parts of the models (not related to the deposition module, e.g., parameterization of meteorological variables) were standardized. The main questions addressed by this work are: (i) What environmental factors have impact on measured ozone deposition at the study site? (ii) What are the weaknesses of the investigated modules and how could they be improved?

The detailed in-depth evaluation of the discrepancies and their causes give an objective evaluation of deposition schemes performances, and designate the direction of further improvements of the ozone deposition models.

2. Material and methods

2.1. Site description

For this study, a six month dataset for the Niwot Ridge AmeriFlux site (Colorado, US) in the Roosevelt National Forest in the Rocky Mountains (40°1'58.4" N, 105°32'47.0" W, 3050 m a.s.l.) was used. Since the site lies on the hillside, the mountain-valley wind can effect meteorological parameters significantly. The soil in the Niwot Ridge area can be characterized by 32.3–63.4% sand and 27.7–50.4% silt content in the upper 12 cm layer (*Schütz,*

2005). The soils at the forested subalpine zone of the Front Range are typically cryalfs or cryolls depending on slope orientation (*Birkeland et al.*, 2003), developed on glacial till, extremely gravelly (granite debris). During May (spring), when the annual snowmelt occurs, the soils are fairly saturated with melt water. The mountain-valley winds predominate at this site (*Fig. 1*), upslope flows from the east occur on many summer afternoons bringing high concentrations of anthropogenic pollutants, including ozone, from the Denver/Boulder Metropolitan area and have a profound effect on atmospheric ozone dynamics (*Turnipseed et al.,* 2009). *Table 1* contains the descriptive parameters of this site.
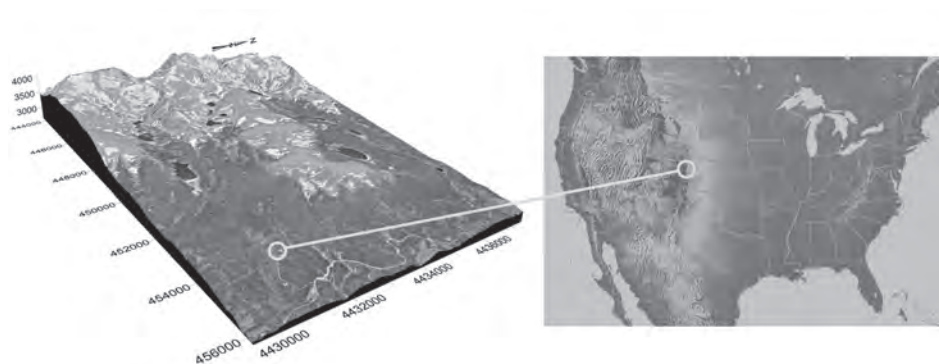
Fig. 1. Relief and location of the Niwot Ridge Ameriflux site.

Table 1. Descriptive characteristics of the study site, and site specific model input data used in the calculations

Site characteristics	Value	Reference
Average annual mean temperature	0.13 °C	1961–1990 mean, CRU CL 2.0 dataset (*New et al.,* 2002)
Annual total precipitation	482 mm	
Mean (minimum, maximum) temperature (T)	9.41 °C (−14.17 °C, 23.63 °C)	May-October 2003, measured dataset
Total precipitation (P)	232 mm	
Mean (minimum, maximum) soil water content (SWC, θ)	0.152 m^3 m^{-3} (0.076 m^{3}m^{-3}, 0.389 m^3 m^{-3})	
Site specific data used in model		
Average height of canopy (h)	11.4 m	
Leaf area index (*LAI*)	4.2 m^2 m^{-2}	(*Turnipseed et al.,* 2009)
Displacement height (d)	7.8 m	
Aerodynamic roughness (z_0)	1.6 m	

2.2. Measurements

2.2.1. Data used in the study

Continuous ozone flux and meteorological measurements above a subalpine forest canopy (*Pinus contorta, Picea engelmannii, Abies lasiocarpa*) were carried out during the growing season (May-October) of 2003 at 21.5 m height. Effect of short term variations in meteorological parameters has already been discussed in a previous publication (*Turnipseed et al.,* 2009). The ozone flux was measured using the eddy-covariance (EC) technique above the canopy, detailed description of the experiment can be found in *Monson et al.* (2002) and *Turnipseed et al.,* (2002, 2003, 2009). The meteorological data (air temperature (*T*), vapor pressure deficit (*VPD*), soil water content (*SWC*), photosynthetically active radiation (*PAR*), and solar radiation (*SR*) measurements), carbon-dioxide (CO_2) flux, and additional information were obtained from the Ameriflux network (cdiac.ornl.gov/ftp/ameriflux/data/). Due to the lack of in-situ measurements of soil water retention, the value of wilting point ($0.169 \, m^3 \, m^{-3}$) and field capacity soil moisture ($0.396 \, m^3 \, m^{-3}$) were taken from the IGBP-DIS (5×5 arc-minutes) resolution database (Global Gridded Surfaces of Selected Soil Characteristics (International Geosphere-Biosphere Programme – Data and Information System)) (*Global Soil Data Task Group*).

2.2.2. Data processing and quality assurance

Quality assurance of measured ozone flux data were carried out. Positive fluxes were not taken into account (ozone flux toward the ecosystem is negative by definition). After filtering the ozone flux data, the dataset contains 4013 records of the initially available 5243 half-hourly values (23% of the data were omitted) and 24% of carbon-dioxide fluxes were excluded (initially 7142 data, after filtering 5395). Flux data were omitted during periods of precipitation and very low turbulence intensity, where friction velocity (u^*) is less than $0.2 \, ms^{-1}$ after *Turnipseed et al.* (2009).

In the case where measured data were available for more than 70% of the day (assumed as a representative day), gap filling of measured ozone flux was performed to fill the missing half-hourly values using monthly mean diurnal variations technique (*Falge et al.,* 2001). Using the same technique, daily accumulated ozone fluxes and daily averages of environmental parameters were calculated to eliminate the effect of diurnal variations of wind direction due to the mountain-valley wind system on the days when measured data were available for more than 70% of the day.

2.3. Modeling

The dry deposition models evaluated here are all routinely applied in studies using regional CTMs that are described in the literature and applied over large spatial extents (*Stern et al.,* 2008; *Cho et al.,* 2009), therefore, it is important to examine the accuracy of their estimations. The ZHANG model is the deposition submodel of AURAMS CTM (*Smyth et al.,* 2009), and DEPAC is applied in RCG (*Stern,* 2009) and in LOTOS-EUROS (*Schaap et al.,* 2008) CTMs. Models were tested in site-specific mode, which employs local vegetation parameters (*Table 1*) and in situ meteorological observations as input data. Alternatively, the investigated models can be run in regional mode, using the default vegetation parameters, even though these deposition models are not validated for all types of LUCs described by the simulations.

The dry deposition models are vertical (1-dimensional), one-layered models based on the so-called big-leaf concept, as the canopy is treated as one big leaf surface (*Fig. 2*), and the deposition velocity is calculated using the resistance analogy:

$$v_d = \frac{1}{R_a + R_b + R_c}.$$ (2)

Deposition velocity can be calculated as the reciprocal value of the residual of the resistances (analogous to Ohm's low for electricity) via parameterization of the aerodynamic (R_a) and quasi-laminar boundary layers (R_b) and canopy resistance (R_c), where this latter term includes stomatal (R_{st}), mesophyll (R_{mes}), in-canopy (R_{inc}), cuticular (R_{cut}), and soil (R_{soil}) resistances. Resistance schemes are described later in Section 2.3. The differences in the schemes occur in parameterization of these resistances (*Table 2*). Calculation of R_a is very similar in both models, the ZHANG model uses the formula presented in *Padro et al.* (1991) and the DEPAC model uses the parameterization of *Wesely* and *Hicks* (1977). R_b is parameterized using the same formula (*Hicks,* 1982) in both models. To estimate R_c, the following equations were used in the ZHANG model (Eq.(3), *Zhang et al.,* 2003) and in the DEPAC model (Eq.(4), *Erisman et al.,* 1994):

$$\frac{1}{R_c} = \frac{1 - W_{st}}{R_{st} + R_{mes}} + \frac{1}{R_{cut}} + \frac{1}{R_{inc} + R_{soil}},$$ (3)

$$\frac{1}{R_c} = \frac{1}{R_{st} + R_{mes}} + \frac{1}{R_{cut}} + \frac{1}{R_{inc} + R_{soil}},$$ (4)

where W_{st} is the fraction of stomatal blocking under wet conditions, and is calculated as:

$$W_{st} = \begin{cases} 0, & SR \leq 200\,\mathrm{Wm}^{-2} \\ \dfrac{(SR-200)}{800}, & 200 < SR \leq 600\,\mathrm{Wm}^{-2} \\ 0.5, & SR > 600\,\mathrm{Wm}^{-2} \end{cases} \tag{5}$$

Zhang et al. (2003) stated that in the case of morning dew and sunshine immediately after rain, solar radiation could be strong and R_{st} is small, however, stomata can be partially blocked by water films and the W_{st} term will then increase the stomatal resistance.
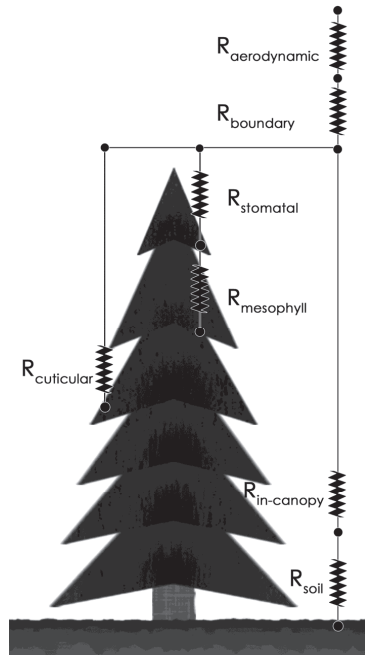
Fig. 2. Resistance network used in the models.

One of the main differences between the models is the parameterization of stress functions of R_{st} (*Table 2*). The ZHANG model calculates R_{st} as described in *Zhang et al.* (2002, 2003), meanwhile DEPAC model has two different parameterizations for the stomatal resistance based on *Baldocchi et al.* (1987) (referred to here as the DEPAC-Baldocchi model) and *Wesely* (1989) (referred to here as the DEPAC-Wesely model), therefore, three different modules are

used in this study. Both the ZHANG model and the DEPAC-Baldocchi model calculate R_{st} using functions of air temperature ($f(T)$) and vapor pressure deficit ($f(VPD)$), but water stress is described in different ways (for detailed description of model equations see *Appendix 1*). In the case of optimum environmental conditions, the canopy stress functions are equal to one, representing no stress. In the ZHANG model, water stress ($f(\psi)$) is a step function of leaf-water-potential (ψ) depending on *SR* (*Table 2*), meanwhile in the DEPAC-Baldocchi model there is no soil water stress, $f(\theta)$ equals to 1.

Table 2. Description of main resistances and their parameterization in the model versions used in the study. Independent variables determining their values in the different parameterizations of the models are shown

Resistance	ZHANG	DEPAC-Baldocchi	DEPAC-Wesely
R_{st}	f(T, vpd, ψ)	f(T, vpd, θ)	f(T, SR)
R_{mes}	constant	constant	constant
R_{cut}	f(LAI, u^*)	constant	constant
R_{inc}	f(LAI, u^*)	f(h, LAI, u^*)	f(h, LAI, u^*)
R_{soil}	f(T)	constant	constant

Finally, model parameterization improvements were carried out. Many studies have shown that soil moisture is an important factor for controlling stomatal activity (*Bates* and *Hall,* 1981; *Gollan et al.,* 1986). It has been shown previously and also acknowledged in the literature that resistance based models are sensitive to moisture stress parameterization (*Büker et al.,* 2012; *Van Wijk et al.,* 2000). Soil moisture content data is easy to obtain compared to the leaf-water-potential used in some modeling approaches. Since none of the investigated models use soil moisture in the parameterization of stomatal resistance, model improvements were carried out (the ZHANG modified model and the DEPAC-Baldocchi modified model later on) with the introduction of a soil moisture ($f(\theta)$ in Eq.(6)) stress function based on the work of, e.g., *Mészáros et al.* (2009) and *Grünhage* and *Haenel* (2008). In the case of ZHANG model, the leaf-water-potential function was replaced by a function of soil moisture. In the case of DEPAC-Baldocchi model, instead of constant value (no soil moisture stress), the soil moisture stress function was implemented. The stress function introduced in the models for *SWC* is as follows:

$$f(\theta) = \begin{cases} 1 & \text{if } \theta > \theta_f \\ \max\left\{\dfrac{\theta - \theta_w}{\theta_f - \theta_w}, 0.05\right\} & \text{if } \theta_w < \theta \leq \theta_f \\ 0.05 & \text{if } \theta \leq \theta_w \end{cases}, \tag{6}$$

where θ_w and θ_f denote soil moisture content corresponding to the wilting point and the field capacity, respectively.

To explore the performance of the different resistance schemes of the investigated models without influence of parameterization of environmental parameters, measured meteorological variables were used when it was possible, and meteorological and astronomical parameterizations (e.g., characteristics of moist air and solar radiation) were synchronized using one common scheme in all other cases. Vapor pressure deficit was calculated using the approach of the World Meteorological Organization (2008), density of moist air, specific heat of moist air was estimated after *Grünhage* and *Haenel* (2008). Solar zenith angle was calculated using the parameterization scheme provided by NASA (*Landsman*, 1993).

2.4. Evaluation methodology

2.4.1. Measurement evaluation

In the first part of this work, analyses of in situ observations were carried out to explore the effect of environmental factors on ozone deposition. Climate impact studies and ecosystem studies are mainly focused on the accumulated pollutant load the ecosystem receives, i.e., the ozone uptake, to be able to qualitatively evaluate/predict its effect on photosynthetic activity (*Harmens* and *Mills,* 2012; *Lombardozzi et al.,* 2012; *Tang et al.,* 2014).

We examined soil moisture, global radiation, photosynthetically active radiation, vapor pressure deficit, and temperature as abiotic controlling factors of ozone flux. Half-hourly measurements were quality checked and analyzed for the whole six-month-long period for changes in relationships between ozone fluxes and ozone deposition drivers throughout the growing season (May-October).

2.4.2. Model evaluation

In the second part of our study, outputs of three deposition models were compared to measured ozone fluxes. Different model quality indicators were calculated to evaluate model performance using half-hourly data on monthly and six-month-long time scales. The statistical metrics used in this study (Pearson linear correlation coefficient (R), mean bias (MB), mean absolute error (MAE),

root mean square error (*RMSE*), normalized mean square error (*NMSE*), index of agreement (*IA*), and modeling efficiency (*ME*) indicators) were calculated for the whole period both for daytime (when the solar zenith angle is greater than zero) and nighttime (when the solar zenith angle is less than or equal to zero). The equations of these metrics are given below (*Neter et al.,* 1988; *Chang* and *Hanna,* 2004; *Pereira,* 2004; *Falge et al.,* 2005). *R* is the linear correlation between the observations and model results, values can vary between −1 and 1 (perfect correlation), 0 means the datasets are independent. *MB* is a measure of overall bias for variables, in case of perfect estimation it is 0. *MAE* is overall absolute bias of observed and modeled data. *RMSE* is the square root of the average squared bias of the modeled data, it is sensitive for extreme errors. *NMSE* emphasizes the scatter in the entire data set. Smaller values of *NMSE* denote better model performance. *IA* can vary between 0 and 1, and it is a metric of mean square error, in case of perfect agreement it is equal to 1. *ME* has a range from 1 to −∞, and it is a measure of the accuracy of model estimations to the mean of observations, any positive value means that estimation is better than means of measurements, in case of perfect agreement it is equal to 1.

3. Results and discussion

3.1. Controlling factors of ozone fluxes

In order to explore the effect of environmental factors on ozone deposition, relationships between environmental variables and energy fluxes were examined on a daily basis and on the original half-hourly resolution using eddy covariance (EC) data.

Half-hourly measured meteorological data were compared (*T*, *SWC*, *VPD*, *SR*, *PAR*) with half-hourly measured ozone fluxes. *Fig. 3* shows time series plots for these variables. The soil at the site was more or less saturated with water during May, therefore, soil moisture is probably not a limiting factor during that period. *Turnipseed et al.* (2009) found that after photosynthetic photon flux density (*PPFD*), *VPD* was the most dominant environmental driver controlling the daytime deposition of O_3 at this site through its influence over stomatal conductance.
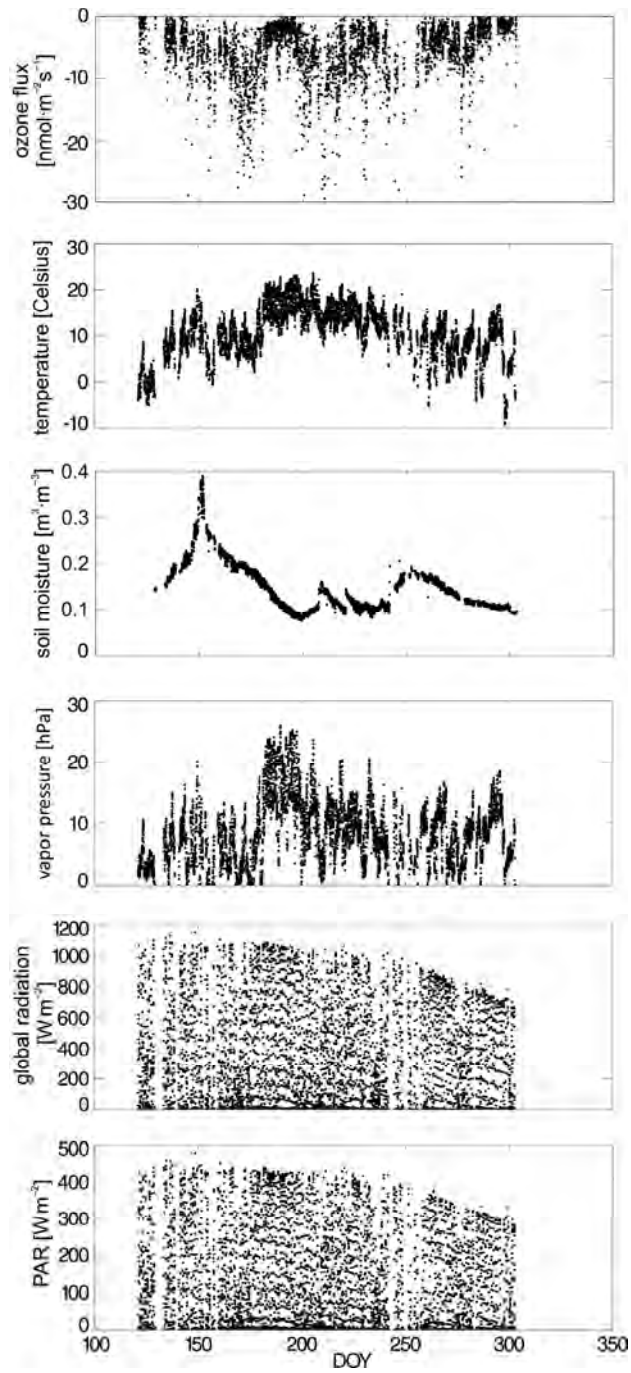
Fig. 3. Time series of controlling factors and ozone flux (May-October, 2003).

3.2. Results of model evaluations

Model results were investigated on half-hourly and daily time steps, and model performance indicators were calculated based on measured and modelled ozone flux data.

The ZHANG model outperformed the other two model versions on the original half-hourly resolution, but one should be aware of the still poor correlation between measured and modeled ozone flux for the whole period (*Table 3*). In order to evaluate the average behavior of models and how their performance varies with time of the day, mean diurnal variations of measured and modeled ozone fluxes were calculated. The ZHANG model provided the best results compared to the other two models in capturing the ozone flux magnitude and dynamics as shown by mean diurnal variation (*Fig. 4A* and *C*). The ZHANG modified model in *Fig. 4A* will be addressed later in the paper.

Table 3: Model quality indicators based on half-hourly measured ozone fluxes (May-October, 2003)

Model name	Period	R^2 (p<0.001)	N	MB [nmol m^{-2} s^{-1}]	MAE [nmol m^{-2} s^{-1}]	RMSE [nmol m^{-2} s^{-1}]	NMSE [nmol m^{-2} s^{-1}]	IA	ME
ZHANG model	All data	**0.26**	3877	1.39	3.21	**4.45**	**0.52**	**0.68**	**0.08**
	Daytime	**0.17**	2796	1.83	3.77	**4.91**	**0.44**	**0.59**	−0.03
	Nighttime	**0.07**	1081	**0.25**	**1.76**	2.91	0.93	**0.47**	−0.15
DEPAC-Baldocchi model	All data	0.15	3877	7.30	8.09	10.07	1.44	0.46	−3.71
	Daytime	0.05	2796	9.84	10.47	11.72	1.29	0.37	−4.88
	Nighttime	0.02	1081	0.74	1.93	**2.90**	**0.80**	0.31	−0.15
DEPAC-Wesely model	All data	0.07	3877	**−0.50**	**3.03**	4.55	0.75	0.42	0.04
	Daytime	0.01	2796	**−0.98**	**3.46**	5.04	0.70	0.34	−0.09
	Nighttime	0.02	1081	0.74	1.93	**2.90**	**0.80**	0.31	−0.15

Mean measured ozone flux [nmol m^{-2} s^{-1}] for all data: −5.50, daytime: −6.51, nighttime: −2.90
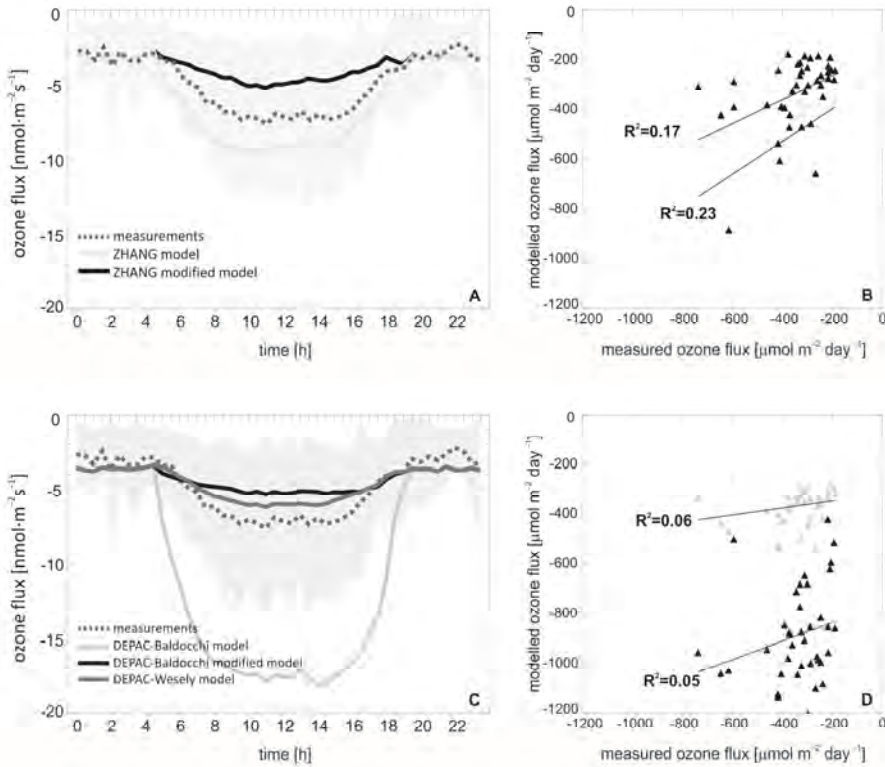
Fig. 4. Performance of the ZHANG model and the ZHANG modified model (May-October, 2003): (A) mean diurnal variation of half-hourly measured and modeled ozone flux, (B) daily accumulated measured and modeled ozone flux. Performance of the DEPAC-Baldocchi model, the DEPAC-Wesely model, and the DEPAC-Baldocchi modified model (May-October, 2003): (C) mean diurnal variation of half-hourly measured and modeled ozone flux, (D) daily accumulated measured and modeled ozone flux.

The performances of the two versions of the DEPAC model stay below that of the ZHANG model as it is reflected by most model quality indicators listed in *Table 3*. Correlation is lower, the DEPAC-Baldocchi and the DEPAC-Wesely parameterization can only explain 15% and 7% of the observed variance. Model errors are significantly higher in the case of the DEPAC-Baldocchi parameterization. It should be noted that although DEPAC-Wesely can explain even less of the observed variance of half-hourly ozone deposition, its performance is comparable to that of the ZHANG model based on some other statistical measures (*IA*, *ME*, *NMSE*, *RMSE*).

Mean diurnal variation of ozone deposition modeled by different parameterizations of the DEPAC model are shown in *Fig. 4C* together with measured ozone deposition. The DEPAC-Baldocchi model overestimates the measured fluxes (as it is also indicated by statistics based on the full half-hourly dataset, shown in *Table 3*). The most important difference between the ZHANG and DEPAC models lies in the parameterization of R_{st}. It has been reported by *Mészáros et al.* (2009) that deposition models are sensitive to soil moisture content input. The soil moisture stress is not parameterized in the DEPAC-Baldocchi model, $f(\theta)$ has a fixed value of one, which assumes that there is no water stress for the canopy. So, these results show that it is essential to include the soil moisture in the dry deposition models, consequently, the ZHANG model is to be preferred above the DEPAC models.

As it is presented in *Fig. 4C,* the DEPAC-Wesely model underestimates the measured fluxes, although model error is lower than in the case of the DEPAC-Baldocchi parameterization (*Table 3*). The DEPAC-Baldocchi modified model in *Fig. 4C* will be discussed later in the paper.

To explore if models capture long-term variabilities, monthly means of ozone fluxes were calculated (*Fig. 5*). We separated data to daytime (when solar elevation angle is greater than 0, *Fig. 5A*) and nighttime (when solar elevation angle is less than 0, *Fig. 5B*) parts, since the modeling approach is different for nighttime conditions (see *Appendix 1*). The calculated nighttime ozone deposition data reveal a very good agreement with measured flux (*Fig. 5B*). Considering that nighttime ozone fluxes are dominated by cuticular or soil pathways, this good performance compared to the daytime performance of the models suggests that mostly the description of stomatal uptake is responsible for model errors. For observed ozone flux during nighttime, the DEPAC-Baldocchi and the DEPAC-Wesely models result in the same values, since the parameterizations are the same for nighttime conditions. For daytime data where stomatal resistance is calculated using the more sophisticated approach described in *Appendix 1*, model performances diverge more. The relatively simple parameterization of the DEPAC-Wesely model simulated monthly average ozone deposition with the smallest bias in each month except June. It should be kept in mind, however, that only measured ozone flux data is considered here, i.e., this is not real average ozone deposition but the monthly average of available measured data.

When models are applied in climate change impact studies over large spatial and temporal extents, data are often not used in their original temporal resolution (see, e.g., *Sitch et al.,* 2007). Model results were examined on a daily time step using accumulated ozone fluxes to simulate ozone load (*Fig. 4B, Fig. 4D*). This approach is used in most large scale climate impact studies. Results of the ZHANG model have the best correlation with the measured accumulated ozone fluxes ($R^2 = 0.23$, $p < 0.05$, *Table* 4), but in case of DEPAC-Baldocchi, the model correlation cannot be detected ($R^2 = 0.05$, $p = 0.144$, *Table* 4).
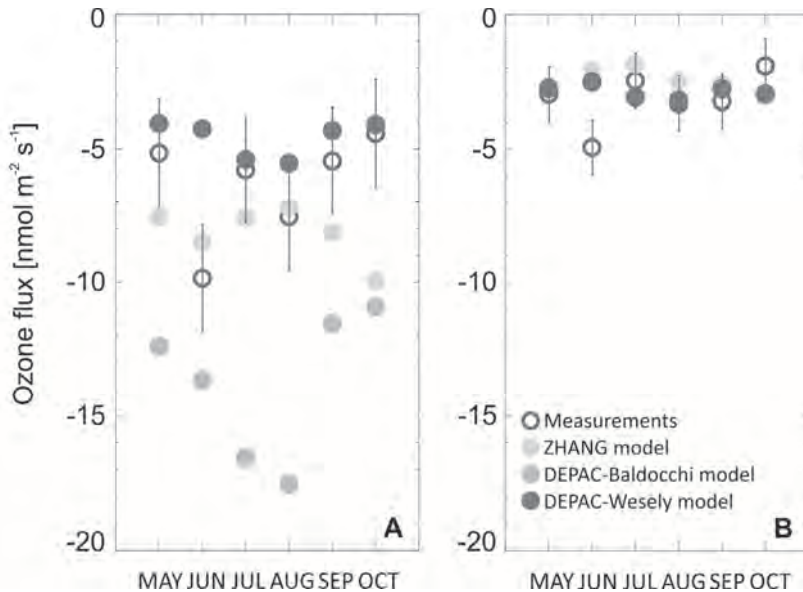
Fig. 5. Monthly means of half-hourly modeled and measured ozone fluxes (May-October, 2003): (A) daytime, when solar elevation greater than 0, (B) nighttime, when solar elevation is less than zero. Standard deviation of measured data is also shown as error bars.

Table 4. Model quality indicators based on daily measured accumulated ozone fluxes (May-October, 2003)

Model name	R^2	p	N	MB [μmol m^{-2} day^{-1}]	MAE [μmol m^{-2} day^{-1}]	RMSE [μmol m^{-2} day^{-1}]	NMSE [nmol m^{-2} day^{-1}]	IA	ME
ZHANG model	**0.22**	0.002	39	148.92	171.07	218.66	0.28	0.99	0.96
DEPAC-Baldocchi model	0.06	0.144	39	548.17	552.93	585.12	1.13	0.98	0.51
DEPAC-Wesely model	0.02	0.358	39	**61.14**	**119.43**	**151.74**	**0.17**	**1.00**	**0.99**

Mean measured ozone flux [μmol m^{-2} day^{-1}]: –340.94

This contradicting behavior of the three structurally identical models demonstrates the need for a careful interpretation of resistance based model results for sites where no previous results are reported in the literature regarding correlation and systematic model errors. Results of the ZHANG modified model (*Fig. 4A*) has a lower correlation ($R^2 = 0.09$, $p < 0.001$ instead of 0.25 in *Table 3*) with measurements using the full half-hourly dataset, and RMSE value did not change (4.69 nmol m^{-2} s^{-1}). In case of the DEPAC-Baldocchi modified model (*Fig. 4C*), R^2 decreased (0.05, $p < 0.001$ instead of 0.15 in *Table 3*), parallel *RMSE* decreased almost by half compared to the original parameterization (4.66 nmol m^{-2} s^{-1} versus 10.07 nmol m^{-2} s^{-1}). On a daily time step, the DEPAC-Baldocchi modified model results showed better correlation with measured accumulated ozone fluxes than the original model ($R^2 = 0.06$, $p = 0.140$; *Fig. 4D*). Comparing *Fig. 4B* and *Fig. 4D* we can conclude that the modified models resulted in similar values, at least compared to the differences observed when comparing the original model versions. This can be explained by non-stomatal resistance (R_{cut}, R_{inc}, and R_{soil}), since with implementation of $f(\theta)$, R_{st} has the same value in both modified models.

Mészáros et al. (2009) carried out a sensitivity analysis of a multiplicative dry deposition model and found that soil moisture content is one of the most influential parameters in the model. This explains why the introduction of soil moisture stress parameterization in the DEPAC-Baldocchi model had such a dramatic effect on model results. However, as indicated by measurements, soil moisture was not a driving factor for ozone deposition at this site in the measurement period. This suggests that model constraints do not reflect real environmental circumstances, i.e., model results agree with measured ozone fluxes, but the model fails to explain short-term variability of ozone deposition, which led to a decrease in correlation between half-hourly measured and modeled ozone fluxes. The use of soil moisture content data representative for the whole root zone when available should improve model results.

4. Conclusion

In this study, ecosystem-atmosphere ozone fluxes are simulated using three widely used deposition models. Our model validation results showed worse model performance during daytime when stomatal activity is higher, which suggests that modeling problems are especially related to the stomatal pathway ozone deposition. It was also shown that the ZHANG model is to be preferred under most circumstances, as it provided the best model-measurement agreement among the used models in hourly and daily time steps. Nevertheless, the most accurate long-term (monthly average) results were provided by the DEPAC-Wesely model. The inclusion of soil moisture stress in two models improved model accuracy, but the correlation remained low, suggesting that

there are other errors in the description of factors and their interactions regulating ozone deposition in the models.

In spite of their wide acceptance (*Brook et al.,* 1999; *Flemming* and *Stern,* 2007), the multiplicative models used in this study have not been calibrated for some important land cover types, e.g., none of the above models have been calibrated for evergreen forests. In studies where these models are applied on large spatial scales, continents, and countries (*Manders et al.,* 2012; *van Loon et al.,* 2007; *Smyth et al.,* 2009), this can bias the results over these land uses, leading to spatially varying uncertainty in the estimations, which should be considered when interpreting results from chemical transport models. According to our results, even if we minimize input data errors using measured driving data when available, model results diverge when validated for a randomly selected geographical location and land use type. This suggests, that the lack of calibration inhibits the reliable use of these models in case of ecosystem types other than they have been calibrated for, and hence, their practicality in large scale studies, where models are used over several ecosystems, might be questionable and their results should be interpreted carefully.

Appendix

Appendix **1:** Formulas used in the model to describe the resistance network.

Zhang model	DEPAC model
$Ra = \dfrac{1}{\kappa \cdot u^*}\left[0.74 \cdot \ln\left(\dfrac{z_r}{z_0}\right) - \psi_h\right]$	$Ra = \dfrac{1}{\kappa \cdot u^*}\left[\ln\left(\dfrac{z_r}{z_0}\right) - \psi_h\right]$
$R_b = 1.31 \cdot \dfrac{5}{u^*}$	
$R_{st} = \dfrac{1}{G_{st}(PAR) \cdot f(T) \cdot f(vpd) \cdot f(\psi) \cdot 0.637}$	**Baldocchi** $R_{st} = \dfrac{1}{G_{st}(PAR) \cdot f(T) \cdot f(vpd) \cdot f(\theta) \cdot 0.637}$ **Wesely** $R_{st} = 1{,}571 \cdot R_i \cdot \dfrac{400}{T \cdot (40-T)} \cdot \left(1 + \left(\dfrac{200}{SR + 0.1}\right)^2\right)$
if solar elevation < 0: $R_{st} = 12500$ $\left[sm^{-1}\right]$	
$R_{mes} = 0$ $\left[sm^{-1}\right]$	
$R_{cut} = \dfrac{4000}{u^* \cdot LAI^{0.25} \cdot e^{0.03RH}}$ if $T < -1°C$: $R_{cut} = R_{cut} \cdot e^{0.2(-1-T)}$	$R_{cut} = 1000$ $\left[sm^{-1}\right]$
$R_{inc} = \dfrac{100 \cdot LAI^{0.25}}{(u^*)^2}$	$R_{inc} = 8 \cdot h \cdot \dfrac{LAI}{u^*}$
$R_{soil} = 200$ $\left[sm^{-1}\right]$ if $T < -1°C$: $R_{soil} = R_{soil} \cdot e^{0.2(-1-T)}$	$R_{soil} = 100$ $\left[sm^{-1}\right]$ if $T < 0°C$: $R_{soil} = 2000$ $\left[sm^{-1}\right]$
$G_{st}(PAR) = \dfrac{LAI_s}{r_{st}(PAR_s)} + \dfrac{LAI_{sh}}{r_{st}(PAR_{sh})}$	$G_{st}(PAR) = \dfrac{LAI}{250 \cdot (1 + 25/PAR_{measured})}$
$r_{st}(PAR_x) = 250 \cdot (1 + 25/PAR_x)$	$R_i = \begin{cases} 130 \left[sm^{-1}\right] & summer \\ 250 \left[sm^{-1}\right] & autumn \\ 400 \left[sm^{-1}\right] & winter \\ 250 \left[sm^{-1}\right] & spring \end{cases}$
$f(VPD) = 1 - b_{VPD} \cdot (e_s - e)$	

$f(T) = \dfrac{T - T_{\min}}{T_{opt} - T_{\min}} \cdot \left(\dfrac{T_{\max} - T}{T_{\max} - T_{opt}} \right)^{b_T}$, *Baldocchi et al.*, 1987	
$b_T = \dfrac{T_{\max} - T_{opt}}{T_{\max} - T_{\min}}$, *Baldocchi et al.*, 1987	
$f(\psi) = \begin{cases} 1 & \text{if } \psi > \psi_{c1} \\ \max\left(\dfrac{\psi - \psi_{c2}}{\psi_{c1} - \psi_{c2}}, 0.05 \right) & \text{if } \psi_{c2} < \psi \leq \psi_{c1} \\ 0.05 & \text{if } \psi \leq \psi_{c2} \end{cases}$ $\psi = -0.72 - 0.0013 SR$	$f(\theta) = 1$
unstable $\Phi_h = 0.74 \cdot \ln\left(\dfrac{1 + \left(1 - \left(9 \cdot \dfrac{z_r}{L} \right) \right)^{0.25}}{2} \right)$	unstable $\Phi_h = \exp\left[0.598 + 0.39 \cdot \ln\left(-\dfrac{z_r}{L} \right) - 0.09 \cdot \left(\ln\left(-\dfrac{z_r}{L} \right) \right)^2 \right]$
stable $\Phi_h = -4.7 \dfrac{z_r}{L}$	stable $\Phi_h = -5 \dfrac{z_r}{L}$
neutral $\Phi_h = 0$	

***Appendix* 2**: Nomenclature for Appendix 1.

ψ_{c1}, ψ_{c2}	specify leaf-water-potential dependency parameters [MPa]
Φh	dimensionless stability function
b_{VPD}	*vpd* constant [kPa^{-1}],
e, e_s	ambient and saturation water vapor pressure [kPa], respectively
G_{st}	unstressed stomatal conductance [m s^{-1}]
κ	Karman constant (0.41)
L	Monin-Obukhov length (calculation method is not detailed here) [m]
PAR_s/PAR_{sh}	*PAR* received by sunlit and shaded leaves, respectively [W m^{-2}]
R_i	minimum bulk canopy stomatal resistances for water vapor [s m^{-1}]
r_{st}	unstressed leaf stomatal resistance [s m^{-1}]
T_{min}, T_{max}, T_{opt}	minimum, maximum and optimum T for stomatal opening, respectively (–5 °C, 40 °C and 15 °C)
z_r	reference height [m]

References

Anav, A., Menut, L., Khvorostyanov, D., and *Viovy, N.*, 2011: Impact of tropospheric ozone on the Euro-Mediterranean vegetation. *Glob. Change Biol. 17,* 2342–2359. https://doi.org/10.1111/j.1365-2486.2010.02387.x

Ashmore, M.R., 2005: Assessing the future global impacts of ozone on vegetation. *Plant Cell Environ. 28,* 949–964. https://doi.org/10.1111/j.1365-3040.2005.01341.x

Baldocchi, D.D., Hicks, B.B., and *Camara, P.,* 1987: A canopy stomatal resistance model for gaseous deposition to vegetated surfaces. *Atmos. Environ. 21,* 91–101. https://doi.org/10.1016/0004-6981(87)90274-5

Ball, J.T., Woodrow, I.E., and *Berry, J.A.,* 1987: A model predicting stomatal conductance and its contribution to the control of photosynthesis under different environmental conditions, In (ed.: *J. Biggens*) Progress in Photosynthesis Research, IV. Martinus Nijhoff, Dordrecht, 221–224. https://doi.org/10.1007/978-94-017-0519-6_48

Bates, L.M. and *Hall, A.E.,* 1981: Stomatal Closure with Soil-Water Depletion No Associated with Changes in Bulk Leaf Water Status. *Oecologia 50,* 62–65. https://doi.org/10.1007/BF00378794

Bey, I., Jacob, D.J., Yantosca, R.M., Logan, J.A., Field, B., Fiore, A.M., Li, Q., Liu, H., Mickley, L.J., and *Schultz, M.,* 2001: Global modeling of tropospheric chemistry with assimilated meteorology: Model description and evaluation. *J. Geophys. Res, 106,* 23073–23095. https://doi.org/10.1029/2001JD000807

Birkeland, P.W., Shroba, R.R., Burns, S.F., Price, A.B., and *Tonkin, P.J.,* 2003: Integrating soils and geomorphology in mountains–an example from Front Range Colorado. *Geomorphology 55*, 329–344 https://doi.org/10.1016/S0169-555X(03)00148-X

Brook, J.R., Zhang, L., Li, Y., and *Johnson, D.,* 1999: Description and evaluation of a model of deposition velocities for routine estimates of dry deposition over North America. Part II: review of past measurements and model results. *Atmos. Environ. 33,* 5053–5070. https://doi.org/10.1016/S1352-2310(99)00251-4

Büker, P., Emberson, L.D., Ashmore, M.R., Cambridge, H.M., Jacobs, C.M.J., Massman, W.J., Müller, J., Nikolov, N., Novak, K., Oksanen, E., Schaub, M., and de la Torre, D., 2007: Comparison of different stomatal conductance algorithms for ozone flux modelling. *Environ. Pollut. 146,* 726–735. https://doi.org/10.1016/j.envpol.2006.04.007

Büker, P., Morrissey, T., Briolat, A., Falk, R., Simpson, D., Tuovinen, J.-P., Alonso, R., Barth, S., Baumgarten, M., Grulke, N., Karlsson, P. E., King, J., Lagergren, F., Matyssek, R., Nunn, A., Ogaya, R., Peñuelas, J., Rhea, L., Schaub, and M., Uddling, 2012: DO3SE modelling of soil moisture to determine ozone flux to forest trees. *Atmos. Chem. Phys*. *12,* 5537–5562. https://doi.org/10.5194/acp-12-5537-2012

Chamberlain, A.C., 1967: Transport of Lycopodium Spores and Other Small Particles to Rough Surfaces. Proceedings of the Royal Society of London, Series A, Mathematical and Physical Sciences 296, 45–70. https://doi.org/10.1098/rspa.1967.0005

Chang J.C. and Hanna, S.R., 2004: Air quality model performance evaluation. *Meteorol. Atmos. Phys. 87,* 167–196. https://doi.org/10.1007/s00703-003-0070-7

Cho, S., Makar, P. A., Lee, W. S., Herage, T., Liggio, J., Li, S. M., Wiens, B., and Graham, L., 2009: Evaluation of a unified regional air-quality modeling system (AURAMS) using PrAIRie2005 field study data: The effects of emissions data accuracy on particle sulphate predictions. *Atmos. Environ. 43,* 1864–1877. https://doi.org/10.1016/j.atmosenv.2008.12.048

Emery, C., Jung, J., Downey, N., Johnson, J., Jimenez, M., Yarwood, G., and Morris, R., 2012: Regional and global modeling estimates of policy relevant background ozone over the United States. *Atmos. Environ. 47,* 206-217. https://doi.org/10.1016/j.atmosenv.2011.11.012

Erisman, J., Van Pul, A., and Wyers, P., 1994: Parameterization of surface resistance for the quantification of atmospheric deposition of acidifying pollutants and ozone. *Atmos. Environ. 28,* 2595–2607. https://doi.org/10.1016/1352-2310(94)90433-2

Falge, E., Baldocchi, D., Olson, R., Anthoni, P., Aubinet, Marc, Bernhofer, C., Burba, G., Ceulemans, R., Clement, R., Dolman, H., Granier, A., Gross, P., Grunwald, T., Hollinger, D., Jensen, No., Katul, G., Keronen, P., Kowalski, A., Lai, Ct., Law, Be., Meyers, T., Moncrieff, H., Moors, E., Munger, Jw., Pilegaard, K., Rannik, U., Rebmann, C., Suyker, A., Tenhunen, J., Tu, K., Verma, S., Vesala, T., Wilson, K., and Wofsy, S., 2001: Gap filling strategies for defensible annual sums of net ecosystem exchange. *Agr. Forest Meteorol. 107,* 43–69. https://doi.org/10.1016/S0168-1923(00)00225-2

Falge, E., Reth, S., Brüggemann, N., Butterbach-Bahl, K., Goldberg, V., Oltchev, A., Schaaf, S., Spindler, G., Stiller, B., Queck, R., Köstner, B., and Bernhofer, C., 2005: Comparison of surface energy exchange models with eddy flux data in forest and grassland ecosystems of Germany. *Ecol. Model. 188,* 174–216. https://doi.org/10.1016/j.ecolmodel.2005.01.057

Fares, S., Vargas, R., Detto, M., Goldstein, A., Karlik, J., Paoletti, E., and Vitale, M., 2013: Tropospheric ozone reduces carbon assimilation in trees: estimates from analysis of continuous flux measurements. *Glob. Change Biol. 19,* 2427–2443. https://doi.org/10.1111/gcb.12222

Flemming, J. and Stern, R., 2007: Testing model accuracy measures according to the EU directives – examples using the chemical transport model REM-CALGRID. *Atmos. Environ. 41,* 9206–9216. https://doi.org/10.1016/j.atmosenv.2007.07.050

Fowler, D., Amann, M., Anderson, R., Ashmore, M., Cox, P., Depledge, M., Derwent, D., Grennfelt, P., Hewitt, N., Hov, O., Jenkin, M., Kelly, F., Liss, P., Pilling, M., Pyle, J., Slingo, J., and Stevenson, D., 2008: Ground-level ozone in the 21st century: future trends, impacts and policy implications. Royal Society Policy Document 15/08, London: The Royal Society.

Global Soil Data Task Group. Global Gridded Surfaces of Selected Soil Characteristics (IGBP-DIS). Data set. Available on-line [http://www.daac.ornl.gov] from Oak Ridge National Laboratory Distributed Active Archive Center, Oak Ridge, Tennessee, U.S.A. https://doi.org/10.3334/ORNLDAAC/569

Gollan, T., Passioura, J.B., and Munns, R., 1986: Soil-Water Status Affects the Stomatal Conductance of Fully Turgid Wheat and Sunflower Leaves. *Aust. J. Plant Physiol. 13,* 459–464. https://doi.org/10.1071/PP9860459

Grell, G.A., Peckham, S.E., Schmitz R., S.A., McKeen, Frost, G., Skamarock, W.C., and Eder, B., 2005: Fully coupled 'online' chemistry in the WRF model. *Atmos. Environ.t 39,* 6957–6976.

Grünhage, L. and Haenel, H.-D., 2008: PLATIN PLant-ATmosphere Interaction model. *Landbauforschung 319,* 85.

Harmens, H., and Mills, G., 2012: Ozone pollution: Impacts on carbon sequestration in Europe. ICP Vegetation Programme Coordination Centre. CEH Bangor, UK, ISBN: 978-1-906698-31-7.

Hicks, B.B., 1982: In: Critical assessment document on acid deposition, Chapter VII, Dry deposition, ATDL Contribution file 81/24, Atmospheric Turbulence and Diffusion Laboratory, NOAA, Oak Ridge, Tennessee, USA.

Hurley, P., 2008: TAPM V4. Part 1: Technical Description. *CSIRO Marine Atmos. Res. Paper 25,* 59.

Jarvis, P.G. 1976: The interpretation of the variations in leaf water potential and stomatal conductance found in canopies in the field. *Philos. T. Roy. Soc. B 273,* 593–610. https://doi.org/10.1098/rstb.1976.0035

Karnosky, D.F., Pregitzer, K.S., and Zak, D.R., 2005: Scaling ozone responses of forest trees to the ecosystem level in a changing climate. *Plant Cell Environ. 28,* 965–981. https://doi.org/10.1111/j.1365-3040.2005.01362.x

Karnosky, D.F., Zak, D.R., Pregitzer, K.S., and Awmack, C.S., 2003: Tropospheric O3 moderates responses of temperate hardwood forests to elevated CO2: a synthesis of molecular to ecosystem results from the Aspen FACE project. *Funct. Ecol. 17,* 289–304. https://doi.org/10.1046/j.1365-2435.2003.00733.x

Kirtman, B., Power, S.B., JAdedoyin, .A., Boer, G.J., Bojariu, R., Camilloni, I., Doblas-Reyes, F.J., Fiore, A.M., Kimoto, M., Meehl, G.A., Prather, M. Sarr, A., Schär, C., Sutton, R., van Oldenborgh, G.J., Vecchi, G., Wang, H.J., 2013: Near-term Climate Change: Projections and Predictability. In: *Stocker, T.F., Qin, D., Plattner, G.-K., Tignor, M., Allen, S.K., Boschung, J., Nauels, A., Xia, Y., Bex, V., and Midgley, P.M. (eds.),* 2013: Climate Change 2013: The Physical Science Basis. Contribution of Working Group I to the Fifth Assessment Report of the Intergovernmental Panel on Climate Change. Cambridge University Press, Cambridge, United Kingdom and New York, NY, USA.

Klingberg, J., Engardt, M., Uddling, J., Karlsson, P., and Pleijel, H., 2011: Ozone risk for vegetation in the future climate of Europe based on stomatal ozone uptake calculations. *Tellus A 63,* 174–187. https://doi.org/10.1111/j.1600-0870.2010.00465.x

Kvalevåg, M.M. and G., Myhre, 2013: The effect of carbon-nitrogen coupling on the reduced land carbon sink caused by tropospheric ozone. *Geophys. Res. Lett. 40,* 3227–3231. https://doi.org/10.1002/grl.50572

Landsman, W.B., 1993: In Astronomical Data Analysis Software and Systems II. In (eds.: *Hanisch, R.J., Brissenden, R.J.V.,* and *Barnes, J.*), A.S.P. Conference Series, 52, 246.

Lombardozzi, D., Levis, S., Bonan, G., and Sparks, J.P., 2012: Predicting photosynthesis and transpiration responses to ozone: decoupling modelled photosynthesis and stomatal conductance. *Biogeosciences 9,* 3113–3130. https://doi.org/10.5194/bg-9-3113-2012

Loreto, F. and Fares, S., 2007: Is Ozone Flux Inside Leaves Only a Damage Indicator? Clues from Volatile Isoprenoid Studies. *Plant Physiol. 143,* 1096–1100. https://doi.org/10.1104/pp.106.091892

Manders, A., van Meijgaard, E., Mues, A., Kranenburg, R., van Ulft, L.H., and Schaap, M., 2012: The impact of differences in large-scale circulation output from climate models on the regional modeling of ozone and PM. *Atmos. Chem. Phys. 12,* 9441–9458. https://doi.org/10.5194/acp-12-9441-2012

Menut, L., Bessagnet, B., Khvorostyanov, D., Beekmann, M., Blond, N., Colette, A., Coll, I., Curci, G., Foret, G., Hodzic, A., Mailler, S., Meleux, F., Monge, J.-L., Pison, I., Siour, G., Turquety, S., Valari, M., Vautard, R., and Vivanco, M.G., 2013: CHIMERE 2013: a model for regional atmospheric composition modeling. *Geosci. Model Dev. 6,* 981–1028. https://doi.org/10.5194/gmd-6-981-2013

Mészáros, R., Szinyei, D., Vincze, C., Lagzi, I., Turányi, T., Haszpra, L., and Tomlin, A.S., 2009: Effect of the soil wetness state on the stomatal ozone fluxes over Hungary. *Int. J. Environ.Pollut. 36,* 180–194. https://doi.org/10.1504/IJEP.2009.021825

Meyers T.P. and Baldocchi, D.D., 1988: A comparison of models for deriving dry deposition fluxes of O3 and SO2 to a forest canopy. *Tellus B 40,* 270–284. https://doi.org/10.3402/tellusb.v40i4.15916

Misson, L., Panek, J.A. and *Goldstein, A.H.,* 2004: A comparison of three approaches to modeling leaf gas exchange in annually drought-stressed ponderosa pine forests. *Tree Physiol. 24,* 529–541. https://doi.org/10.1093/treephys/24.5.529

Monson, R.K., Turnipseed, A.A., Sparks, J.P., Harley, P.C., Scott-Denton, L.E., Sparks, K.L., and *Huxman, T.E.,* 2002: Carbon sequestration in a high-elevation subalpine forest. *Glob. Change Biol. 8,* 1–20. https://doi.org/10.1046/j.1365-2486.2002.00480.x

Moussiopoulos N. and *Douros, I.,* 2005: Efficient calculation of urban scale air pollutant dispersion and transformation using the OFIS model within the framework of CityDelta. *Int. J. Environ. Pollut.24,* 64–74. https://doi.org/10.1504/IJEP.2005.007385

Neter, J., Wasserman, W., and *Whitmore, G.A.,* 1988: Applied statistics. Allyn and Bacon, Inc., 3rd edition, 1006.

New, M., Lister, D., Hulme, M., and *Makin, I.,* 2002: A high-resolution data set of surface climate over global land areas. *Climate Res. 21,* 1–25. https://doi.org/10.3354/cr021001

Niyogi, D.S., Raman, S., and *Alapaty, K.,* 1998: Comparison of Four Different Stomatal Resistance Schemes Using FIFE Data. Part II: Analysis of Terrestrial Biospheric–Atmospheric Interactions. *J. Appl. Meteor. 37,* 1301–1320.
https://doi.org/10.1175/1520-0450(1998)037<1301:COFDSR>2.0.CO;2

Padro, J., den Hartog, G., and *Neumann, H.H.,* 1991: An investigation of the ADOM dry deposition module using summertime O_3 measurements above a deciduous forest. *Atmos. Environ. 25,* 1689–1704. https://doi.org/10.1016/0960-1686(91)90027-5

Pan, Y., Birdsey, R.A., Fang, J., Houghton, R., Kauppi, P.E., Kurz, W.A., Phillips, O.L., Shvidenko, A., Lewis, S.L., Canadell, J.G., Ciais, P., Jackson, R.B., Pacala, S., McGuire, A.D., Piao, S., Rautiainen, A., Sitch, S., and *Hayes, D.,* 2011: A Large and Persistent Carbon Sink in the World's Forests. *Science 333,* 6045, 988–993. https://doi.org/10.1126/science.1201609

Pereira, A.R., 2004: The Priestley–Taylor parameter and the decoupling factor for estimating reference evapotranspiration. *Agr. Forest Meteorol. 125,* 305–313.
https://doi.org/10.1016/j.agrformet.2004.04.002

Pio, C.A., Feliciano, M.S., Vermeulen, A.T., and *Sousa,* E.C., 2000: Seasonal variability of ozone dry deposition under southern European climate conditions, in Portugal. *Atmos. Environ. 34*, 195–205. https://doi.org/10.1016/S1352-2310(99)00276-9

Schaap, M., Timmermans, R.M.A., Sauter, F.J., Roemer, M., Velders, G.J.M., Boersen, G.A.C., Beck, J.P., and *Builtjes, P.J.H.,* 2008: The LOTOS–EUROS model: description, validation and latest developments. *Int. J. Environ. Pollut. 32,* 270–290. https://doi.org/10.1504/IJEP.2008.017106

Schütz, H.-U., 2005*:* Pocket gopher – Actor under the stage. Studies on Niwot Ridge, Colorado Front Range, U.S.A. In: (eds.: *Broll, G., Keplin, B.),* Mountain Ecosystems: Studies in Treeline Ecology, Springer-Verlag, Berlin Heidelberg https://doi.org/10.1007/3-540-27365-4_6

Simpson, D., Benedictow, A., and *Berge, H.,* 2012: The EMEP MSC-W chemical transport model – technical description. *Atmos. Chem. Phys. 12,* 7825–7865.
https://doi.org/10.5194/acp-12-7825-2012

Sitch, S., Cox, P.M., Collins W.J., and *Huntingford, C.,* 2007: Indirect radiative forcing of climate change through ozone effects on the land-carbon sink. *Nature 448,* 791–794.
https://doi.org/10.1038/nature06059

Smyth, S.C., Jiang, W., Roth, H., Moran, M.D., Makar, P.A., Yang, F., Bouchet, V., and *Landry, H.,* 2009: A comparative performance evaluation of the AURAMS and CMAQ air-quality systems. *Atmos. Environ. 43,* 1059–1070.
https://doi.org/10.1016/j.atmosenv.2008.11.027

Stern, R., 2009: *Das chemische Transportmodell REM-CALGRID.* Model description. FU Berlin, 28. Available: www.geo.fu-berlin.de/met/ag/trumf/RCG/RCG-Beschreibung.pdf?1373749582

Stern, R., Builtjes, P., Schaap, M., Timmermans, R., Vautard, R., Hodzic, A., Memmesheimer, M., Feldmann, H., Renner, E., Wolke, R., and *Kerschbaumer, A.,* 2008: A model inter-comparison study focussing on episodes with elevated PM10 concentrations. *Atmos. Environ. 42,* 4567–4588. https://doi.org/10.1016/j.atmosenv.2008.01.068

Tang, H., Pang, J., Zhang, G., Takigawa, M., Liu, G., Zhu, J., and *Kobayashi, K.,* 2014: Mapping ozone risks for rice in China for years 2000 and 2020 with flux-based and exposure-based doses. *Atmos. Environ. 86,* 74–83. https://doi.org/10.1016/j.atmosenv.2013.11.078

Tuovinen, J-P., 2009: Ozone flux modelling for risk assessment: status and research needs. *iForest – Biogeosci. Forestry 2,* 34–37. Online available: www.sisef.it/iforest/show.php?id=485

Turnipseed, A.A., Anderson, D.E., Blanken, P.D., Baugh, W., and *Monson, R.K.,* 2003: Airflows and turbulent flux measurements in mountainous terrain. Part 1. Canopy and local effects. *Agr. Forest Meteorol. 119,* 1–21. https://doi.org/10.1016/S0168-1923(03)00136-9

Turnipseed, A.A., Blanken, P.D., Anderson, D.E., and *Monson, R.K.,* 2002: Energy budget above a high-elevation subalpine forest in complex topography. *Agr. Forest Meteorol. 110,* 177–201. https://doi.org/10.1016/S0168-1923(01)00290-8

Turnipseed, A.A., Burns, S.P., Moore, D.J.P., Hu, J., Guenther, A.B., and *Monson, R.K.,* 2009: Controls over ozone deposition to a high elevation subalpine forest. *Agr. Forest Meteorol. 149,* 1447–1459. https://doi.org/10.1016/j.agrformet.2009.04.001

Uddling, J., Hall, M., Wallin, G., and *Karlsson, P.E.,* 2005: Measuring and modelling stomatal conductance and photosynthesis in mature birch in Sweden. *Agri. Forest Meteorol. 132,* 115–131. https://doi.org/10.1016/j.agrformet.2005.07.004

Van Loon, M., Vautard, R., Schaap, M., Bergström, R., Bessagnet, B., Brandt, J., Builtjes, P.J.H., Christensen, J.H., Cuvelier, K., Graf, A., Jonson, J.E., Krol, M., Langner, J., Roberts, P., Rouil, L., Stern, R., Tarrasón, L., Thunis, P., Vignati, E., White, L., and *Wind, P.,* 2007: Evaluation of long-term ozone simulations from seven regional air quality models and their ensemble. *Atmos. Environ. 41,* 2083–2097. https://doi.org/10.1016/j.atmosenv.2006.10.073

Van Wijk, M.T., Dekker, S.C., Bouten, W., Bosveld, F.C., Kohsiek, W., Kramer, K., and *Mohren, G.M.J.,* 2000: Modeling daily gas exchange of a Douglas-fir forest: comparison of three stomatal conductance models with and without a soil water stress function. *Tree Physiol. 20,* 115–122. https://doi.org/10.1093/treephys/20.2.115

Vautard, R., Builtjes, P.H.J., Thunis, P., Cuvelier, K., Bedogni, M., Bessagnet, B., Honoré, C., Moussiopoulos, N., Pirovano G., Schaap, M., Stern, R., Tarrason, L., and *Van Loon, M.,* 2007: Evaluation and intercomparison of Ozone and PM10 simulations by several chemistry transport models over four European cities within the CityDelta project. *Atmos. Environ. 41,* 173–188. https://doi.org/10.1016/j.atmosenv.2006.07.039

Wesely, M., 1989: Parameterization of surface resistance to gaseous dry deposition in regional-scale, numerical models. *Atmos. Environ. 23,* 1293–1304. https://doi.org/10.1016/0004-6981(89)90153-4

Wesely, M.L. and *Hicks, B.B.,* 1977: Some factors that effect the deposition rates of sulfur dioxide and similiar gases on vegetation. *J. Air Pollut. Control Assoc. 27,* 1110–1116. https://doi.org/10.1080/00022470.1977.10470534

World Meteorological Organization, 2008: Guide to meteorological instruments and methods of observation, Geneva, Switzerland: Secretariat of the World Meteorological Organization.

Wu, Z., Wang, X., Chen, F., Turnipseed, A.A., Guenther, A.B., Niyogi D.,, Charusombat, U., Xia, B., Munger, J.W. and*, Alapaty, K.,* 2011: Evaluating the calculated dry deposition velocities of reactive nitrogen oxides and ozone from two community models over a temperate deciduous forest. *Atmos. Environ. 45*, 2663–2674. https://doi.org/10.1016/j.atmosenv.2011.02.063

Zhang, L., Brook, J.R., and *Vet, R.,* 2003: A revised parameterization for gaseous dry deposition. *Atmos. Chem. Phys. 3,* 2067–2082. https://doi.org/10.5194/acp-3-2067-2003

Zhang, L., Moran, M.D., Makar, P.A., Brook, J.R., and *Gong, S.,* 2002: Modelling gaseous dry deposition in AURAMS: a unified regional air-quality modelling system. *Atmos. Environ. 36,* 537–560. https://doi.org/10.1016/S1352-2310(01)00447-2

IDŐJÁRÁS

Extreme precipitation events in the Polish Carpathians and their synoptic determinants

Agnieszka Wypych[1], **Zbigniew Ustrnul**[2], **Danuta Czekierda**[2],
Angelika Palarz[1], and **Agnieszka Sulikowska**[1]

[1] *Department of Climatology, Jagiellonian University,*
7 Gronostajowa Str., 30-387 Krakow, Poland

[2] *Institute of Meteorology and Water Management – National Research Institute,*
61 Podlesna St., 01-673 Warszawa, Poland

*Corresponding author E-mail: agnieszka.wypych@uj.edu.pl

Abstract— Heavy rainfalls and consequent floods are the most important extreme events in Central Europe in terms of frequency and economic losses. The purpose of the study is to evaluate regional extreme precipitation events in the Polish Carpathian Mountains as well as to determine the circulation basis for these events. Extreme precipitation values were identified based on daily precipitation totals measured at almost 70 weather stations in the Polish Carpathians between 1951 and 2015. The analysis concentrates on daily mean areal precipitation totals in excess of 100 mm per day as well as 50 and 30 mm, which causes flooding in the Carpathians. All extreme precipitation data were analyzed from a synoptic perspective, with special attention paid to pressure patterns over Central Europe. The analysis confirms that the heaviest rainfalls are affected by the situations with the N-NE airflow. However, analyses with the application of the upper tropospheric data brought some new findings on the precipitation extreme topic. It turned out that most cases with significant rains occurred when the mid-tropospheric advection was from the southern sector (during the typical N and NE advections in the lower part).

Key–words: precipitation totals, extremes, atmospheric circulation, Carpathians

1. Introduction

Atmospheric precipitation is a meteorological element which is most often mentioned as the cause of many environmental and socio-economic extreme phenomena. In Central Europe, especially in southern Poland, south-eastern part of Germany, in Czech Republic, and Slovakia, these are floods of different range. Therefore, the most important in this case is considering extremely high precipitation totals.

The discussion on extremely high precipitation belongs to the most important tasks when meteorological extreme phenomena become an issue. Moreover, as most climatic elements in the temperate zone, also atmospheric precipitation is considerably determined by circulation factors and depends mainly upon the direction and type of oncoming air masses. The topic is relatively well expressed in the literature. It especially concerns the values forcing floods and high waters. Most publications concern the studies of the circulation background of rainfalls in mountains, with dangerous effects of the high totals (i.e., *Cebulak*, 1992; *Cebulak* and *Niedźwiedź*, 2000; *Ustrnul* and *Czekierda*, 2001; *Niedźwiedź*, 2003; *Mudelsee et al.*, 2004; *Brázdil et al.*, 2005; *Niedźwiedź et al.*, 2009, *Kundzewicz et al.*, 2012; *Łupikasza* and *Niedźwiedź*, 2015, *Niedźwiedź et. al*, 2015, *Łupikasza, 2016*), some of them are with special attention to considerable floods dated July 1970 (*Morawska-Horawska*, 1971), July 1997 (*Pavlik* and *Sandev*, 1997), and May 2010 (*Bissoli et al.*, 2011; *Kašpar et al.*, 2013). There are also publications treating the issue of extreme flood comprehensively with all the hydrological, environmental, as well as socio-economical results (e.g., *Müller et al.* 2009), flood monographs of 1997 and 2010 (*Grela et al.*, 1999; *Maciejewski et al.*, 2011) with the latest publication describing flood risk in Europe (*Kundzewicz*, 2012) or in upper Vistula river basin (*Kundzewicz et al.*, 2016).

The purpose of the paper is to evaluate regional extreme precipitation events taking place over the course of the last several decades as well as to determine the circulation basis for these events in the Polish Carpathians, a great part of which belongs to the Western Carpathian Mountains. That area is regarded as the primary source area of dangerous floods in Poland (*Niedźwiedź et al.*, 2015, *Twardosz et al.*, 2016, *Kundzewicz et al.*, 2016). Given that most extreme precipitation events cause floods and high waters, one purpose of the paper is also to describe the circulation determinants of these extreme hydrological events.

2. Material and methods

The area of interest - located in Poland - covers about 80 000 km^2 (*Fig. 1*) and is distinguished by very differentiated hypsometry: from lowland landscape on the north, through highlands and foothills, up to the highest tops of the Tatra Mountains (over 2600 m a.s.l.) a bordering range with Slovakia. The altitude reaches 350 m a.s.l. on average, however, the region is famous for its diverse

elevation. Therefore, climatologically, Polish Carpathians are also the most complex area in Poland. Their relief features are important in the formation of their local weather conditions and climate patterns. The mountains constitute the latitudinal orographic barrier, which is additionally forcing the condensation of the water vapor.
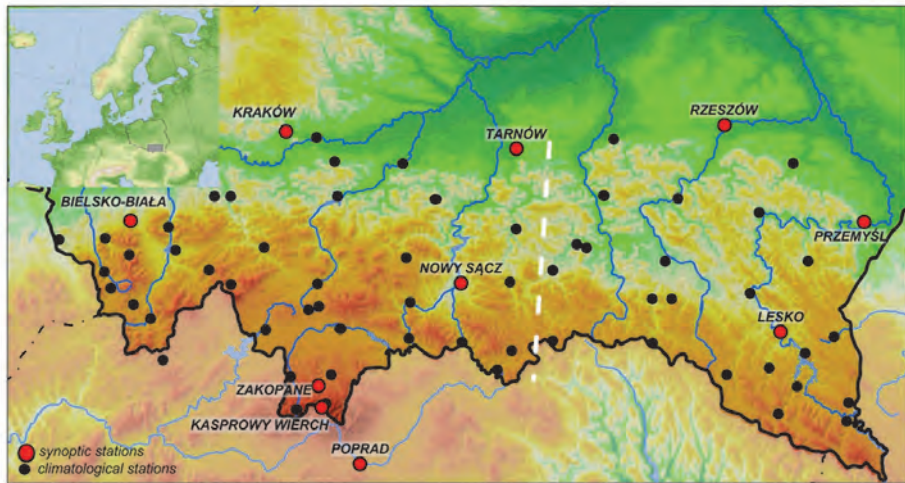

Fig. 1. Location of measuring points mentioned in the study (dashed line: virtual border between the western and eastern parts of the Carpathians).

Daily precipitation totals from almost 70 measuring points (synoptic as well as climatological stations from the Polish Carpathians territory) were taken into account (*Fig. 1*). Two other stations – for validation purposes – have been also taken from the Slovak side of the Western Carpathians. The main research material was based on data from the 65-year period of 1951–2015. This period covers the longest time horizon, for which it was possible to create homogenous meteorological observation series. Precipitation totals have been thoroughly checked, not only in a formal sense, but also in spatial terms where necessary. Needless to say, the issue of measurement data homogeneity is crucial in any analysis of climate issues. Even the slightest errors in the used data, which are often undetectable by standard control procedures, can lead to completely false conclusions. This also applies to issues where extreme values are estimated. Special care needs to be taken when analyzing such data, and, in fact, special efforts were made to make sure that the data used herein are error free.

While examining extremes, including precipitation extremes, a question about their unique nature emerges. It needs to be stated, when the extreme threshold is only a local or regional one and when, reaching certain magnitude, it can become worldwide. Therefore, weather extremes as well as precipitation extremes should be discussed at first at a regional or even local scale, where they are the most important due to their influence.

The paper focuses on daily mean areal precipitation totals in excess of 50 mm per day as well as 30 mm, 10 mm, and 5 mm over the course of two or three days of continuous precipitation, which causes flooding in the Carpathians. Also the incidents of daily precipitation totals over 100 mm at selected stations were taken into account. The paper analyzes long-term variability in flooding patterns. All extreme precipitation data were analyzed from a synoptic perspective, with special attention paid to pressure patterns over Central Europe. Therefore, Grosswetterlagen classification (*Werner* and *Gerstengarbe*, 2010) was included because of its widespread use in Europe and the possibility to refer the obtained results to other international research and local circulation types classification by *Niedźwiedź* (2016), which has been proved to be useful in research conducted for the Western Carpathians (*Cebulak*, 1992; *Niedźwiedź et al.*, 2015). A detailed description of the types of circulation for each of the used calendars is provided in the works cited, whereas a summary of the circulation types for each of the two schemes is provided by *Ustrnul* and *Czekierda* (2009).

Simultaneously, other relevant data and materials have been used. Above all, the data on air mass advection defined on the basis of the data from NCEP/NCAR reanalyses for several grid points from the area of interest. Special attention was paid to the data originating from the grid point 50°N and 20°E. Basing on this data, the directions and strength of airflow at upper atmospheric levels (850, 700 and 500 hPa) were determined. Finally, additional synoptic materials (e.g., charts, aerological diagrams, etc.) have been used and studied.

The crucial part of calculations consisted of the analysis of the frequency of occurrence of daily precipitation totals in particular ranges, i.e., over 5 mm, 10 mm, 20 mm, and 30 mm. The sums constituted the so-called mean areal precipitation was calculated as the arithmetic mean of precipitation sums recorded at a given station. Such an approach was possible due to a relatively even spread of measuring sites.

In the study, particular attention was paid to the extremely high precipitation, which did not occur at single geographic locations (e.g., one station) but was recorded by at least few stations. This allowed us to avoid the discussion about precipitation of a very local nature which causes are fairly complex, most often local, and it is difficult to describe the direct circulation conditions accompanying its formation.

At the same time, separate analyses were carried out for the totals recorded at the individual stations. This involved the extreme events, when the mean areal precipitation exceeded 30 mm. All of the distinguished cases were then analyzed in respect of circulation types.

3. Results and discussion

Spatial differentiation of precipitation totals constantly refers to the relief (*Fig. 1*). The highest amounts, reaching up to 2000 mm annually, appear in the mountains; while not more than 700 mm are typical for the forelands (northern part of the area). Summer precipitation is dominated by the highest amounts of about 100-250 mm in July. It is worth mentioning that spatial differences in precipitation pattern between the western and eastern parts of the area can be seen (*Fig. 1*). It is also evident in the high values of extreme precipitation. Therefore a detailed analysis was conducted for the two regions separately.

In the Polish Carpathians, during the period of 1951–2012, totals did exceed 100 mm at many stations (*Table 1*), and the highest total occurred in the mountains with the absolute maximum (ever recorded at the synoptic station) on Kasprowy Wierch Mt., where on June 30, 1973, the daily precipitation total was 232 mm. It is worth adding that on the same day, at the neighboring Hala Gąsienicowa Climate Station, there were 300 mm of rainfall. To this day, this value is considered the highest measured rainfall value in Poland, and it is rather close to the Central European maximum 345.1 mm reached on July 29, 1897 at the Czech station Nová Louka in Jizerské Hory Mts (*Munzar et al.*, 2011).

Table 1. Events with the highest daily precipitation totals and the associated circulation types by the local Niedźwiedź classification (TN) and the Grosswetterlagen classification (GWL) *

MAX (mm)	date	station	number of stations with RR>100 mm	TN	GWL	areal mean (mm)
300.0	Jun 30, 1973	Hala G.	6	Nc	HM	52.3
224.0	Jul18, 1970	Szczyrk	19	Nc	TrM	83.4
223.5	Jul 8, 1997	Hala G.	6	Nc	Na	52.4
213.0	Aug 31, 2010	Szczyrk	5	NEc	TrM	45.9
190.8	Jul 25, 2001	Maków Podh.	1	Nc	BM	23.2
173.0	Jul 18, 1962	Hala G.	3	NEc	U	43.4
172.8	May 16, 2010	Brenna	10	NEc	TrM	75.3
169.2	Aug 21, 1972	Brenna	5	Nc	TrM	50.9
161.7	Jun 29, 1958	Szczyrk	5	Nc	HFa	64.9
157.0	Sep 7, 1996	Wisła	2	Nc	HNa	39.0
154.1	Jul 25, 1960	Brenna	3	Nc	NWz	49.0

* if extreme precipitation was recorded at more than one station at a day, only the maximum totals are presented

Having analyzed particular circulation types, it can be stated that the majority of extremely high precipitation totals occurred in cyclone-type situations with airflow from the northern sector (*Table 1*). This applied basically to N and NE directions.

The same patterns can be seen while analyzing areal means. Majority of situations when daily mean areal precipitation totals exceeded 30 mm happened in cyclonic situation with N or NE advections and in a cyclonic trough (*Fig. 2*).
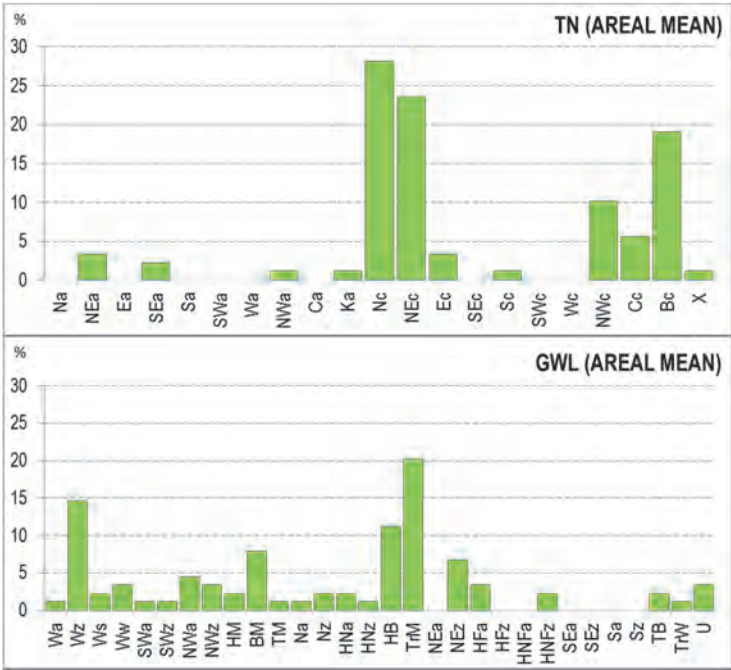

Fig. 2. Frequency of extreme daily precipitation totals over 30 mm in the Polish Carpathians in particular circulation types.

It is worth mentioning that the maximum daily precipitation totals occurred at only several stations during periods of a stationary low pressure center, and at a slightly higher number of stations during a cyclonic pattern with NE airflow (*Fig. 2*).

The circulation background, however, seems to differ spatialy (*Fig. 3*). For the western part of the area of interest, extreme precipitation is most frequently associated with the beforementioned Nc, NEc, and also cyclonic through (Bc) situations, whereas to the east, the impact of high pressure system with advection from eastern sector and NW can also be seen (*Fig. 3*).
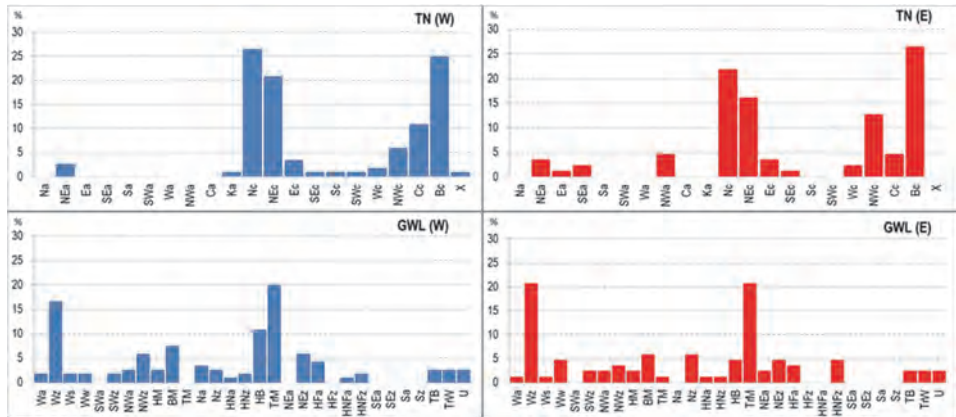

Fig. 3. Frequency of extreme daily precipitation totals over 30 mm in the western (W) and eastern (E) parts of the Polish Carpathians in particular circulation types.

It is worth mentioning (as it was previously stated) that the amount of precipitation reaching the west is much higher. The mean areal maxima recorded for the region are over 90 mm, while the eastern part does not get more than 56 mm of rain, what was the maximum for 1966 (*Fig. 4*).
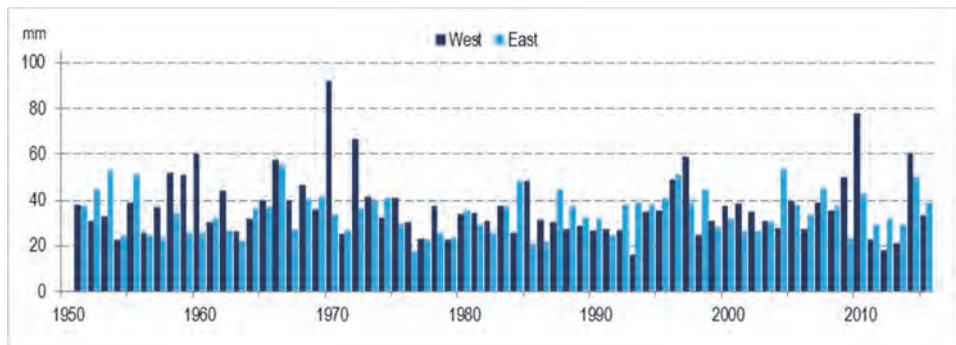

Fig. 4. Extreme daily precipitation totals (mm) – areal mean of western and eastern part of the Polish Carpathians.

For 68 measuring points, the highest daily mean areal precipitation totals were over 70 mm in 1970, more than 60 mm were recorded in 2010, but it is shown that while the whole area is taken into consideration, the areal extremes are lower and less frequent (there are some years without aeral mean over 30 mm – *Fig. 5*).
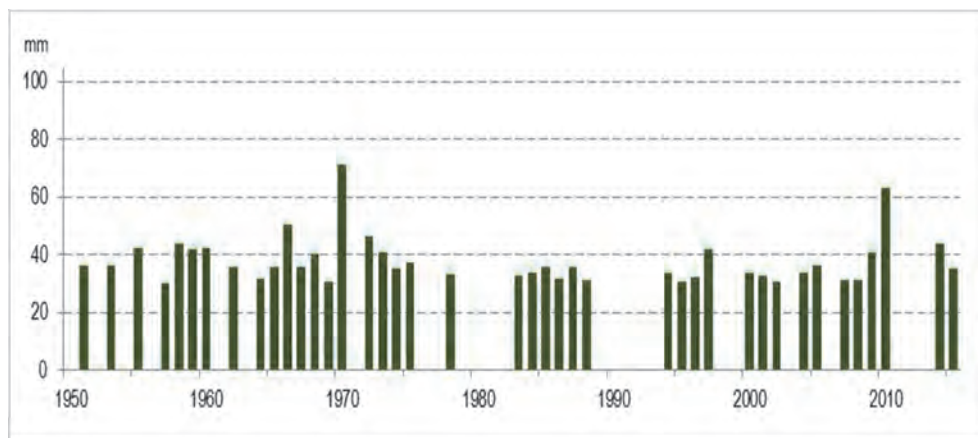

Fig. 5. Extreme daily precipitation totals (mm) – the highest areal mean over 30 mm is in the Polish Carpathians.

The regularity described above becomes clearly seen with stronger criteria. Days with daily mean areal precipitation exceeding 50 mm were selected. *Table 2* presents the exceptional events when the amount of water provided for each sq. meter was higher than 50 liters. Such an extreme situation happened twice more frequent in the western part of the Carpathians. Also, the relationship between precipitation extremes and strong moisture fluxes from the north was substantially more significant for the western than for the eastern part of Polish Carpathians.

Those distinguished extremes and their circulation background (*Table 2*) proved also the slight difference in circulation impact along the mountain range in southern Poland. Almost all of the events (except for two) in the western part were associated with Nc, NEc situations, while the role of circulation types in the eastern part is less univocal. There are 6 different types influencing such high daily mean areal precipitation totals (*Table 2*).

Table 2. Events with extreme (over 50 mm) daily precipitation areal mean in the western and eastern Polish Carpathians and the associated circulation type by TN and GWL classifications

West				East			
Areal mean (mm)	Date	TN	GWL	Areal mean (mm)	Date	TN	GWL
103.8	Jul 18, 1970	Nc	TrM	66.2	Sep 06, 1996	Nc	HNa
85.8	May 16, 2010	NEc	TrM	59.0	Aug 2, 1963	Ea	HFa
70.8	Jun 29, 1958	Nc	HFa	58.9	Aug 27, 1966	NEc	HNFz
69.3	Aug 8, 1997	Nc	Na	57.1	Jul 27, 2004	Nc	TrM
68.1	Aug 21, 1972	Nc	TrM	52.8	Aug 24, 1953	Nc	Wz
63.6	Jul 25, 1960	Nc	NWz	52.1	Jul 18, 1968	Cc	Nz
62.7	May 29, 1966	Nc	HB	51.3	Jun 21, 1955	Bc	Ww
60.9	Aug 31, 2010	NEc	TrM	50.2	Sep 4, 2007	NWc	NWz
56.9	Aug 20, 1972	NEc	TrM				
55.7	Jun 30, 1973	Nc	HM				
54.6	Sep 7, 1996	Nc	HNa				
53.2	Aug 22, 2009	Bc	BM				
52.7	Aug 8, 1985	Nc	TrM				
52.6	Jul 18, 1962	NEc	U				
50.9	Jul 13, 1960	NEc	Wa				
50.6	Jun 30, 1959	NWc	TrM				

As it has already been mentioned, that the information on the circulation of upper level was also used in this work. So far, such an approach has not been fully discussed as no quantitative information was accessible. The data from the reanalyses allowed to investigate the influence of circulation for the whole research period. The analyses of particular cases proved that the data from the 700 or 300 hPa levels does not provide any substantial information. For this reason, only data from the 500 hPa level, which represents mid-tropospheric conditions, was taken into consideration.

As first, the situations determining the highest values of precipitation in the Western Carpathians, i.e., those associated with the advection from the N sector were investigated. In these cases, the analysis of the direction of the airflow at the 500 hPa level was carried out. It turned out that in mid-troposphere the advection from the southern sector (especially from the SW) is observed in instances with most daily totals (about 50% of all cases) (*Fig. 6a*). This regularity is noticeable in almost every class of daily mean areal precipitation totals, and it can be observed at individual stations. At the Krakow station, located at the foreland of the Carpathians, the SW direction at the 500 hPa level is even more significant (*Fig. 6b*).
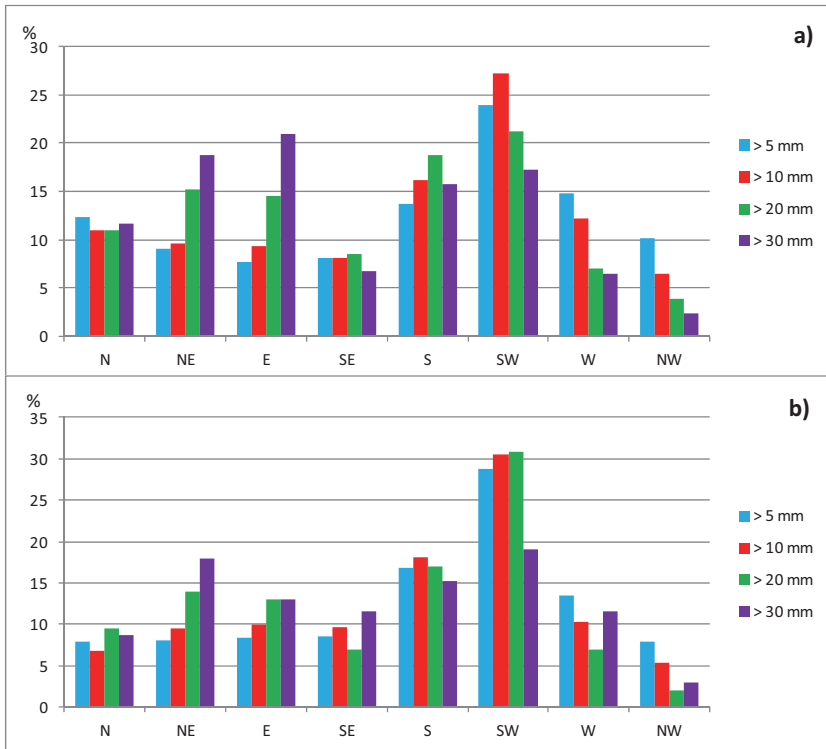
Fig. 6. Frequency of daily precipitation totals over selected thresholds in the particular direction airflows at the 500 hPa level (northern sector airflow at 1000 hPa) - a) areal mean, b) Krakow station.

Analogous relationships can also be found for other weather stations. It means that both low- and mid-level atmospheric circulation influence high precipitation totals. The impact of local conditions of terrain on heavy rainfalls is significantly smaller than the direction of the airflow in the low- and mid-troposphere. This regularity is evident over the whole area, including the areas outside the borders of Poland. The calculations carried out for the two stations in Slovakia expose the same regularity. *Fig. 7* shows the frequency of significant precipitation in Poprad, located between the main ranges of the Tatra and the Low Tatra Mountains., in fact situated in the very heart of the Western Carpathians.
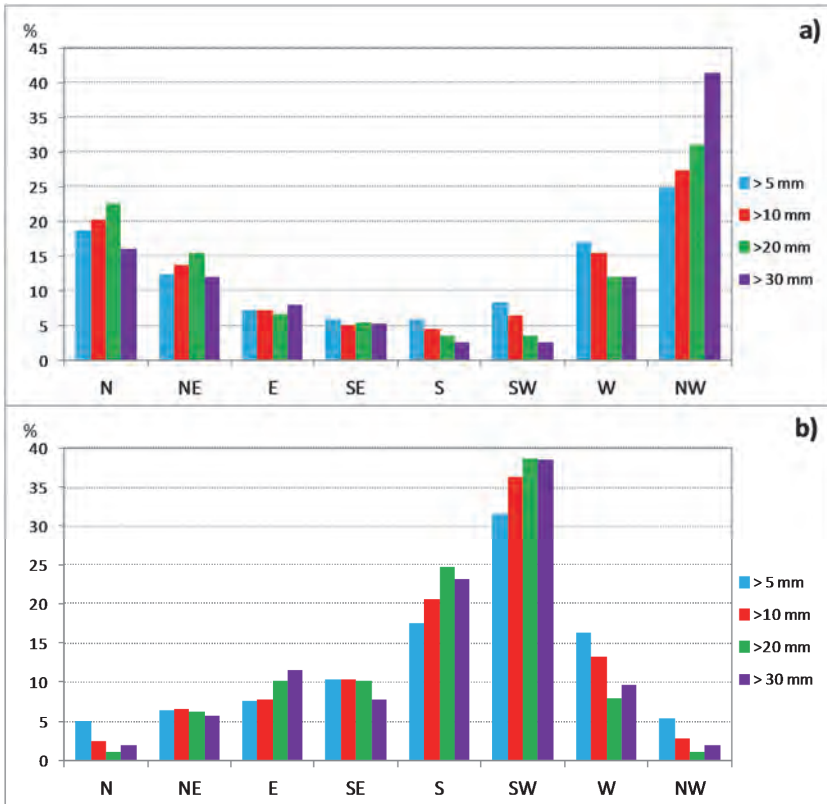
Fig. 7. Frequency of daily precipitation totals over selected thresholds in the particular direction airflows at Poprad station – a) at 1000 hPa level, b) at 500 hPa level during northern sector airflow at 1000 hPa.

Significant precipitation totals occur during the northern sector airflow, reaching 60% of all cases in the lower troposphere (*Fig. 7a*). The frequency rises up to 70% when daily totals over 30 mm are considered. *Fig. 7b* shows the distribution of precipitation from different directions in the mid-troposphere (500 hPa level), when in the low-troposphere airflow from the northern sector is observed. Evidently, in all of the ranges of daily precipitation totals, the southern sector is dominant with the SW direction in particular.

4. Conclusions

The study, based on the largest number of measurement data available and compiled for the Polish Carpathians for over a 60-year-long period, shows the differentiation of the highest values of daily precipitation totals. The work proves that practically at every station, the values can exceed 100 mm. From hydrological point of view, for the research area, these can be regarded as extreme values. Precipitation totals recorded within the analyzed period locally reached up to 300 mm/day, what gave over 100 mm from the regional point of view (areal mean). However, distinct differences between the western and eastern parts of the Polish Carpathians have been detected.

The analysis confirmed the considerable influence of the atmospheric circulation upon significant precipitation totals including even extreme values. Extreme daily precipitation totals in the Polish Carpathians, which are usually the reasons for floods in southern Poland, are the results of a shallow low-pressure system hovering over -Ukraine (north and north-easterly cyclonic types and trough over Central Europe), often with front system causing cyclone-type airflow from the north and northeast. During the mentioned synoptic situations, cool air masses coming in from the north and northeast cause heavy precipitation events (dynamic rise of air over the mountain barrier increases the amount of precipitation). The analysis confirmed the meaning of the Vb cyclone track described by van Bebber (distinguished already in 1891) (*van Bebber*, 1891), which was confirmed in the contemporary studies for Central Europe (e.g., *Mudelsee et al.*, 2004; *Seibert et al.*, 2007).

Analyses with the application of the upper tropospheric data brought some new insight into precipitation extremes causes. It turned out that most cases with significant rains occurred, when the advection in the mid-troposphere was from the southern sector (during the typical N, NE advection in the lower part). Such a situation may be explained with the fact that the collision of warm southerly air, which transports huge amounts of water, with cool air from the north leads to intensive condensation that sometimes results in local thunderstorms with heavy rainfalls. To a certain degree, this situation reminds us of the situation with the so-called Spanish Plume extreme events over the United Kingdom (*Webb et al.*, 2001; *Webb*, 2011), as well as severe hydrometeorological events over Finland and the Baltic states (e.g., *Punkka* and *Bister*, 2005).

The study did not concern very local events with torrential rain of short duration which could produce flash floods. During these events, the maximum intensity of downpours can exceed 100–150 mm within 1–2 hours. As much better time-resolution data is required to conduct such analyses, they are not possible yet due to the lack of the relevant long-time data series.

References

Bissolli, P., Friedrich, K., Rapp, J., and *Ziese, M.,* 2011: Flooding in eastern central Europe in May 2010 - reasons, evolution and climatological assessment. *Weather 66,* 147–153. https://doi.org/10.1002/wea.759

Brázdil, R., Dobrovolný, P., Elleder, R., Kakos, V., Kotyza, O., Květoň, V., Macková, J., Müller, M., Štekl, J., Tolasz, R., and *Valášek, H.,* 2005: Historical and recent floods in the Czech Republic. Masaryk University in Brno, Czech Hydrometeorological Institute in Prague, Brno-Prague.

Cebulak, E., 1992: Wpływ sytuacji synoptycznej na maksymalne opady dobowe w dorzeczu górnej Wisły *Folia Geographica, Ser. Geographica Physica 23,* 81–95. (in Polish)

Cebulak, E., and *Niedźwiedź, T.,* 2000: Zagrożenie powodziowe dorzecza górnej Wisły przez wysokie opady atmosferyczne. *Monografie Komitetu Gospodarki Wodnej PAN 17,* 55–70 (in Polish)

Die Grosswetterlagen Europas. http://www.dwd.de/GWL (assessed May 3, 2016)

Grela, J., Słota, H., and *Zieliński, J. (eds.),* 1999: Dorzecze Wisły – Monografia powodzi lipiec 1997. Institute of Meteorology and Water Management, Warsaw. (in Polish)

Kašpar, M., Müller, M., and *Pecho, J.,* 2013: Comparison of meteorological conditions during May and August 2010 floods in Central Europe. *AUC Geographica 48,* 27–34. https://doi.org/10.14712/23361980.2015.2

Kundzewicz, Z.W., Dobrowolski, A., Lorenc, H., Niedźwiedź, T., Pińskwar, I., and *Kowalczak, P.,* 2012: Floods in Poland. In (ed.: Kundzewicz, Z.W.) Changes in Flood Risk in Europe. Special Publication No. 10, IAHS Press, Wallingford, Oxfordshire, UK, *319–334.* https://doi.org/10.1201/b12348

Kundzewicz, Z.W. (ed.), 2012: Changes in Flood Risk in Europe. CRC Press.

Kundzewicz Z.W., Stoffel M., Niedźwiedź T., and *Wyżga B. (eds.),* 2016: Flood Risk in the Upper Vistula Basin. GeoPlanet: Earth and Planetary Sciences, Springer. https://doi.org/10.1007/978-3-319-41923-7

Łupikasza, E. and *Niedźwiedź, T.,* 2015: Wieloletnia zmienność typów cyrkulacji sprzyjających występowaniu wysokich opadów atmosferycznych w Tatrach (1873-2014). In (eds.: Lorenc, H. and Ustrnul, Z.) Klimat a Społeczeństwo i Gospodarka. Polskie Towarzystwo Geofizyczne Oddział Warszawski, Instytut Meteorologii i Gospodarki Wodnej Państwowy Instytut Badawczy, Warszawa: 93–111. (in Polish)

Łupikasza, E., 2016: The Climatology of Air- Mass and Frontal Extreme Precipitation. Springer Atmospheric Sciences, Springer. https://doi.org/10.1007/978-3-319-31478-5

Maciejewski, M., Ostojski, M.S., and *Walczykiewicz, T.* (eds.), 2011: Dorzecze Wisły – Monografia powodzi maj-czerwiec 2010. Institute of Meteorology and Water Management – National Research Institute, Warsaw (in Polish)

Morawska-Horawska, M., 1971: Meteorologiczne przyczyny powodzi w Polsce południowej w lipcu 1970 roku. *Przeglad Geofizyczny 4,* 299–315 (in Polish)

Mudelsee, M., Börngen, M., Tetzlaf, G., and *Grünewald, U.,* 2004: Extreme floods in Central Europe over the past 500 years: role of cyclone pathway "Zugstrasse Vb". *J. Geophys. Res. 109(D23101),* 1–21. https://doi.org/10.1029/2004JD005034

Müller, M., Kašpar, M., and *Matschullat, J.,* 2009: Heavy rains and extreme rainfall-runoff events in Central Europe from 1951 to 2002. *Nat. Hazards Earth Syst. Sci. 9,* 441–450. https://doi.org/10.5194/nhess-9-441-2009

Munzar, J., Ondráček, S., and *Auer, I.,* 2011: Central European one-day precipitation records. *Moravian Geographical Reports 19,* 32–40.

Niedźwiedź, T., 2003: Extreme precipitation events on the northern side of the Tatra Mountains. *Geogr. Polonica 76,* 13–21.

Niedźwiedź, T., 2016: Catalogue of synoptic situations in the upper Vistula river basin (1873.09–2015.12). http://klimat.wnoz.us.edu.pl

Niedźwiedź, T., Łupikasza, E., Pińskwar, I., Kundzewicz, Z.W., Stoffel, M., and *Małarzewski, Ł.,* 2015: Variability of high rainfalls and related synoptic situations causing heavy floods at the northern foothills of the Tatra Mountains. *Theor. Appl. Climatol. 119,* 273–284. https://doi.org/10.1007/s00704-014-1108-0

Niedźwiedź, T., Twardosz, R., and *Walanus, A.,* 2009: Long-term variability of precipitation series in east central Europe in relation to circulation patterns. *Theor. Appl. Climatol. 98,* 337–350.

Pavlik, J. and *Sandev, M.,* 1997: Synoptické hodnoceni povětrnostnichsituaci v průběhupovodně v červenci 1997. *Meteorologickéz právy 50, 164–171.* (in Czech)

Punkka, A.J. and *Bister, M., 2005:* Occurrence of summertime convective precipitation and mesoscale convective systems in Finland during 2000–01. *Month. Weather. Rev. 133,* 362–373. https://doi.org/10.1175/MWR-2854.1

Seibert, P., Frank, A., and *Formayer, H.,* 2007: Synoptic and regional patterns of heavy precipitation in Austria. *Theor. Appl. Climatol. 87,* 139–153. https://doi.org/10.1007/s00704-006-0198-8

Twardosz, R., Cebulska, M., and *Walanus, A.,* 2016: Anomalously heavy monthly and seasonal precipitation in the Polish Carpathian Mountains and their foreland during the years 1881-2010. *Theor. Appl. Climatol. 126,* 323–337. https://doi.org/10.1007/s00704-015-1570-3

Ustrnul, Z. and, *Czekierda, D*., 2001: Circulation background of the atmospheric precipitation in central Europe (based on the Polish example). *Meteorol. Z. 10(3),* 103–111. https://doi.org/10.1127/0941-2948/2001/0010-0103

Ustrnul, Z., D. and *Czekierda,* 2009: Atlas of extreme meteorological phenomena and synoptic situations in Poland. IMGW, Warszawa, 182.

van Bebber, W.J., 1891: Die Zugstrassen der barometrischen Minima. *Meteorol. Z., 8,* 361–366.

Webb, J.D.C., 2011: The great summer heatwaves of 1975-1976 in the UK, and some violent storms. *Int. J. Meteorol. 36,* 255–261.

Webb, J.D.C., Elsom, D.M. and *Reynolds, D.J.,* 2001: Climatology of severe hailstorms in Great Britain. *Atmos. Res. 56,* 291–308. https://doi.org/10.1016/S0169-8095(00)00081-8

Werner, P.C. and *Gerstengarbe, F-W.,* 2010: Katalog der Großwetterlagen Europas (1881–2009) nach Paul Hess und Helmut Brezowsky, 7. verbesserte und ergänzte Auflage. *PIK Report 119.* www.dwd.de/GWL

IDŐJÁRÁS

Expected changes in the length of *Anopheles maculipennis* (Diptera: Culicidae) larva season and the possibility of the re-emergence of malaria in Central and Eastern Europe and the North Balkan region

Attila J. Trájer[1,2*], **Tamás Hammer**[3]

[1] *Institute of Environmental Engineering,*
University of Pannonia,
Egyetem Str. 10, H-8200 Veszprém, Hungary

[2] *Department of Limnology, University of Pannonia,*
Egyetem Str. 10, H-8200 Veszprém, Hungary

[3] *Independent author*

*Corresponding author E-mail: trajer.attila@mk.uni-pannon.hu, attilatrajer@gmail.com

(Manuscript received in final form April 6, 2017)

Abstract—*Anopheles maculipennis* is one of the potential vectors of *Plasmodium vivax* caused malaria in Europe. Although potential malaria vectors are present in the continent, malaria was eradicated in historical times and recently absent in Central and East Europe and the North Balkan. Climate change may trigger the re-emergence of malaria in Europe positively affecting the seasonal patterns of the potential Anopheline vectors. The increasing length of the larva season of mosquito vectors is one of the risk factors of the re-emerging of malaria. The monthly relative abundance values of the larvae of *Anopheles maculipennis* were modeled for the reference period 1961–1990 and the periods 2011–2040 and 2041–2070 based on the REMO climate model for Central and East Europe and the North Balkan region. Strong, significant correlation (r^2=0.94, p<0.0001) was found between the monthly relative abundances of larvae and monthly mean air temperature values in Hungary between March and November. The threshold of the larval activity of *Anopheles maculipennis* was found to be about 4 °C. Comparing the modeled relative abundances for 1961–1990, 2011–2040, and 2041–2070, April and October months showed the most notable changes. The model predicts that in Southeast Hungary, East Croatia, North Serbia, South Romania, and North Bulgaria, the main season will increase by +1 to +2 months to the period of 2041–2070 comparing to the reference period. The model also indicates that the complete main *Anopheles maculipennis* larva season of the mosquito will increase by two months in Southeast Hungary and at least 1 month in the other parts of the south Pannonian Ecoregion, in the North Balkan region including South Romania and North Bulgaria for 2041–2070.

Key-words: ecological modeling, mean monthly temperature, Carpathian Basin, malaria mosquitoes

1. Introduction

Anopheles (Cellia) maculipennis s. s. Meigen, 1818 (hence simply: *An. maculipennis*), the name-giving species of the *Anopheles maculipennis* complex is abundant in Europe, the Middle East, and the Caucasus. *An. maculipennis* is the vector of Batai, Tahyna, Myxoma and West Nile viruses, *Dirofiliaria immitis* Leidy, 1856 and *Dirofilaria repens* Railliet and Henry, 1911 roundworms and *Francisella tularensis* McCoy and Chapin, 1912; Dorofe'ev, 1947 (*Şuleşco et al.*, 2016; *Silbermayr et al.*, 2014; *Huhtamo et al.*, 2013; *Reusken et al.*, 2011; *Filipe et al.*, 1972). *An. maculipennis* and *Anopheles (Cellia) messae* Falleroni, 1926 were the primarily vectors of malaria in the warm and temperate continental climate areas of Europe (*Dfa*, *Dfb* zones according to the Köppen-Geiger climate classification) in historical times (*Bruce-Chwatt* and *Zulueta*, 1980*; Proft et al.*, 1999). In the warm Mediterranean (summer dry) and humid Mediterranean (subtropical) climate areas (*Csa*, *Cfa* zones according to the Köppen-Geiger climate classification), rather the malaria mosquitoes *Anopheles (Cellia) sacharovi* Favre, 1903*, Anopheles (Cellia) superpictus* Grassi, 1899, and *Anopheles (Cellia) labranchiae* Falleroni, 1926 were the principal vectors of malaria before the middle of the 20th century (*Sinka et al.,* 2010; *Gratz*, 2004; *Kiszewski et al.,* 2004). In Greece and the Middle East where malaria is present in the recent times, the members of the *Anopheles superpictus* complex are important, but not the solely anopheline vectors of malaria (*Danis et al.,* 2011; *Oshaghi*, 2008), since *An. maculipennis* is also among those mosquito species which are thought to be the potential recent vectors of *Plasmodium vivax* Grassi and Feletti, 1890 (*Danis et al.*, 2011).

In the Roman era and the Middle Ages, the mainly *P. vivax* caused malaria was common autochthonous vector-borne infection in the warmer (Mediterranean and oceanic) climate areas of the Old Continent. Malaria infected the human populations of the Mediterranean region (*Facchini et al.*, 2004; *Hume*, 2003) or the British Islands (*Gowland* and *Western*, 2012), and malaria was a constant scourge in Roman Italy, including the capital of the Roman Empire (*Temin*, 2006). There are evidences, that *Plasmodium falciparum* Welch, 1897 caused malaria spread only during the late antiquity era in the Mediterranean (*Sallares et al.,* 2004). Based on the risk classification of *Gething et al.* (2010), in 1900, malaria was mesoendemic in the Balkan (excluding the high Dinarids and the Rodope Mountains) and the Hungarian Great Plain and hypoendemic in the other areas of Eastern and Central Europe. In Hungary, at least three potential malaria vector species – namely *An. maculipennis*, *Anopheles (Anopheles) atroparvus* Van Thiel, 1927 and *Anopheles (Cellia) messae* Falleroni, 1926– have been collected in the last decades and the presence of a fourth malaria vector mosquito, *An. superpictus* is also plausible in the southern parts of the country (*Tóth* and *Kenyeres*, 2012). Before 1960, malaria was endemic in Hungary (*Mihályi* and *Gulyás*, 1963) and

the pathogen of the recurrent malaria – *P. vivax* - was the most frequently transmitted malaria pathogen (*Trájer et al.*, 2016). The eradication of malaria was performed through several complex, chemical, hydrological, and epidemiological interventions (*Szénási et al.*, 2003). After the eradication of autochthonous malaria, the annual incidences of imported malaria were less than 0.1 per 100,000 inhabitants in the last two decades in Hungary (*Chakarova et al.*, 2015). In Europe, malaria is endemic recently only in Greece, where *P. vivax* protozoans cause autochthonous cases (*Danis et al.*, 2011).

Nowdays, malaria is still one of the most important vector-borne diseases with global distribution causing more than 300–500 million new cases every year in the world (*Olupot-Olupot* and *Maitland*, 2013; *Caminade et al.*, 2014; WHO, 2002). About 40% of the people of Earth live in malaria endemic areas (*Mendis et al.*, 2001), and only in 2015, malaria caused more than 200 million new cases and resulted about 440 thousand deaths worldwide (*World Malaria Report*, 2015). Despite all efforts, *P. falciparum* caused malaria remained the most important mortality factor for children in the sub-Saharan Africa throughout the entire 20th century (*Craig et al.*, 1999).

The current geographic range of malaria is much smaller than the range of the potential mosquitoes, which phenomena is called as 'Anophelism without malaria' (*Jetten et al.*, 1996). The malaria vector potential of an anopheline mosquito species in a currently malaria-free area is problematic compared to the areas where malaria is still autochthonous. For example, *Sinka et al*. (2010) found that *An. messeae* could be the dominant vector of malaria in Central and East Europe; *Kiszewski et al.* (2004) proposed that *An. atroparvu*s should be the most notable potential malaria vector in the same area. In contrast, based on faunistic studies, in Hungary, it seems that *An. maculipennis* is one order of magnitude more frequent potential malaria vector mosquito than *An. messea*e and two-three magnitudes more abundant than *An. atroparvus* and *Anopheles (Anopheles) algeriensis* Theobald, 1903. Based on the results of the mosquito collection surveys in the 1960's to the 1990's, *An. maculipennis* formed itself the 3% of the total imago mosquito material and more than the 6% of the larva material (*Tóth*, 2004), thus it is the most abundant malaria mosquito in the country. It should be added, that there is experimental evidence that *Anopheles (Cellia) plumbeus* Stephens, 1828 also can transmit human pathogen *Plasmodium* parasites to human beings (*Krüger et al.*, 2001), which species also occur and frequent in Central and East Europe.

The range of malaria is strongly determined by the occurrence of the anopheline vectors and the seasonal activity patterns of both larvae and imagoes of malaria mosquitoes. *Hackett* and *Missiroli* (1935) already in 1935 recognized that the length of the *An. maculipennis* season is determined by latitude which correlates to the spatial patterns of temperature conditions. *Kuhn et al.* (2002) found significant relationships between climatic factors as precipitation, temperature and the presence of the most important malaria vectors in Europe.

The analysis of the former malaria data of Hungary showed that the observed annual run of the incidences of *P. vivax* caused by can be well modeled by the temperature-based activity model of the resident malaria mosquitoes, e.g., the activity of *An. messeae* (*Trájer* and *Hammer*, 2016) indicating+ the importance of ambient temperature on malaria incidence under continental climate conditions.

Now, global climatic change is expected to increase the range and incidence of mosquito- and other arthropod-borne diseases. Climate scenarios predict the increase of temperature, which can increase the risk of the parasite transmissions by increasing the distribution and abundance of vectors, and the length of mosquito vector and parasite seasons (*Russel*, 1998). The effect of climate change on the distribution of malaria mosquitoes is not a fiction: in the period of 1973–2012, the expansion of *An. maculipennis* was observed in northeastern Europe and northwestern Asia (*Novikov* and *Vaulin*, 2014). Parallel to the spread of the vectors, one of the possible results of elevated temperature conditions is the increasing worldwide burden and distribution of malaria (*Lindsay* and *Birley*, 1996; *Loevinsohn,* 1994). *Martens et al.* (1999) predicted that the greatest potential consequences of climate change are that malaria will occur in temperate zones, where the anopheline mosquito vectors are present but the recent cooler climate does not allow the transmission of the parasites. *Kuhn et al.* (2002) showed that climate change can significantly increase the abundance of the European *Anopheles s*pecies.

The investigation of the potential effect of climate change on mosquito larva seasonality can help the development of the near-future mosquito-control protocols. In nature, mosquito populations originally were limited by their predators including, e.g., the predation of swallows (*Brown* and *Sethi*, 2002). In human environment, the decrease of mosquito abundance has serious health and veterinary importance in the mosquito-vectored-endemic areas of the world (*Reiter,* 2001; *Rogers* and *Randolph*, 2000; *Patz et al.,* 1998). The abundance of mosquito-borne diseases also depends on the urbanization intensity (*Trájer et al.*, 2016). The activity of malaria vectors and the seasonal transmission probability of *Plasmodium* species are highly sensitive to climatic conditions (*Martens et al.*, 1995) – mainly the changes of temperature (*van Lieshout et al.*, 2004). Similarly to the larvae of other anopheline mosquitoes, the larvae of *An. maculipennis* also develop through four instars, after which they metamorphose into pupae. The time of development is the function of water temperature where larvae develop, and it indirectly depends on the ambient air temperature. It is known, that elevated ambient temperatures increase the growth rates of mosquito vector populations, since the full ontogeny time of mosquitoes depends on temperature (*Paz* and *Albersheim*, 2008). The larvae of *An. maculipennis* can inhabit the water of smaller watercourses, marshes, brooks, rainwater puddles, and the littoral part of small lakes, or they can live even in dendrotelmata, fitotelmata, technotelmata, or malakotelmata. In the Bakony-Balaton region, Hungary, larvae were continuously

collected from the beginning of April to mid-October, and the main swarming season of imagoes occurred from late June to the end of September (*Tóth*, 2006). The species avoid the salt lakes of the Hungarian Great Plain (*Tóth*, 2004).

We aimed to model the changing seasonality of *An. maculipennis* larvae due to climate change in Central and East Europe and the North Balkan region based on the scenarios of the REMO climate model. We focused on the modeling of the start and end of the mosquito larva season of *An. maculipennis*. It was hypothesized, that the Carpathian Basin is one of the most sensible areas to the anthropogenic climatic change also in the aspect of the changing seasonality patterns of *An. maculipennis*. The seasonal abundance of *An. maculipennis* imagoes practically overlaps with the seasonality of larvae in Hungary. About more than five times higher numbers of larvae were collected than imagoes (2258/12363; *Tóth*, 2004). The higher number of larvae provided more confident correlation between the abundance and temperature.

On the other hand, mosquito larvae are target of the modern biological mosquito control techniques. The populations of mosquito larvae can be reduced by biological control agents, which methods are more selective than the classical pesticide-like adulticides, which chemicals are harmful for the ecosystems in general. The modeling of the predictable seasonality of *An. maculipennis* larvae can help the future mitigation procedures. In the interpretation of the results, we focused also on the biological and social consequences of the changing spatial-temporal patterns of *An. maculipennis* larvae, and we analyzed the probability of the re-emergence of malaria in the light of our findings.

2. Materials and methods

2.1. Mosquito data

The monthly mosquito larva data of *An. maculipennis* were gained from the mosquito monograph of *Tóth* (2004). This monograph contains the data of different mosquito larvae, pupae, and adults based on the literature of the former mosquito collection efforts in Hungary and the author's own surveys. The monograph was based on the data of collections, which were performed basically in the 1960's, 1970's, 1980's, and the 1990's. The abundance data of larvae of *An. maculipennis* were used in monthly temporal distribution. The absolute number of larvae were converted to relative monthly abundance values according to Eq.(1). If the total annual value is 100%, relative monthly abundance value is

$$A_{rm} = \frac{N_m}{N_a} \times 100, \tag{1}$$

where A_{rm} is the relative abundance of a month, N_m is the number of the total collected larvae according to a given month, and N_a is the total number of the collected larvae representing the entire period.

2.2. Climate data and its processing

It was thought that ambient air temperature can be handled as the principal factor of *An. maculipennis* seasonality with specific regard to the start and end of the mosquito larva season, and consequently, temperature can strongly influence the total length of the larva season. This presumption was based on the observations that the poikilothermic *An. maculipennis* mosquitoes breed in small lakes, small lake-like reservoirs, litoprofundal shallow lakes, and swamp-like natural waters (*Tóth*, 2004), which have low heat storage capacity due to the combination of extent water surface and relatively low water depth. This geometry is expressly true for the narrow littoral zone of the waters, where the larvae of *An. maculipennis* can be found.

Two climate data sources were used:

1) The REMO model provided climatic analysis for the reference period and two future periods (2011–2040 and 2041–2070) for modeling purposes.
2) Since the collection period of mosquito larvae (from the 1960's to the end of the 1990's – which practically means the period of 1961–1999 in the present analysis) does not completely overlap the reference period of the REMO model (1961–1990), the E-OBS climate model (from 1950 to now) was used for the preformation of correlation between monthly relative mosquito larva abundances and monthly mean temperature values.

European climate data were obtained from the regional climate model REMO, which was developed in Hamburg (*Jacob et al.*, 1997; *Jacob*, 2001). The horizontal resolution of the used grid is 25 km ×25 km. The model REMO is based on the ECHAM5 global climate model (*Roeckner et al.*, 2003, 2004) and the IPCC SRES A1B scenario. The A1B scenario supposes very fast economic increase, worldwide population peak in the middle of the 21st century, and the introduction of innovative and efficient technologies (*Nakicenovic* and *Swart*, 2000). The reference period of REMO is 1961–1990, the two future periods of modeling are 2011–2040 and 2041–2070. Although the entire European continent is within the domain of REMO, only a part of the grid shown in *Fig. 1A* was used. For the abundance modelling, only one variable, the monthly mean temperature (°C) was used.

To perform the correlation between the relative (%) abundance values and mean temperatures, mean temperature values of the period 1961–1999 were gained from the E-OBS model. The monthly ambient temperature values were averaged according to monthly temporal resolution. The following grid was used which covers almost the whole area of Hungary: from 45.75 to 48.50N and from 16.00 to 23.00 E. The spatial resolution was 0.25°×0.25° (*Fig. 1B*).

164
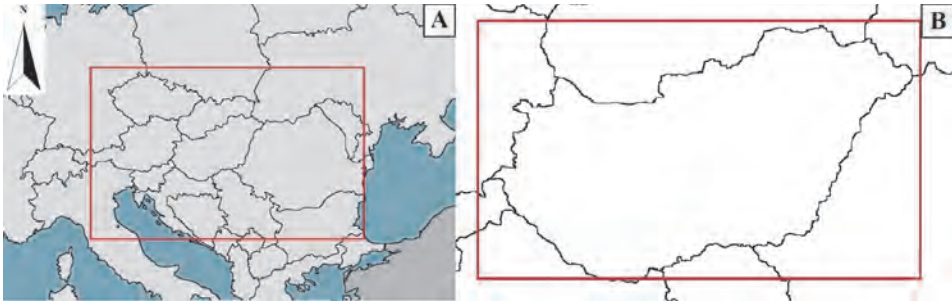
Fig. 1. Domains of the REMO (red rectangle; A) and E-OBS (red rectangle; B) models within of Europe.

2.3. Modeling steps

Comparing the relative monthly abundance data of the larvae of *An. maculipennis* and the monthly mean temperature values, it was observed, that the annual abundance profile of the mosquito larvae starts to increase rapidly above the abundance value of 12% in May, and inversely, the main season ends, when the abundance decreases below this value after September in Hungary. The 12% monthly abundance value was handled as the frame of the main larva season of the mosquito. Only those months were involved into the analysis, when the monthly mean temperature of the period exceeded the 4 C value, which empirically indicates the start/end of the larva season.

GIS processing of the data

ESRI ArcGIS 10.0 software was used for preparing climatic data, running the model, and displaying the model results. First step, the georeferred climate data of REMO climate model were loaded to the program. Using the raster calculator function of ArcGIS, monthly temperature values were converted into monthly relative abundance values based on Eq.(2) (see below). The raster results were converted to polygon-type ESRI shapefile format. The order of the three layers – the modeled relative larva abundance values of the periods 1961–1990, 2011–2040, and 2041–2070 – determined that the result maps can show the mainly northward (spring), southward (autumn), or the seasonal altitudinal shifts of the relative abundance (or activity) of *An. maculipennis* larvae. To create color images, we linked the points with the calculated relative abundance values. The different values were assigned to the referred points and were sorted into attribute table. Then the climatic data were refined by the inverse distance weighted interpolation method of ESRI ArcGIS 10 software. Color codes of relative abundance values were selected according to a 0 to 12 (exactly to 12.24<) scale. Dark red color was used to mark the main season in the maps, when the modeled relative abundance values reach or exceed the 12% annual value; porcelain white color indicate the pre or post-season areas, where there are no active larvae in the natural waters.

3. Results

3.1. Correlation between the monthly relative larva abundances and the temperature

The start of the main season was in April, while the threshold of the larval abundance of *An. maculipennis* was about 4 C in Hungary in the reference period. In the end of the season, the monthly abundance value decreased below the 12% value which occurred in October, while the larval season ended in November in the reference period in Hungary, when the ambient mean temperature sank below 4 C (*Fig. 2*).
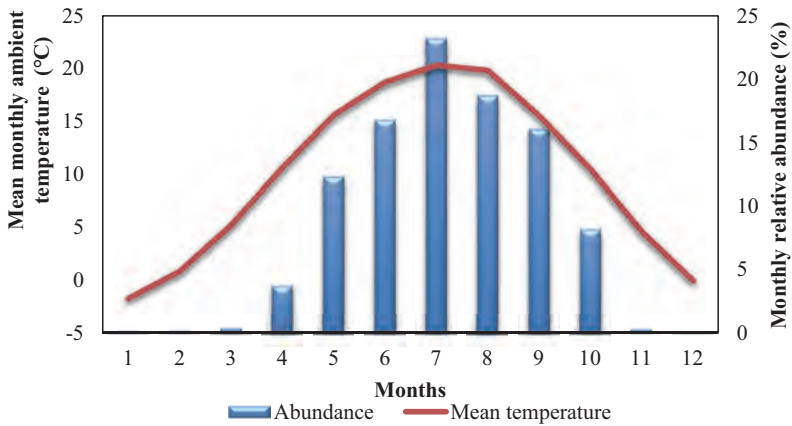
Fig. 2. The run of the monthly relative abundances of *An. maculipennis* larvae in Hungary based on the collected mosquito material of the 1960's to 1990's, and the run of the mean monthly ambient temperature in 1961–1999 averaged according to the selected grid of Hungary.

Strong, significant linear correlation was found between the monthly relative abundances of larvae and the mean ambient temperature values ($r^2=0.94$, $p<0.0001$) from March to November:

$$A_{rm} = 1.3564 * T_m - 7.1749, \tag{2}$$

where A_{rm} is the relative (%) abundance of *An. maculipenis* larvae in a month, T_m is the mean monthly ambient temperature (°C). Eq.(2) was used in the modeling if the projected abundance of the larvae (*Fig. 3*).
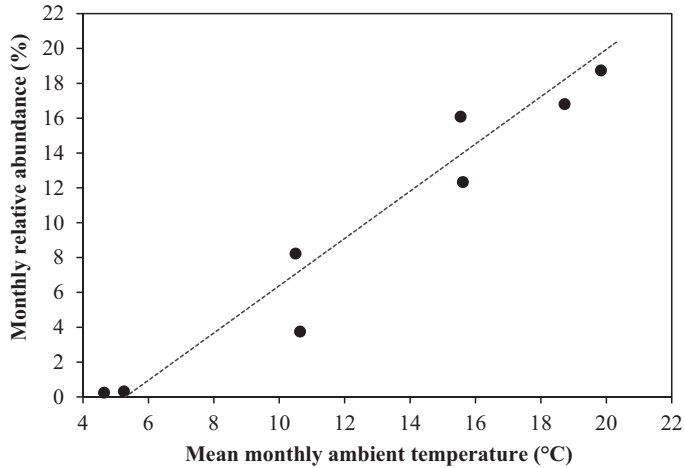
Fig. 3. The correlation between the monthly relative abundances of *An. maculipennis* larvae and the mean monthly ambient temperatures in March to November.

3.2. *Modeled starts of the seasons*

The modeled relative abundance values of *An. maculipennis* larvae showed notable differences in the case of the three different 30-year periods. Comparing the modeled abundances for the reference periods 1961–1990, 2011–2040, and 2041–2070, the most notable spatio-temporal shifts in the main larval seasonality – including the start of the absolute and the main season – was observed in April based on the modeled relative abundances. It was modeled for the reference period, that the main larva season usually did not start until May in Central and East Europe and the North Balkan region except a Romanian lowland section of river Danube. In contrast, for the period 2011–2041 the model predicts, that the main season of the larvae of *An. maculipennis* will start in April in the areas of Vojvodina, Serbia and the Romanian Lowland. For the period 2041–2070, the model predicts broader shift of the main season's start from May to April affecting almost the entire South Pannonian Ecoregion. In Southeast Hungary, East Croatia, North Serbia, South Romania, and North Bulgaria, the total main season will shift by 1 month to the period of 2041–2070. For 2041–2070, the model predicts that the start of the season of the mosquito's larvae in Southeast Germany, the Czech Republic, and the northeastern forelands of the Carpathian Mountains will start one month earlier compared to the reference period (*Fig. 4*).
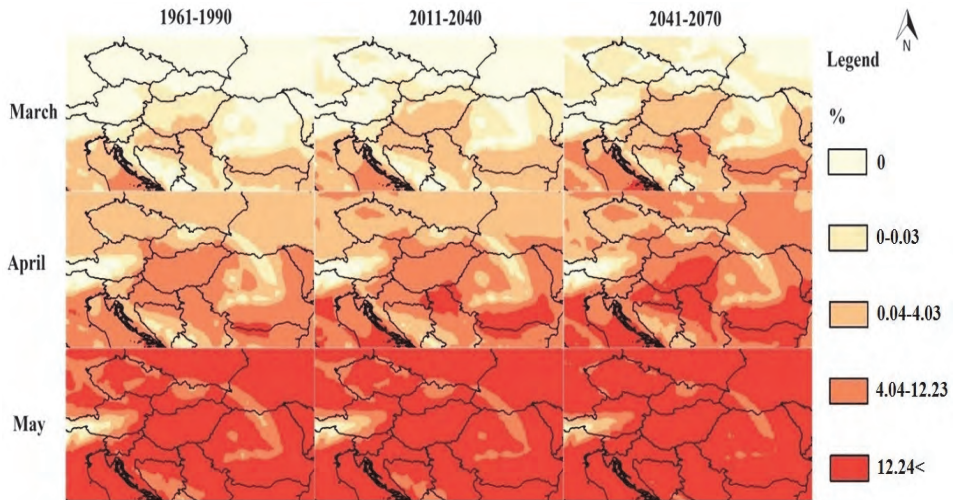
Fig. 4. The predicted monthly relative abundance values of *An. maculipennis* larvae in Central and East Europe and the North Balkan in March, April and May for the periods of 1961–1990, 2011–2040, and 2041–2070.

3.3. Modeled ends of the seasons

The model predicts that the main season of *An. maculipennis* larvae will end one month later in 2041–2070, compared to the reference period, when it ends in October. For 2041–2071, the model predicts that the total season will not end until November in the northern part of Central Europe. For 2041–2070, the model predicts also that the main season of the mosquito's larvae will continue to the end of October in the entire North Balkan and South Pannonian Ecoregion to the end of October. In Hungary, the end of the main season will shift by plus 1 month for the period 2041–2070. Due to the high heat storage capacity of the sea water, the main season of *An. maculipennis* continues to November in the Adriatic coasts. For 2041–2070, the model predicts that the start of the season of the mosquito's larvae in South East Germany, the Czech Republic and the North East forelands of the Carpathian Mountains will end one month later compared to the reference period. The model shows the vertical shift of the season, which is clearly visible in case of the Tranylvanian Middle Mountains. or in the Dinarid Ranges, where the main part of the season also predicted to start earlier and end later by 1–1 month (*Fig. 5*).
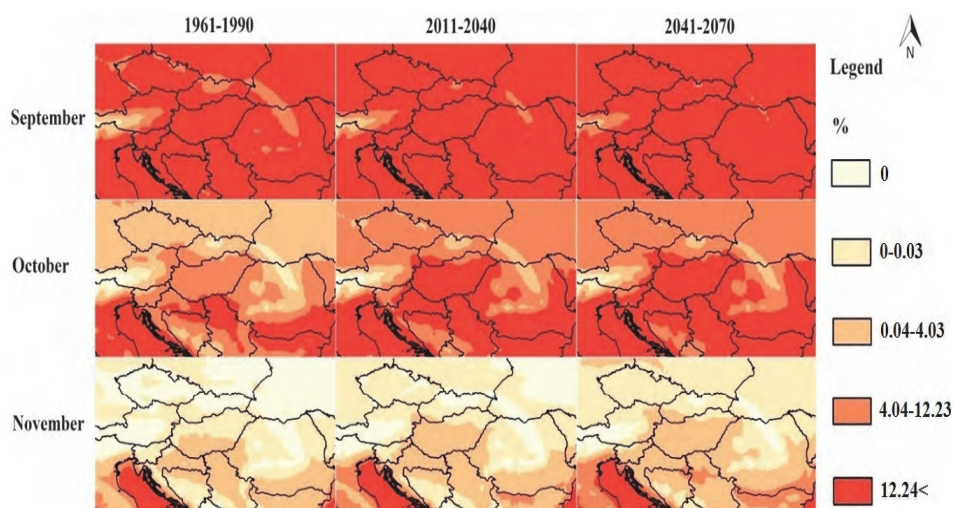
Fig. 5. The predicted monthly relative abundance values of *An. maculipennis* larvae in Central and East Europe and the North Balkan in September, October and November for the periods of 1961–1990, 2011–2040, and 2041–2070.

4. Discussion

The monthly relative abundance values of *An. maculipennis* larvae was modeled for 1961–1990, 2011–2040 and 2041–2070 in Central and East Europe and the North Balkan region based on the REMO climate model and the Hungarian monographic mosquito data of *Tóth* (2004). Our results predict the notable elongation of the larva season for 2011–2040 and 2041–2070 compared to the reference period 1961–1990. The changes of the geographical patterns of the starting and ending months of the main and absolute seasons seem to be not homogenous in the studied region. The fastest increase of the season's length will affect the areas, where large rivers and flood basins occur. The model predicts the most rapid elongation of the larva season of *An. maculipennis* in the central part of the Pannonian Ecoregion and the lower (Romanian and Bulgarian) section of the Danubian Plain. The model shows that the length of the main season is predicted to increase by 2 months for 2041–2070 in the southeastern part of the Hungarian Great Plain, while in the other parts of the Pannonian Ecoregion and the North Balkan, the length of the main season will elongate by less than two months for the second future period. These heterogenic predicted spatial-temporal changes of the activity of larvae can be the potential consequence of the faster warming climate of the Carpathian Basin (and some other floodplain areas in the North Balkan) compared to the other regions of Europe (*Bartholy* and *Gelybó*, 2007).

The above summarized results support the hypothesis that meteorological/ climatic factors, as ambient temperature, influence substantially the spatial-temporal activity patterns of the potential vectors, and indirectly the transmission dynamics of vector-borne diseases such as malaria (*Githeko et al.,* 2000; *Gubler,* 1998; and *Gubler et al.,* 2001). This conclusion is highly true for mosquitoes and mosquito-borne infections (*Reiter*, 2001). The temperature threshold of the vital and blood meal seeking activity of female mosquitoes are different that is also can be true for physiological thresholds of the vector mosquitoes and the transmitted protozoans. The temperature threshold of the digestion of blood meal in case of *An. maculipennis* is about 10 °C, while the threshold temperature of the extrinsic incubation cycle of *P. vivax* is about 15 °C (*Martens et al.,* 1995). Comparing the thresholds of the activity of *An. maculipennis* imagoes and the extrinsic incubation cycle of the different *Plasmodium* species indicate that the length of the malaria season should be shorter than the potential season of adults or larvae. Based on these facts, the effect of the increasing length of the larval seasonality of *An. maculipennis* on the malaria risk cannot be clearly estimated due to the non-linear response of the vector-parasite-host system (*Patz* and *Olson*, 2006). This non-linear correlation reflects in the results of some authors, who found that the elongation of the malaria mosquito season rather increases the risk of malaria transmission in the future in the temperate areas than in the subtropical or tropical regions of the Earth (*Martens* and *Thomas* 2005; *Martens et al.,* 1995). In addition, the increasing length and frequency of above-average summer temperatures in association with heat waves due to climate change also may has unexpected positive impact on malaria transmission (*Baldari et al.,* 1998, *Krüger et al.,* 2001). Climatic change also can cause the redistribution of the dominant malaria vectors in the temperate zone of Europe, although this topic has not been studied sufficiently yet.

The number of annual mosquito generations – which primarily depends on the length of the mosquito season – substantially influences the total number of mosquitoes and the human-infected mosquito encounter probability. The exact estimation of the generation number of a mosquito should require the calculation of the temperature-based development time of each ontogeny stages, as in case of the potential annual generation number of *Aedes (Stegomyia) albopictus* Skuse, 1894 was modeled under different climatic circumstances by *Trájer et al.* (2017). The effect of the precipitation conditions on mosquito vector's abundances is controversial and highly depends on species, climate, month, and geographical location (*Landesman et al.,* 2007), but does not affect substantially the length of the season of mosquitoes in temperate areas, where appropriately small water habitats are available during the entire year – except in very severe droughts.

In fact, in Hungary it was found, that seasonal abundance profile of imagoes overlaps with the season of larvae. It can be explained by the fact that the first annual generation of larvae come from eggs laid by a small number overwintering *An. maculipennis* females in early spring (*Freeborn*, 1932), since a little

proportion of malaria mosquitoes can overwinter in caves and other shelters (*Tóth*, 2006). As it was mentioned, the correlation between the temperature and the vector-borne diseases – including the malaria risk – follows non-linear correlations, since the biological response of mosquito populations to increasing temperatures can be more than an order of magnitude larger than the observed change in temperature (*Patz* and *Olson*, 2006). *Lindsay* and *Birley* (1996) also found, that small increases in temperature at low temperatures may increase the risk of transmission radically. Global climate change will have substantial impact on the length of malaria transmission season in several areas, affecting also the temperate countries and the tropical mountains, where recently the climate is too cold for the transmission of malaria (*Martens et al.*, 1999). The length of the activity season of malaria mosquitoes is one of the important risk factors, and consequently, it also can be the symptom of the warming climate. In addition, *Bradly* (1989) showed that due to the warming trends of climate, the length of the life cycle of *Plasmodium* parasites also will be shorter increasing the risk of the transmission of the pathogens.

The analysis of the past autochthonous malaria data of Hungary provided important additive information on the influencing climatic factors of the former temperate malaria (see, e.g., *Trájer et al.,* 2016). However, the derivation of observed malaria seasons from the modeled annual activity of the plausible mosquito vectors can be problematic, since there are sparse reliable data about the exact composition, abundance, and infection rate of the former anopheline mosquito fauna. Summarizing the available data about the past vectors of (the mainly) *P. vivax* caused malaria, *Szénási et al*. (2003) found that *An. atroparvus, An. maculipennis,* and *An. messeae* were the vectors of the *Plasmodium* parasites in Hungary before the 1960's. It should be mentioned that the changes of the taxonomy of the *An. maculipennis* complex trough time and the similarity of these species to each other -causing difficulties in the identification – can cause conceptual and taxonomic confusions in the evaluation of the former literature of temperate malaria vectors. It is a notable problem, because when in the first decades of the 20th century malaria was still endemic in some parts of the temperate climate areas of Europe, the systematics of the *Anopheles maculipennis* complex was under clarification. While the name-giving *An. maculipennis* (understand as *An. maculipennis* sensu lato) already was described in 1818 by Meigen, *An. messeae* was separated from the other species of the complex only in 1926 by Falleroni. In 1935, *Hackett* and *Missiroli*, and in 1940, *Bates* published their reviews about the taxonomy of the complex. *Mihályi* and *Gulyás* (1963) clarified the occurrence and the taxonomic composition of the complex in Hungary.

It should be also added, that the malaria vector status of a mosquito depends on the specific blood meal questing preferences of malaria mosquitoes. The females of *An. maculipennis* mainly bite other mammals and rather the females of *An. atroparvus* and *An. messeae* feed on humans (*Kenyeres* and *Tóth*, 2008). These observations cannot be generalized for each of the *An. maculipennis*

populations of Central and Eastern Europe. The potential malaria vector role of *An. maculipenni*s (sensu stricto) can be proposed due to the high frequency of the species compared to the total mosquito material. *An. maculipennis* can be handled as the typical, model-value species of the *An. maculipennis* complex. Modeling the larval seasonality of this mosquito can be indicative to some other relative species of the complex in the studied region – mainly for *An. messeae* – and less in the case of *An. atroparvus*, which is a rather Mediterranean element of the complex. As it was mentioned, in the Balkan Peninsula, where some other potential malaria vectors also exist, *An. maculipennis* is a secondarily important vector of *Plasmodium* species in this area. Furthermore, the model value of *An. messeae* is less obvious in this area concerning the future malaria risk.

The modeling of larval seasonality of potential malaria vectors has further potential positive incomes for the societies and wildlife. In the past, adulticides were almost the solely agents of mosquito control causing significant damages to the ecosystems. If larvicides were applied it meant the use of contact poisons, growth regulators or surface films (as even the use of diesel oil). In the last few decades, the ecological noxiousness of these interventions become clear. The expressed hazard of the use of DDT to the ecosystems is no doubt since the release of Silent Spring (*Carson*, 1962). The new generation larvicides against anopheline and culicine mosquitoes are hormones, bacterial agents as, e.g., *Bacillus thuringiensis* Berliner, 1915 serovariety israelensis or *Lysinibacillus* (*Bacillus)* *sphaericus* Neide, 1904 (*Lacey*, 2007; *Lace*y and *Singer*, 1982; *Goldberg*, 1979), fungi, nematodes, copepods, or aquatic vertebrae (*Walker* and *Lynch*, 2007). It is plausible, that the importance of the less harmful mosquito-control agents will increase in the next decades, although the efficacy of, e.g., the bacterial agents depends on the habitat type. *Shiliu et al.* (2003) described that the bacterial biopesticides against *Anopheles* larvae were less effective in habitats with high algal content and in fast flowing streams due to the isolating effect of algal mats and the dilution effect of river streams. Along with these tools, models, which are based on the larval seasonality, can represent the progressive approach of the mitigation and adaptation strategies in response to the effect of climate change on anopheline mosquito populations.

5. Conclusions

Our model concerned a very important factor of the possible re-emergence of malaria in Central and East Europe, since the length of the mosquito larva season affects the possibility of malaria transmission by several direct and indirect ways. Of course, several other factors can act to the persistence of the autochthonous vector cycle of human malaria. It can be concluded that the changing larva season of *An. maculipennis* can be used as the indicator of climate change for malaria mosquitoes in the temperate and sub-Mediterranean areas of Central and East

Europe and the North Balkan. The additional modeling of the future seasonality of Mediterranean *Anopheles* mosquitoes should be useful in the further estimation of the possibility of the re-emergence of malaria in Europe. Our projection can be used in the planning of the chemical control of mosquito populations helping the adaptation and mitigation for the future warmer climate of Europe, since mosquito larvae are the targets of the selective biological control agents.

References

Baldari, M., Tamburro, A., Sabatinelli, G., Romi, R., Severini, C., Cuccagna, G., Fiorilli, G., Pia Allegri, M., Buriani, C., and *Toti, M.*, 1998: Malaria in Maremma, Italy. *The Lancet 351*, 1246–1247. https://doi.org/10.1016/S0140-6736(97)10312-9

Bartholy, J. and *Gelybó, R.P.G.,* 2007: Regional climate change expected in Hungary for 2071–2100. *Appl. Ecol. Environ. Res. 5,* 1–17. https://doi.org/10.15666/aeer/0501_001017

Bates, M., 1940: The nomenclature and taxonomic status of the mosquitoes of the *Anopheles maculipennis* complex. *Ann. Entomolog. Soc. Amer. 33,* 343–356. https://doi.org/10.1093/aesa/33.2.343

Bradley, D.J., 1989: Current trends in malaria in Britain. *J. Roy. Soc. Medic. 82*, 8–13.

Brown, C.R. and *Sethi, R.A.,* 2002: Mosquito abundance is correlated with cliff swallow *(Petrochelidon pyrrhonota)* colony size. *J. Medical Entomol. 39,* 115–120. https://doi.org/10.1603/0022-2585-39.1.115

Bruce-Chwatt, L.J. and *De Zulueta, J.,* 1980: The rise and fall of malaria in Europe: a historico-epidemiological study. Published for the Regional Office for Europe of the World Health Organization by Oxford University Press, Walton Street, Oxford OX2 6DP.

Caminade, C., Kovats, S., Rocklov, J., Tompkins, A.M., Morse, A.P., Colón-González, F.J., Stenlund, H., Martens, P., and *Lloyd, S.J.,* 2014: Impact of climate change on global malaria distribution. *Proc. Nat. Acad. Sci. 111*, 3286–3291. https://doi.org/10.1073/pnas.1302089111

Carson, R., 1962: Silent spring. Houghton Mifflin Company.

Chakarova, B., Kichukova, K., and *Karaslavov, G.,* 2015: A short historical overview of malaria in worldwide and in Bulgaria. The fight against malaria-the main task of sanitary epidemiological station in stara zagora in the first year of its opening, 1950. *Trakia J. Sci. 13,* 151–154. https://doi:10.15547/tjs.2015.s.02.032

Craig, M.H., Snow R.W., and *Le Sueur, D.,* 1999: A climate-based distribution model of malaria transmission in sub-Saharan Africa. *Parasitology today 15*, 105–111. https://doi.org/10.1016/S0169-4758(99)01396-4

Danis, K., Baka, A., Lenglet, A., van Bortel, W., Terzaki, I., Tseroni, M., Detsis, M., Papanikolaou, E., Balaska, A., Gewehr, S., Dougas, G., Sideroglou, T., Economopoulou, A., Vakalis, N., Tsiodras, S., Bonovas, S., and *Dougas, G.,* 2011: Autochthonous *Plasmodium vivax* malaria in Greece, 2011. *Eurosurveillance 16*, 1–5.

Facchini, F., Rastelli, E., and *Brasili, P.,* 2004: Cribra orbitalia and cribra cranii in Roman skeletal remains from the Ravenna area and Rimini (I–IV century AD). *Int. J. Osteoarchaeol., 14*, 126–136. https://doi.org/10.1002/oa.717

Filipe, A.R., 1972: Isolation in Portugal of West Nile virus from *Anopheles maculipennis* mosquitoes. *Acta virologica 16,* 361–361.

Freeborn, S.B., 1932: The seasonal life history of *Anopheles maculipennis* with reference to humidity requirements and" hibernation.". *Amer. J. Hygiene 16.* https://doi.org/10.1093/oxfordjournals.aje.a117857

Gething, P.W., Smith, D.L., Patil, A.P., Tatem, A.J., Snow, R.W., and *Hay, S.I.*, 2010. Climate Change and the Global Malaria Recession. *Nature 465*, 342–346. https://doi.org/10.1038/nature09098

Githeko, A.K., Lindsay, S.W., Confalonieri U.E. and *Patz, J.A.*, 2000: Climate change and vector-borne diseases: a regional analysis. *Bull. World. Health. Organ. 78*, 1136–1147.

Goldberg, L.J., 1979: U.S. Patent No. 4,166,112. Washington, DC: U.S. Patent and Trademark Office.

Gowland, R.L., and *Western, A.G.,* 2012: Morbidity in the marshes: Using spatial epidemiology to investigate skeletal evidence for malaria in Anglo-Saxon England (AD 410–1050). *Amer. J. Physical Anthropol. 147*, 301–311. https://doi.org/10.1002/ajpa.21648

Gratz, N.G., 2004: The mosquito-borne infections of Europe. *Europ. Mosquito Bull. 17*, 1–7.

Gubler, D.J., Reiter, P., Ebi, K.L., Yap, W., Nasci, R., and *Patz, J.A.*, 2001: Climate variability and change in the United States: potential impacts on vector-and rodent-borne diseases. *Environ. Health Perspectiv. 109*, 223. https://doi.org/10.2307/3435012

Gubler, D.J., 1998: Resurgent vector-borne diseases as a global health problem. *Emerging Infectious Diseases 4*, 442. https://doi.org/10.3201/eid0403.980326

Hackett, L.W., and *Missiroli, A.,* 1935: The varieties of *Anopheles maculipennis* and their relation to the distribution of malaria in Europe. *Rivista di Malariologia, 14*, 46–109.

Huhtamo, E., Lambert, A.J., Costantino, S., Servino, L., Krizmancic, L., Boldorini, R., Allegrini, S., Grasso, I., Korhonen, E.M., Vapalahti, O., and *Lanciotti, R.S.*, 2013: Isolation and full genomic characterization of Batai virus from mosquitoes, Italy 2009. *J. General Virology 94*, 1242–1248. https://doi.org/10.1099/vir.0.051359-0

Hume, J., 2003: Malaria in antiquity: a genetics perspective. *World archaeol. 35*, 180–192. https://doi.org/10.1080/0043824032000111362

Jacob, D., 2001: A note to the simulation of the annual and inter-annual variability of the water budget over the Baltic Sea drainage basin. *Meteorol. Atmos. Phys. 77*, 61–73. https://doi.org/10.1007/s007030170017

Jacob, D. and *Podzun*, R., 1997: Sensitivity studies with the regional climate model REMO. *Meteorol. Atmos. Phys. 63*, 119–129. https://doi.org/10.1007/BF01025368

Jetten, T.H., Martens, W.J.M., and *Takken, W.,* 1996: Model simulations to estimate malaria risk under climate change. *J. Medical Entomol. 33*, 361–371. https://doi.org/10.1093/jmedent/33.3.361

Kenyeres, Z., and *Tóth, S.,* 2008: Csípőszúnyog határozó II. (Imágók). *Pannónia Füzetek 2*, 1–96. (In Hungarian)

Kiszewski, A., Mellinger, A., Spielman, A., Malaney, P., Sachs, S.E., and *Sachs, J.*, 2004: A global index representing the stability of malaria transmission. *Amer. J. Tropical Medicine Hygiene 70*, 486–498.

Krüger, A., Rech, A., Su, X.Z., and *Tannich, E.,* 2001: Two cases of autochthonous *Plasmodium falciparum* malaria in Germany with evidence for local transmission by indigenous *Anopheles plumbeus. Tropic. Medicine Int. Health 6*, 983–985. https://doi.org/10.1046/j.1365-3156.2001.00816.x

Kuhn, K.G., Campbell-Lendrum, D.H., and *Davies, C.R.,* 2002: A continental risk map for malaria mosquito (Diptera: Culicidae) vectors in Europe. *J. Medical Entomol. 39*, 621–630. https://doi.org/10.1603/0022-2585-39.4.621

Lacey, L.A., 2007: *Bacillus thuringiensis* serovariety israelensis and *Bacillus sphaericus* for mosquito control. *J. Amer. Mosquito Control Assoc. 23*, 133–163. https://doi.org/10.2987/8756-971X(2007)23[133:BTSIAB]2.0.CO;2

Lacey, L.A. and *Singer, S.,* 1982: Larvicidal activity of new isolates of *Bacillus sphaericus* and *Bacillus thuringiensis* (H-14) against anopheline and culicine mosquitoes. *Mosquito News 42*, 537–543.

Landesman, W.J., Allan, B.F., Langerhans, R.B., Knight, T.M., and *Chase, J.M.,* 2007: Inter-annual associations between precipitation and human incidence of West Nile Virus in the United States. *Vector-Borne Zoonotic Diseas. 7*, 337–343. https://doi.org/10.1089/vbz.2006.0590

van Lieshout, M., Kovats, R.S., Livermore M.T.J., and *Martens, P.,* 2004: Climate change and malaria: analysis of the SRES climate and socio-economic scenarios. *Glob. Environ. Change 14*, 87–99. https://doi.org/10.1016/j.gloenvcha.2003.10.009

Lindsay, S.W., and *Birley, M.H.,* 1996: Climate change and malaria transmission. *Ann. Tropical Medicine Parasitol. 90*, 573–588. https://doi.org/10.1080/00034983.1996.11813087

Loevinsohn, M.E., 1994: Climatic warming and increased malaria incidence in Rwanda. *The Lancet 343*, 714–718. https://doi.org/10.1016/S0140-6736(94)91586-5

Martens, P., Kovats R S., Nijhof, S., De Vries, P., Livermore, M.T.J., Bradley, D.J., Cox J., and McMichael, A.J., 1999: Climate change and future populations at risk of malaria. *Glob. Environ. Change 9*, S89–S107. https://doi.org/10.1016/S0959-3780(99)00020-5

Martens, P. and Thomas, C., 2005: Climate change and malaria risk: complexity and scaling. *Frontis 9*, 3–14. https://doi.org/10.1007/978-1-4020-3929-4_2

Martens, W.J., Niessen, L.W., Rotmans, J., Jetten, T.H., and McMichael, A.J., 1995: Potential impact of global climate change on malaria risk. *Environ. Health Perspectives 103*, 458. https://doi.org/10.1289/ehp.95103458

Mendis, K., Sina, B.J., Marchesini, P., and Carter, R., 2001: The neglected burden of *Plasmodium vivax* malaria. *Amer. J. Tropical Medicine Hygiene 64*, 97–106. https://doi.org/10.4269/ajtmh.2001.64.97

Mihályi, F., and Gulyás, M., 1963: Magyarország csípő szúnyogjai. Akadémiai Kiadó, Budapest. (In Hungarian)

Nakicenovic, N., Alcamo, J., Davis, G., de Vries, B., Fenhann, J., Gaffin, S., and Dadi, Z., 2000: Special report on emissions scenarios: a special report of Working Group III of the Intergovernmental Panel on GCC (No. PNNL-SA-39650). Pacific Northwest National Laboratory, Richland, WA (US), Environmental Molecular Sciences Laboratory (US).

Novikov, Y.M. and Vaulin, O.V., 2014: Expansion of *Anopheles maculipennis ss* (Diptera: Culicidae) to northeastern Europe and northwestern Asia: Causes and Consequences. *Parasites vectors 7*, 389. https://doi.org/10.1186/1756-3305-7-389

Olupot-Olupot, P. and Maitland, K., 2013: "Management of severe malaria: Results from recent trials". Advances in Experimental Medicine and Biology. *Adv. Experiment. Medicine Biology 764,* 241–50. https://doi.org/10.1007/978-1-4614-4726-9_20

Oshaghi, M.A., Yaghobi-Ershadi, M.R., Shemshad, K., Pedram, M., and Amani, H., 2008: The *Anopheles superpictus* complex: introduction of a new malaria vector complex in Iran. *Bull. De La Societe De Pathologie Exotique 101*, 429–434.

Patz, J.A., and Olson, S.H., 2006: Malaria risk and temperature: influences from global climate change and local land use practices. *Proc. Nat. Acad. Sci. 103*, 5635–5636. https://doi.org/10.1073/pnas.0601493103

Patz, J.A., Martens, W.J., Focks, D.A., and Jetten, T.H., 1998: Dengue fever epidemic potential as projected by general circulation models of global climate change. *Environ. Health Perspective 106*, 147. https://doi.org/10.1289/ehp.98106147

Paz, S., and Albersheim, I., 2008: Influence of warming tendency on *Culex pipiens* population abundance and on the probability of West Nile Fever outbreaks (Israeli Case Study: 2001–2005). *EcoHealth 5*, 40–48. https://doi.org/10.1007/s10393-007-0150-0

Proft, J., Maier, W.A., and Kampen, H., 1999: Identification of six sibling species of the *Anopheles maculipennis* complex (Diptera: Culicidae) by a polymerase chain reaction assay. *Parasitology Res. 85*, 837–843. https://doi.org/10.1007/s004360050642

Reiter, P., 2001: Climate change and mosquito-borne disease. *Environ. Health Perspectives 109*, 141. https://doi.org/10.1289/ehp.01109s1141

Reusken, C., De Vries, A., Ceelen, E., Beeuwkes, J., and Scholte, E. J., 2011: A study of the circulation of West Nile virus, Sindbis virus, Batai virus and Usutu virus in mosquitoes in a potential high-risk area for arbovirus circulation in the Netherlands, "De Oostvaardersplassen." *Europ. Mosquito Bull. 29*, 66–81.

Rogers, D.J. and Randolph, S.E., 2000: The global spread of malaria in a future, warmer world. *Science 289*, 1763–1766. https://doi.org/10.1126/science.289.5485.1763

Roeckner, E., Bäuml, G., Bonaventura, L., Brokopf, R., Esch, M., Giorgetta, M., Hagemann, S., Kirchner, I., Kornblueh, L., Manzini, E., Rhodin, A., Schlese, U., Schulzweida, U., and Tompkins, A., 2003: The atmospheric general circulation model ECHAM 5. Part I: Model description. Max-Planck-Institut für Meteorologie, Hamburg, Germany.

Roeckner, E., Brokopf, R., Esch, M., Giorgetta, M., Hagemann, S., Kornblueh, L., Manzini, E., Schlese, U., and Schulzweida, U., 2004: The atmospheric general circulation model ECHAM 5. PART II:

Sensitivity of Simulated Climate to Horizontal and Vertical Resolution. Max-Planck-Institut für Meteorologie, Hamburg, Germany.

Russell, R.C., 1998: Mosquito-borne arboviruses in Australia: the current scene and implications of climate change for human health. *Int. J. Parasitology 28*, 955–969. https://doi.org/10.1016/S0020-7519(98)00053-8

Sallares, R., Bouwman, A., and *Anderung, C.*, 2004: The spread of malaria to southern Europe in antiquity: new approaches to old problems. *Medical history 48*, 311–328. https://doi.org/10.1017/S0025727300007651

Szénási, Z., Vass, A., Melles, M., Kucsera, I., Danka, J., Csohán, A., and *Krisztalovics, K.,* 2003: A malária Magyarországon: előzmények, aktuális állapot és védekezési elvek. *Orvosi Hetilap 144*, 1011–1018. (In Hungarian)

Shililu, J.I., Tewolde, G.M., Brantly, E., Githure, J.I., C.M. Mbogo, Beier, J.C., Fusco R., and *Novak, R.J.,* 2003: Efficacy of *Bacillus thuringiensis israelensis, Bacillus sphaericus* and *temephos* for managing *Anopheles larvae* in Eritrea. *J. Amer. Mosquito Control Assoc. 19*, 251–258.

Silbermayr, K., Eigner, B., Joachim, A., Duscher, G.G., Seidel, B., Allerberger, F., Indra, A., Hufnagel, P., and *Fuehrer, H.P.,* 2014: Autochthonous *Dirofilaria repens* in Austria. *Parasit Vectors 7*, 226. https://doi.org/10.1186/1756-3305-7-226

Sinka, M.E., Bangs, M.J., Manguin, S., Coetzee, M., Mbogo, C.M., Hemingway, J., Patil, A.P., Temperley, W.H., Gething, P.W. Kabaria, C.W., Okara, R.M., van Boeckel, T., Godfay, H.C.J., Harbach, R.E. and Hay, S.I., 2010: The dominant *Anopheles* vectors of human malaria in Africa, Europe and the Middle East: occurrence data, distribution maps and bionomic précis. Parasit Vectors. *3,* 117. https://doi.org/10.1186/1756-3305-3-117

Şuleşco, T., von Thien, H., Toderaş, L., Toderaş, I., Lühken, R., & Tannich, E., 2016: Circulation of *Dirofilaria repens* and *Dirofilaria immitis* in Moldova. *Parasit Vectors. 9,* 627. https://10.1186/s13071-016-1916-4

Szénási, Z., Vass, A., Melles, M., Kucsera, I., Danka, J., Csohán, A., and *Krisztalovics, K.,* 2003: Malária Magyarországon: aktuális állapot és védekezési elvek. *Orvosi hetilap 144*, 1011–1018. (In Hungarian)

Temin, P., 2006: The economy of the early Roman Empire. *J. Economic Perspectives, 20,* 133–151. https://doi.org/10.1257/089533006776526148

Tóth, S., 2006: A Bakonyvidék csípőszúnyog-faunája (Diptera: Culicidae). *Acta Biologica Debrecina, Supplementum Oecologica Hungarica 15*, 1–240. (In Hungarian)

Tóth, S., 2004: Magyarország csípőszúnyog-faunája (Diptera: Culicidae). Natura Somogyensis 6. Kaposvár 2004. (In Hungarian)

Tóth, S., and *Kenyeres, Z.,* 2012: Revised checklist and distribution maps of mosquitoes (Diptera, Culicidae) of Hungary. *Europ. Mosquito Bull. 30,* 30–65.

Trájer, A., Tánczos, B., Hammer, T., Bede-Fazekas, Á., Ranvig, K., Schoffhauzer, J., and *Padisák, J.,* 2017: The complex investigation of the colonization potential of *Aedes albopictus* (Diptera: Culicidae) in the South Pannonian Ecoregion. *Appl. Ecol. Environ.l Res. 15*, 275–298. https://doi.org/10.15666/aeer/1501_275298

Trájer, A., and *Hammer, T.,* 2016: Climate-based seasonality model of temperate malaria based on the epidemiological data of 1927–1934, Hungary. *Időjárás 120*, 331–351.

Trájer, A., Rengei, A., Farkas-Iványi, K., and *Bede-Fazekas, Á.,* 2016: Impacts of urbanisation level and distance from potential natural mosquito breeding habitats on the abundance of canine dirofilariosis. *Acta Veterinaria Hungarica 64*, 340–359. https://doi.org/10.1556/004.2016.032

Walker, K., and *Lynch, M.,* 2007: Contributions of *Anopheles* larval control to malaria suppression in tropical Africa: review of achievements and potential. *Medic. Veterinary Entomology 21*, 2–21. https://doi.org/10.1111/j.1365-2915.2007.00674.x

WHO, 2002: Scaling up insecticide-treated netting programmes in Africa: A strategic framework for coordinated national action. In: Roll Back Malaria. WHO, Geneva, Switzerland, 2002. http://www.eeaa.gov.eg/cmuic/cmuic_pdfs/generalrep/WHO_ScalingInsectNetAfrica.pdf

World Malaria Report, 2015: World Health Organization. December 2015. ISBN 978 92 4 156515 8. http://apps.who.int/iris/bitstream/handle/10665/200018/9789241565158_eng.pdf:jsessionid=733 AD1D1163752D5CD0CABC86894EDAC?sequence=1

IDŐJÁRÁS

Severe convective supercell outbreak over western Bulgaria on July 8, 2014

Lilia Bocheva*[1], **Tsvetelina Dimitrova**[2], **Rosen Penchev**[3], **Ilian Gospodinov**[1], and **Petio Simeonov**[1]

[1] *National Institute of Meteorology and Hydrology - BAS,
66, Tsarigradsko shoes Blvd., 1784 Sofia, Bulgaria*

[2] *Hail Suppression Agency,
17, Hristo Botev Blvd., 1606 Sofia, Bulgaria*

[3] *Bulgarian Air Traffic Services Authority
1, Brucssels Blvd., Sofia, Bulgaria*

*Corresponding author E-mail: Lilia.Bocheva@meteo.bg

(Manuscript received in final form April 11, 2017)

Abstract— Bulgaria is situated in a geographical area with high frequency and intensity of thunderstorms and hail events. Like in many other countries, an upward trend of weather-induced damage has been observed during the last 15 years in Bulgaria. Much of it was caused by extreme weather events such as torrential precipitation associated with severe thunderstorms or/and wind storms. The series of flash floods and extreme hail storms, which hit Bulgaria in the warm half of 2014, were in line with that trend.

On July 8, 2014, three supercell storms developed over West Bulgaria and heavily impacted urban areas in the afternoon. The extremely strong hail storms over Sofia and Montana were accompanied by strong wind gusts (about 85 km h^{-1}) and torrential rain. The giant hail stones in Sofia had diameter of up to 10 cm and irregular shape. The severe hail and rain, and very strong wind caused substantial damage to infrastructure, buildings, vehicles, and agriculture. More than 40 people were injured by hail stones or collaterally by broken windows. One man was killed by a fallen tree. In Sofia alone, the reported damage was worth more than 100 million euro according to data from insurance companies.

The paper presents the analysis of the evolution of the convective clouds based on radar data. The Doppler radar data revealed the existence of a mesocyclone, mesoanticyclone, microburst, and three-body scatter signature. The cloud top reached up to 17 km, and the maximum radar reflectivity factor was 69–71 dBZ. Analysis of the available radiosounding data, simulation with a numerical model, and the synoptic patterns are also presented.

Key-words: severe convective storms, radar analyses, split cells, hail

1. Introduction

In the middle latitudes, there are two types of long-lived thunderstorms producing damaging hail - multicells and supercells. Supercells (SC) – first defined by *Browning* (1977) – are the most violent thunderstorms producing severe weather: hail with diameter higher than 1.9 cm, flash floods, wind gusts > 25 m s^{-1}, tornadoes. *Weisman* and *Klemp* (1986) defined the main features of the supercells: 1) single, quasi-steady, rotating updraft, which may have a lifetime of several hours; 2) propagating continuously to the right (left) of the mean winds; 3) an elongation of the reflectivity pattern in the direction of the mean vertical wind shear vector; 4) a maximum gradient in the reflectivity field along the right (left) rear flank; 5) an overhang of middle-level reflectivity field over the low-level reflectivity field on the flank of the storm by several kilometers, indicating the presence of a strong updraft; 6) a hook-like echo structure at the storm's right rear (left rear) flank, and often a bounded weak echo region (BWER) appearing at middle levels above the edge of the low-level reflectivity gradient, indicating the presence of both strong updraft and strong rotation around a vertical axis in its vicinity. *Doswell* and *Burgess* (1993) defined another important feature, a deep (several kilometers) mesocyclone. They described that the hook echo and other typical features were the direct results of the mesocyclonic (mesoanticyclonic) circulations of a supercell. On the other hand, in some cases no hook or BWER were detected in the supercells. It is possible that they existed but were not detected because of the width of the radar beam at this range (*Nielsen-Gammon* and *Read*, 1995).

Many authors studied the conditions favorable for development of right-moving or left-moving supercells. Numerical simulations made by *Weisman* and *Klemp* (1982, 1984) have shown that the environmental buoyancy and vertical shear of the environmental wind were important factors in determining the storm structure. The authors reported that the relationship between the storm type, the wind shear in the 0-6 km above-ground level (AGL) layer, and the buoyancy could be represented in the form of a bulk Richardson number (BRN). *Weisman* and *Klemp* (1984) found that supercells form when the BRN is low. *Davies-Jones et al.* (1990) suggested the use of storm-relative helicity (SRH) for estimation of the likelihood for supercell development. It was calculated for the lowest 3 km layer AGL. *Rasmussen* and *Blanchard* (1998) confirmed that SRH discriminated well the supercells and ordinary cells. The helicity (SRH) and instability (CAPE) are combined in energy helicity index (EHI), which performed well in forecasting supercells (*Hart* and *Korotky*, 1991; *Rasmussen* and *Blanchard*, 1998; *Rasmussen*, 2003).

Supercells often start with cluster splitting processes to account for hodograph curvature. According to *Weisman* and *Klemp* (1986), a moderate, unidirectionally sheared environment led to the development of symmetrically splitting supercells with the anticyclonic supercell moving left of the direction of

the midlevel wind and the cyclonic supercell moving right. When, in the Northern Hemisphere, the wind shear vector rotates clockwise with height, the right-moving storm is favored, and if the wind shear vector rotates counter clockwise, the left-moving storm is favored. In the typical supercells, developing in the Northern Hemisphere, which usually are right-moving, the rotation is mesocyclonic, while in the rare left-moving supercells the rotation is mesoanticyclonic (e.g., *House et al.*, 1993; *Nielsen-Gammon* and *Read*, 1995; *Lindsey* and *Bunkers*, 2005).

Its geographical location and diverse terrain characterize Bulgaria as one of the most thundery- and hail-stormy countries in Europe. It is a fact that during the last 10–15 years, the frequency and severity of hail storms and heavy rains increased. West Bulgaria is the region with the highest frequency of thunderstorms in the country (*Bocheva et al.*, 2013), as well as other high-impact events including hailstorms, torrential precipitation, and severe convectively-induced wind storms (*Zamfirov et al.*, 2014; *Gospodinov et al.*, 2015; *Bocheva* and *Simeonov*, 2015).

In this paper, extreme convective thunderstorms which affected West Bulgaria on July 8, 2014 and caused significant damage in the towns and fields along their paths are presented. On that date, three supercells developed only for a period of six hours over Bulgaria, and two of them showed specific splitting behavior. The Doppler capability of the radars, data from which is used here, allowed their detection and analysis. Such cases of splitting hailstorms (left and right) over Bulgaria were firstly presented by *Zamfirov et al*. (2014).

2. Data and methods

The synoptic scale analysis is based on images provided by the NOAA/ESRL Physical Sciences Division, Boulder, Colorado from their website at http://www.esrl.noaa.gov/psd/ based on the National Centers for Environmental Prediction's (NCEP) reanalysis of *Kalnay et al.,* (1996), as well as on the archive of EUMETSAT satellite images, and data from meteorological network of the National Institute of Meteorology and Hydrology (NIMH). There has not been hailpad network in Bulgaria since 1990. Data from visual observations from nearby synoptic, climate, and rain-gauge stations of NIMH, as well as from rocket sites of the Hail Suppression Agency (HSA) are used in this study. The analysis of damage is based on information from the Monthly Bulletin of NIMH, reports of the national civil protection authority, local government authorities, media, and insurance companies. Upper-air sounding data from the15614 radiosonde stations of WMO (World Meteorological Organization) and the GFS (Global Forecast System) model of NOAA (National Oceanic and Atmospheric Administration) are also used.

The analysis of the splitting process and the evolution of the convective cells rely on the S-band Doppler radars of HSA, equipped with IRIS (Interactive Radar Information System) software of Vaisala, and the C-band Doppler radars of the Bulgarian Air Traffic Services Authority (BULATSA), equipped with RAINBOW software. HSA operates three radars (in Bardarski geran, Vratsa district; Goljam chardak, Plovdiv district; and Staro selo, Sliven district), and the first two of them are used in this study (see *Fig. 1*). A full 150 km scan is made every 4 minutes with 14 elevations at degrees from near 0° to 85°. The BULATSA weather radar Meteor-360 AC is located near Sofia. It is a C-band Doppler radar with a range of 250 km and continuous operation. A full 250 km scan is made every 5 minutes using 13 elevations at degrees from near 0° to 40°.

In this study, the Advanced Research-Weather Research and Forecasting (WRF-ARW) model version 3.4.1, implemented in the National Center for Atmospheric Research (NCAR) and the NCEP of the United States, is used (*NCEP*, 2014).
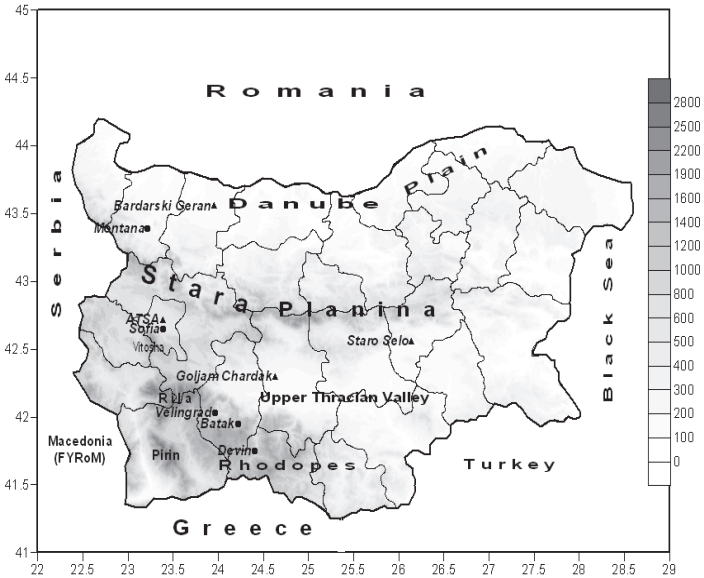
Fig. 1. Map of Bulgaria with the names of cities, towns, radar locations (black triangles), and mountains mentioned in the text. Left axis – latitude in degrees; bottom scale – longitude in degrees; color scale – altitude in m.

3. General overview of severe convective events on July 8, 2014

3.1. Analysis of the large scale environment of the storms

Bulgaria was in a saddle on July 8, 2014 between two lows to west and east and two highs to north and south (*Fig. 2*). The low to the northwest was associated with a cold air mass moving from west to east in the Western and Central Mediterranean. Thanks to the saddle circulation pattern in the middle troposphere (*Fig. 2a*), however, the flow was divergent in the region of Western Bulgaria and on the date of our interest. Near the surface, the northern high propagated to Eastern Bulgaria (*Fig. 2b*), which defined easterly or southeasterly winds in most of the country (*Fig. 4b*). At the ground level, the saddle was positioned exactly at the southeast corner of Bulgaria. Therefore, the southern high defined more southern winds in that region (*Fig. 4b*). These two features explained the convergence pattern in the lower troposphere at the time of the storms. Upper level divergence and lower level convergence were a precondition for strong convection. At the synoptic scale, the pattern resembled an occlusion which can be illustrated with the evolution of the temperature field at the 850 hPa level in *Fig. 3*. The warm-air tongue in Central and Southeastern Europe tended to close within the day which indicated occlusion-like dynamics in the region of Bulgaria.
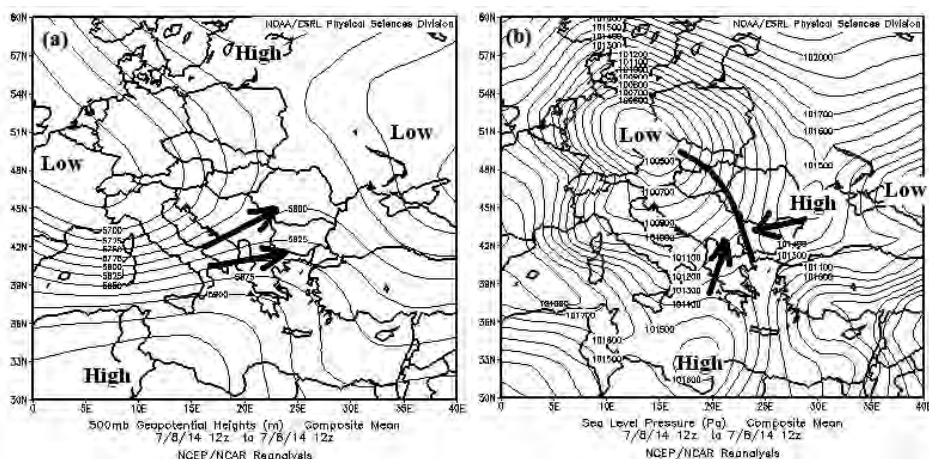
Fig. 2. Synoptic scale patterns on July 8, 2014, 12:00 UTC: (a) geopotential height (m) at 500 hPa; (b) sea level pressure (Pa). Black arrows in (a) and (b) show the direction of the air flow over Bulgaria at the corresponding level. Black curve on map (b) shows the line of instability (or pseudo-occlusion). (Source: NOAA/ESRL Physical Sciences Division, Boulder Colorado; http://www.esrl.noaa.gov/psd/)
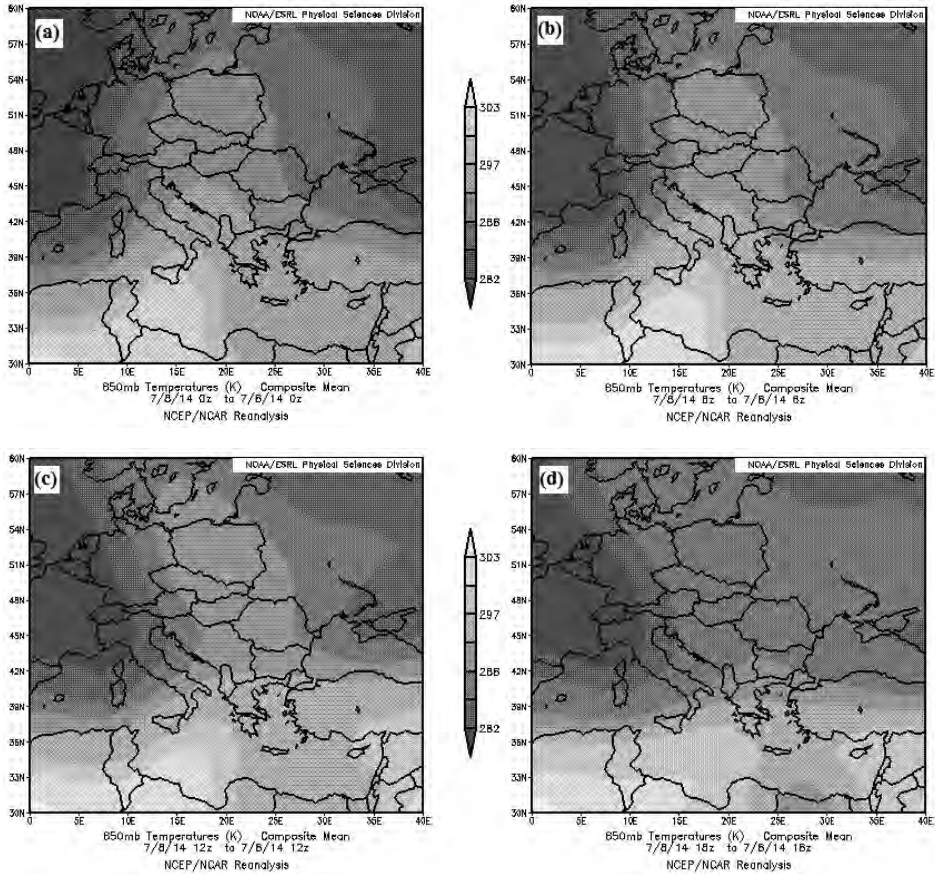
Fig. 3. Synoptic scale temperature (K) pattern at the 850 hPa level on July 8, 2014: (a) 00:00 UTC; (b) 06:00 UTC; (c) 12:00 UTC; (d) 18:00 UTC. (Source: NOAA/ESRL Physical Sciences Division, Boulder Colorado; http://www.esrl.noaa.gov/psd/)
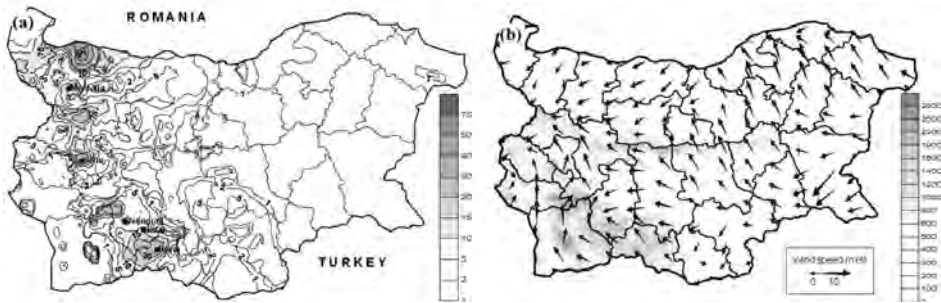

Fig. 4. (a) 24-hour accumulated precipitation amount (grey scale, mm) from 07:30 local time (LT) on July 8, 2014 to 07:30 LT on July 9, 2014. (b) Wind speed (length of the arrow, m s^{-1}) and direction on July 8, 2014, 12:00 UTC; grey scale - terrain altitude.

Fig. 4a shows the precipitation pattern for the date. It illustrates how the storm systems did not manage to propagate much further than the central part of Bulgaria, where they tended to decay which can be seen in *Fig. 5d*. The most significant precipitation spots were in the western part of the country and were associated with the strongest phase of the storm systems on July 8. There were two distinctively separated precipitation patterns: one to the northwest of the country and another one to the south, in the West Rhodopes Mountain. This reflected the divergent leading upper flow. *Fig. 4b* represents the analysis of the 10 m wind at 12:00 UTC on July 8, right before the hail storm hit Sofia. The overall easterly or southeasterly winds in North and East Bulgaria are well visible. They are the result of the influence of the northeastern high-pressure center. In the southwestern corner of the country, one can notice the more southerly oriented winds. From one side, they were defined by the local orography and followed the principal axes of the river valleys in the region. But, from the other side, they experienced the influence of the southwestern high (*Fig. 2b*), which pulled the general wind direction from south.

3.2. Evolution of the storms

Fig. 5 illustrates the evolution of the analyzed storms from satellite perspective. The thin black circles show the position of the analyzed hail storm system, which has hit Sofia, at its origin (a), growth (b), split (c), and decay (d). The thick black circle in (d) highlights the southern storm, which has hit Velingrad and Devin in the Rhodopes. Black arrow points to the position of the hailstorm over Sofia. The Sofia cloud first appeared near the western Bulgarian border at around 11:00 UTC (*Fig. 5a*). Then it strengthened by going eastwards (*Fig. 5b*) and split (*Fig. 5c*). The northern, left-moving storm went beyond Stara Planina (a mountain ridge) and hit the region of Montana. The southern, right-moving storm is the one which has later produced the severe hail fall in Sofia.

The northern and the southern storms dissipated later in the day (*Fig. 5d*), but others appeared behind them along the same storm line, stretching from the Rhodopes to the northwestern corner of Bulgaria, because the large scale conditions did not evolve significantly. In this later generation of convective storms, there was another significant one developing in South Bulgaria. It appeared first over Rila Mountain around and after 15:00 UTC (not shown) and moved in southeasterly direction to the West Rhodopes, which can be seen in *Fig. 5d*, where it hit Velingrad first and Devin later.
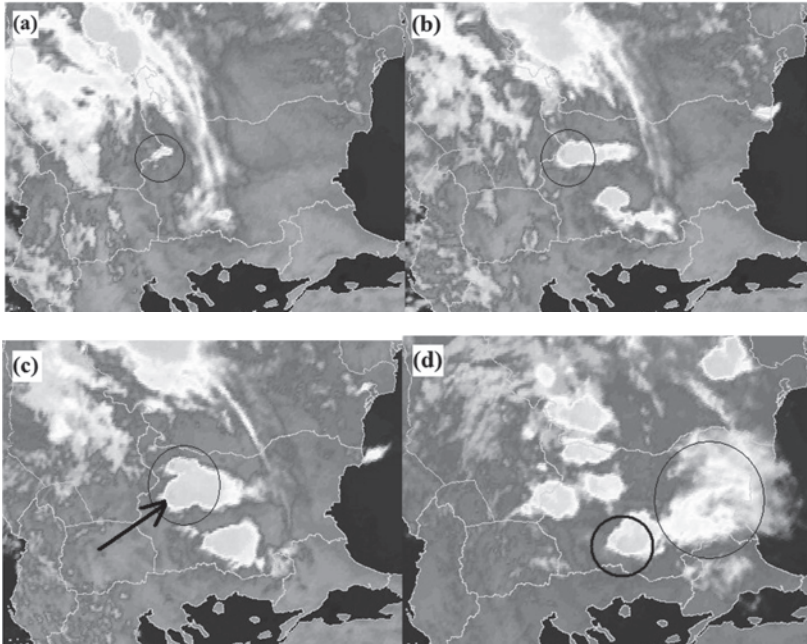
Fig. 5. Infrared satellite images on July 8, 2014: (a) 11:00 UTC; (b) 12:30 UTC; (c) 13:30 UTC; (d) 17:00 UTC. (Source: NIMH archive of EUMETSAT satellite images.) Circles and arrow point to the location of the analyzed storms.

3.3. *Aerological analysis of sounding data*

The most vigorous one of the three analyzed storms developed over Sofia, the capital city. The NIMH operates a WMO aerological station (number 15614) in Sofia, where the regular sounding takes place at 12:00 UTC. Therefore data from that sounding on July 8 was used to analyze the environment of the storm over Sofia (*Fig. 6a*). For the other storms, however (over Montana – *Fig. 6b* and over Velingrad – *Fig. 6c*), pseudo-sounding data at 15:00 UTC, derived from the operational GFS model, was used. Those storms were relatively far from Sofia (*Fig. 1*), and their strongest part was later than the time of the operational sounding at station 15614. The pseudo-sounding data is combined with real measured surface data from other synoptic stations nearby. The data were processed by the RAwinsonde OBservation (RAOB) sounding software. This approach had already been used in *Simeonov et al.* (2013). The height of the 0 ºC isotherm (freezing level), was found to be 3231 m for Velingrad, 3479 m for Sofia, and 3728 m for Montana. Stability and wind shear indices were calculated and analyzed (*Table 1*). The lifted index (LI) for example points to strong instability. Its values are: -7.1 ºC for Sofia; –6.2 ºC for Montana; and –5.6 ºC for Velingrad. The values of CAPE are about 2648 J kg^{-1} for Sofia, 1686 J kg^{-1} for Montana, and 1564 J kg^{-1} for

184

Velingrad. These values, determined from surface parcels, suggested that the environment would support thunderstorms. The Total Totals (TT) index is higher than 50 and indicates a potential development of severe storms.

Fig. 6. Stuve diagramme, hodograph, and basic environmental characteristics on July 8, 2014 (processed by RAOB). Buoyant energy is shaded and the wind profile is illustrated at right in m s^{-1}: (a) Sofia sounding – 12:00 UTC, (b) Montana sounding – 15:00 UTC, (c) Velingrad sounding – 15:00 UTC.

Table 1. Stability and wind shear indices for the three suppercells on July 8, 2014

Indices	SC Sofia	SC Montana	SC Velingrad
CAPE (J kg^{-1})	2648	1686	1564
LI (°C)	–7.1	–4.2	–5.6
TT (°C)	55.4	52.0	51.0
KI (°C)	34.9	37.0	34.0
BRN	57	30	18
SWEAT	349.8	231	233
SRH_{0-3} (m^2 s^{-2})	132	118	143
EHI_{0-3}	1.9	1.0	1.0
VV (m s^{-1})	73	58	56

The shapes (*Fig. 6*) of the wind hodograph in low levels (0–6 km) suggest a wind profile that would support rotating convection. The hodographs, corresponding to the environment of the left-moving storm over Montana and the right-moving storm over Velingrad, have typical supercell shapes (*Weisman* and *Klemp*, 1986) with tendency to be more linear above 2 km AGL. The curvature of the hodograph of the left-moving SC Montana turns clockwise (*Fig. 6b*). Similar cases of left-moving supercells, despite the shear vectors exhibiting clockwise curvature, were obtained and discussed by other authors (*Grasso* and *Hilgendorf*, 2001; *Bunkers,* 2002). The hodograph for the SC Sofia exhibits well pronounced clockwise curvature to 180 degrees in the lower 0–6 km (*Fig. 6a*). According to *Weisman* and *Klemp* (1986), significant shear magnitude and depth of the shear profile are sufficient to produce strong positive vertical pressure gradient force on the right flank of the initial updraft. It is fact, that after the splitting of the initial cell, the right flank evolved into a quasi-steady supercell (Sofia), which moved to the right of the mean winds, whereas the left flank evolved into a weak and short-lived cell. Wind shear indices BRN, SRH_{0-3}, and EHI_{0-3} for layer 0–3 km AGL were calculated for the diagnosis of the supercell's development (*Table 1*). The BRN indices were 57 m^2 s^{-2} (SC Sofia), 30 m^2 s^{-2} (SC Montana), and 18 m^2 s^{-2} (SC Velingrad). The values of SRH_{0-3} for the environment of the three examined supercells were higher than the threshold of 100 m^2 s^{-2} for supercell development (see *Table 1*). EHI_{0-3} has values between 0.6 (SC Montana) and 1.5 (SC Sofia). All indices, therefore, show an environment favoring supercell development. The calculated maximum vertical velocities are high (more than 55 $m\,s^{-1}$). This indicates significant development of convective clouds topping above the equilibrium level (EL), with an attendant risk for heavy rain and hail.

4. Analysis of Doppler radar data of severe convective storms

4.1. Sofia supercell

In the early afternoon, at 10:35 UTC, an isolated cell was first detected 70 km northwest of Sofia outside the territory of Bulgaria. The maximum radar reflectivity factor (Zmax) of the cell was 35 dBZ between 6 and 10 km (–12 °C and –40 °C, see – *Fig. 7a*). The cell developed rapidly and Zmax reached 50–55 dBZ at 10:50 UTC. During the period between 11:30 UTC and 12:10 UTC, new cells developed about 10 kilometers away from the first one, and a cluster formed. The new cells quickly merged in single storm (*Figs. 7c, d*), and the maximum radar reflectivity exceeded 60 dBZ. At 13:00 UTC, the storm split (*Fig. 7e*), producing a cyclonically rotating supercell (SC Sofia) moving to the right of the mean midlevel winds. It passed over Sofia and dissipated at 15:35 UTC out of the city. The second cell moved to the left of the mean midlevel winds. It had no severe development and dissipated 20 minutes after splitting.
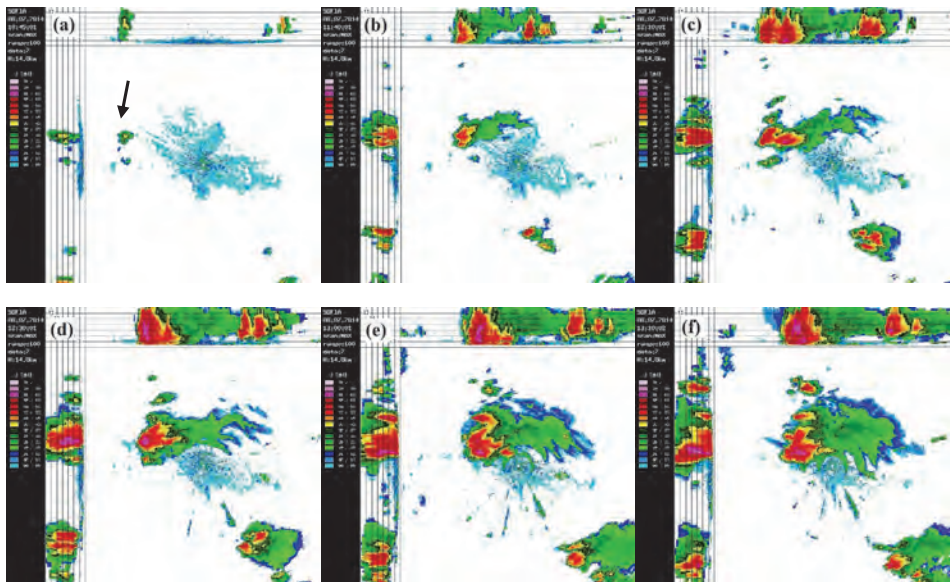
Fig. 7. Formation and development of Sofia supercell based on maximum radar reflectivity obtained by C band radar, located at Sofia airport: (a) at 10:45 UTC, the cell is showed by an arrow ; (b) at 11:40 UTC; (c) at 12:10 UTC; (d) at 12:30 UTC; (e) at 13:00 UTC; (f) at 13:10 UTC.

The vertical wind pattern was analyzed by using the VVP (velocity volume processing) product in time between 12:11 UTC and 14:31 UTC. The analysis showed a low-level backing of the wind, implying a clockwise turning of the hodograph and confirmed the possibility of right-moving thunderstorms (*Fig. 8a*) (*Klemp* and *Wilhelmson,* 1978; *Nielsen-Gamon* and *Read*, 1995). Detailed analysis of the hodograph plot by RAOB (Fig.8b) showed that before 13:00 UTC, when the storm had split, the hodograph had well pronounced clockwise curvature to 180 degrees in the lower 2.2 km with growth of the magnitude and the depth of the shear profile. During the period of severe hail (13:31 UTC – 14:11 UTC), the hodograph changed its form to approximately straight line.

Immediately after splitting, the area of radar reflectivity factor of 60 dBz reached a height of over the –20 °C isotherm, held for next 90 minutes (*Figs. 9* and *10a*), and it was wide more than 30 km^2 (not shown). According to *Blair et al*. (2011), this is a criterion for the existence of giant hailstones. According to meteorological stations reports, the observed size of hailstones on ground in Sofia was more than 5 cm.

The storm severity and the presence of large hail stones were confirmed by VIL (vertical integrated liquid) and VILD (VIL density) value. VIL values exceeded 65 mm and lasted for 1 hour and 40 minutes (13:04 UTC – 14:44 UTC). The high values of VIL indicate that the storm had high reflectivity distributed over a large depth of the atmosphere, and that it is a good indicator for the potentiality of severe weather (*Nielsen-Gamon* and *Read*, 1995; *Edwards* and *Thompson*, 1998). In the same time, VILD (*Amburn* and *Wolf*, 1997) had values higher than 3 g m^{-3} which is the severe hail (> 2 cm) threshold obtained for Bulgaria (*Dimitrova et al.*, 2013).

The strongest development of SC Sofia was between 13:30 UTC and 14:05 UTC, when the maximum reflectivity was 70 dBZ and the echo top (15 dBZ) was between 17 km and 18 km. The southeast end of SC Sofia became comma-head shaped at 13:50 UTC (*Fig. 10b*).

(a)

SOFIA
08.07.2014
12:11:01
scan:VVP
data:V

SOFIA
08.07.2014
12:51:01
scan:VVP
data:V

SOFIA
08.07.2014
13:21:01
scan:VVP
data:V

SOFIA
08.07.2014
13:31:03
scan:VVP
data:V

SOFIA
08.07.2014
13:41:02
scan:VVP
data:V

SOFIA
08.07.2014
13:51:02
scan:VVP
data:V

SOFIA
08.07.2014
14:11:03
scan:VVP
data:V

SOFIA
08.07.2014
14:31:03
scan:VVP
data:V

(b)

12:11 UTC   12:51 UTC   13:21 UTC   13:31 UTC

13:41 UTC   13:51 UTC   14:11 UTC   14:31 UTC

Fig. 8. Wind profiles of the supercell propagation during the period 12:11 UTC - 14:31 UTC, obtained by C band radar, located at Sofia airport: a) "raw" wind data b) a plot of a series of hodographs by RAOB.

189
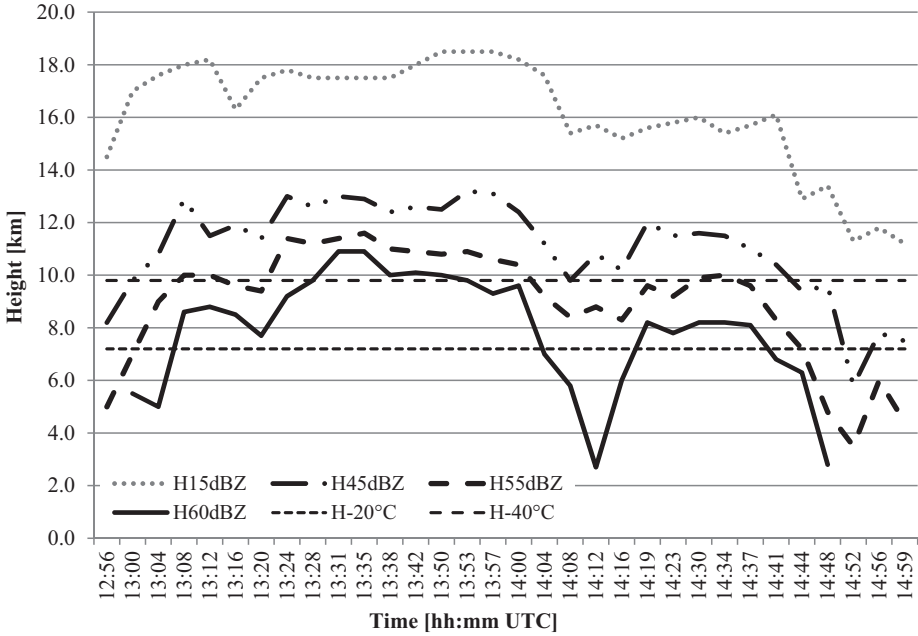
Fig. 9. Time series of radar reflectivity factors during the lifetime of SC Sofia. H15 − height of area of 15 dBZ radar reflectivity; H45 − height of area of 45 dBZ radar reflectivity; H55 − height of area of 55 dBZ radar reflectivity; H60 − height of area of 60 dBZ radar reflectivity; H-20 °C – height of -20 °C isotherm; H-40 °C – height of -40 °C isotherm. The radar data are obtained by S band radar.
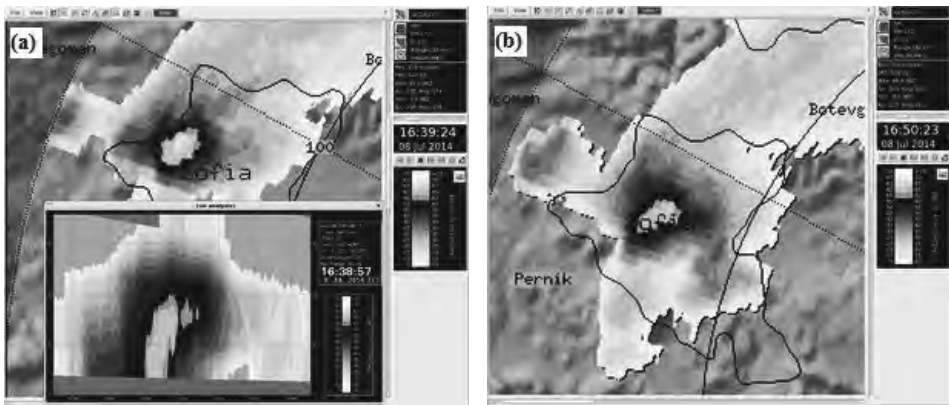
Fig. 10. A PPI (at 1.7° elevation) reflectivity image of SC Sofia during its maximum development, obtained by S band radar a) at 13:39 UTC (16:39 LT); b) at 13:50 UTC (16:50 LT).

The extreme hail event, accompanied with strong wind gust, heavy rain, and high lightning frequency was registered between 13:30 UTC and 14:00 UTC. The giant hailstones had diameter up to 10 cm and irregular shape. TBSS (three body scattering signature) was observed (*Fig. 7f*) during the period between 13:00 UTC and 13:30 UTC. Such cases have been analyzed in detail by *Lemon* (1998), who suggested that it could be expected that hail stones equal to or greater than 2.5 cm in diameter would reach the surface within the next 10–30 min. In confirmation of these conclusions, in our case, the TBSS appeared 30 minutes before the registration of severe hail on the ground.

Thunderstorm mesocyclone is manifested on Doppler velocity scans. The rotation was evident between 4 and 6.5 km height (*Fig. 11a*). In the southeastern part of the rotation core, radial velocities of -13 m s^{-1} (towards the radar) and on the opposite side, radial velocities of $+13$ m s^{-1} (outwards) were observed. Higher values could have been expected, but these are the maximum that the radar can detect. The registered values of the horizontal wind shear (combination of the so-called radial shear and the azimuthal shear) were above 14 m s^{-1} km^{-1}. In accordance with *Holleman* (2008), these values exceeded the threshold of 8 m s^{-1} km^{-1}, determined by the author, which suggested the existence of a microburst (indicated by an arrow in *Fig. 11b*). Many uprooted and/or broken trees in Sofia bring evidence of strong surface winds by the microburst.
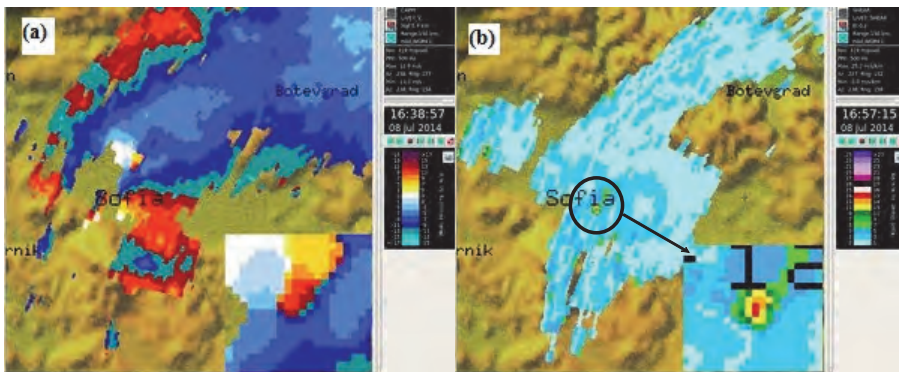
Fig. 11. (a) CAPPI 5.9 km of Doppler velocity of SC Sofia at 13:38 UTC (16:38 LT). A zoom image of mesocyclon rotation is given in the right corner of the images. (b) A horizontal wind shear at 0.2° elevation of SC Sofia at 13:57 UTC (16:57 LT).

4.2. Montana supercell

Left of SC Sofia, a new cell formed and developed as supercell (noted as SC Montana) moving to the left of the mean midlevel winds and characterized by anticyclonic rotation. Its first registration was at 13:00 UTC and, like for SC

Sofia, the first radar echo with maximum radar reflectivity 25 dBZ was between the heights of 5 km and 10 km, where the temperature reached –35 °C (*Fig. 12a*). By analogy with SC Sofia, the convective cell had strong development. At 13:23 UTC, the height of the area with 45 dBZ was above 10 km, and the maximum radar reflectivity was 55 dBZ. In *Fig. 12b* it can be seen, that within the radar range of 150 km, there were only two supercells - SC Sofia and SC Montana. SC Sofia moved southeast and SC Montana moved northeast. At 14:00 UTC, SC Montana split and its left-oriented part acquired supercell structure (*Fig. 13*). The right-moving cell had short life time and reached maximum reflectivity of 50 dBZ only. The left-moving supercell had lifetime of more than 4 hours.
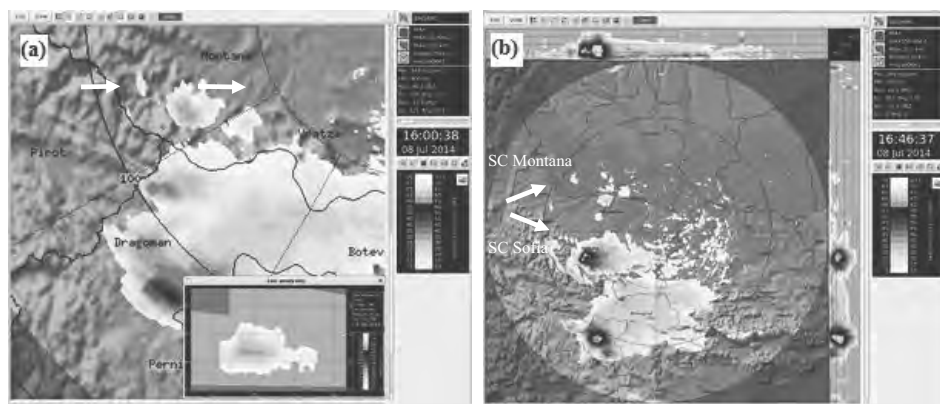
Fig. 12. (a) SC Montana thunderstorm formation at 13:00 UTC (16:00 LT) – showed by an arrow. A radar vertical cross section of the cell is given in the right corner of the image. (b) Maximum radar reflectivity image of the coexistence of SC Sofia and SC Montana at 13:46 UTC (16:46 LT).
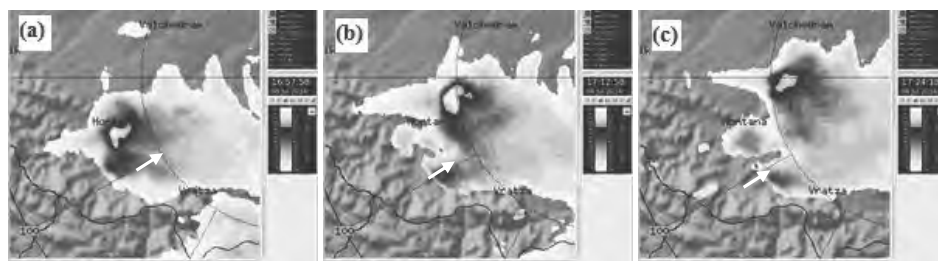
Fig. 13. Maximum radar reflectivity during the Montana storm spliiting: (a) at 14:01 UTC (17:01 LT) ; (b) at 14:12 UTC (17:12 LT); (c) at 14:24 UTC (17:24 LT). The second weaker cell is showed by an arrow.

The left-moving supercell was characterized by long lifetime of severe stage. At 13:38 UTC, radar reflectivity above 60 dBZ was registered and was kept above that level for the next 90 minutes. In the 10 minutes following the splitting at 14:00 UTC, the maximum radar reflectivity factor increased sharply and reached a maximum value of 74.5 dBZ at 14:12 UTC. The height of the area of 55 dBZ was above 12 km and that of the area of 60 dBZ – above 10 km. The area of radar reflectivity factor of 60 dBZ reached 30 km^2 (not shown) at height above –20 °C and lasted more than 30 minutes (*Fig. 14*). VIL increased rapidly between 13:00 UTC and 13:28 UTC, and its values were higher than 65 mm for about 1 hour. Between 13:44 UTC and 14:52 UTC, VILD was higher than 3.0 g m^{-3}. In the same time, the registered hailstones on the ground had size larger than 2.5 cm.
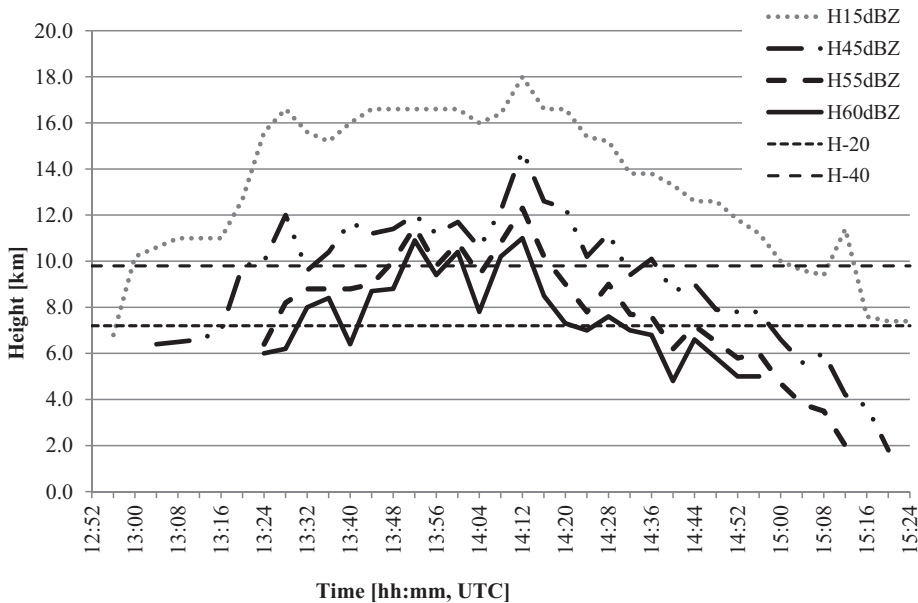

Fig. 14. Time series of the radar reflectivity factor during the lifetime of SC Montana. H15 − height of area of 15 dBZ radar reflectivity; H45 − height of area of 45 dBZ radar reflectivity; H55 − height of area of 55 dBZ radar reflectivity; H60 − height of area of 60 dBZ radar reflectivity; H-20 °C – height of -20 °C isotherm; H-40 °C – height of -40 °C isotherm. The radar data are obtained by S-band radar.

The TBSS appeared at 13:31 UTC, 20 minutes before hail registration on the ground and 44 minutes before severe hail registration on the ground. The flare was observed for 80 minutes, and its length reached more than 40 km

(*Fig. 15a*). TBSS is associated with Non-Rayleigh scattering from large, wet hailstones, whose diameter to wavelength ratio is greater than 1/16th of the radar wavelength (*Lemon*, 1998; *Zrnić*, 1987). On the other hand, the large area of 60 dBZ and high horizontal gradients (12 dBZ per 1 km) at the northern end of the storm led to a sidelobe spike emergence at 13:38 UTC, 20 minutes before the severe hailfall on the ground (Fig. 15a). According to *Manros et al.*, 2010, sidelobe contamination in radar data occurs when there are strong horizontal (or vertical) gradients of reflectivity, on the order of 40 dB per 1 degree. This type of gradient is usually connected with strong thunderstorms capable of producing hail. The presence of the artefacts (TBSS and sidelobe spike), each having different origin, confirms the theory that they can be linked to the existence of large hailstones. Between 13:52 UTC and 14:54 UTC, during their registration, the hail stones size reached 6 cm (information from rocket sites of HSA).
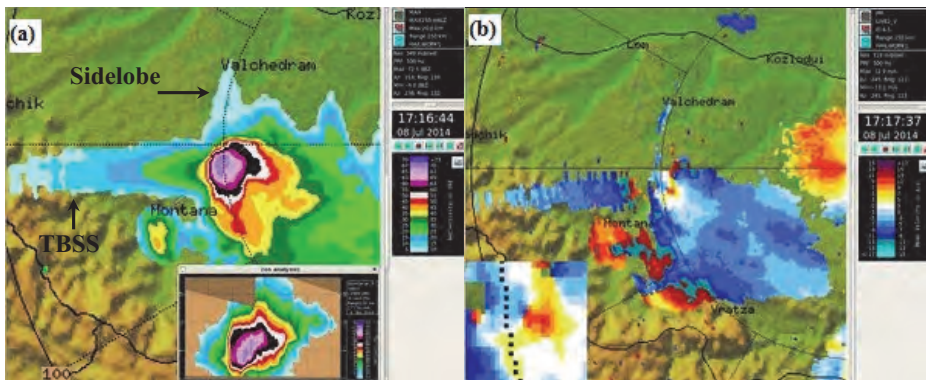
Fig. 15. (a) Maximum radar reflectivity of SC Montana with TBSS and sidelobe observation at 14:16 UTC (17:16 LT). A radar vertical cross section of the cell is given in the right corner of the images. (b) PPI at 4.5° elevation of Doppler velocity of SC Montana at 14:17 UTC (17:17 LT). A zoom image of mesoanticyclon rotation is given in the right corner of the image. Radar information is given by S-band radar.

During the period of maximum development of SC Montana, the analysis of Doppler velocity showed anticyclonic rotation. It was observed for 10 minutes. Evidence of rotation can be found at the levels between 5 and 7 km (*Fig. 15b*). The southern side of the hail core (viewed by the radar) had Doppler velocities away from the radar, while the northern side of the hail core had Doppler velocities toward the radar. The SC Montana is the first documented case of anticyclonically rotating core of supercell developed over Bulgaria. The

vigorous development of the cell accompanied by high updraft velocity is confirmed by the fact, that the speeds in the center of the core are close or equal to zero (*Fig. 15b*). This conclusion is based on the relationship between the Doppler radial velocities in the TBSS area, the storm core, the vertical velocities associated with hydrometeors (*Zrnić,* 1987; *Carbunaru et al.*, 2010), and the presence of high positive Doppler velocity in the beginning of TBSS.

4.3. Velingrad supercell

Another squall line formed at 15:10 UTC to the southeast of the dissipated SC Sofia (*Figs. 16a, b*). At 15:50 UTC, one of the cells of that squall line developed rapidly and evolved into a supercell (SC Velingrad). Its lifetime was more than two hours (*Fig. 16c*).

The cell had smaller area than the other two supercells, but kept high values of other radar characteristics and had recognizable features of supercell. VIL increased rapidly from values of 38 mm to 62.5 mm (not shown) at 15:56 UTC and kept values higher than 60 g m^{-3} during the period of 16:00–17:30 UTC. In the same time, the maximum radar reflectivity was higher than 60 dBZ with height above –20 °C. The maximum registered value of radar reflectivity was 70 dBZ. The values of VILD were higher than 3.0 g m^{-3} pointing to the existence of severe hail (*Dimitrova et al.*, 2013). The supercell had cyclonic rotation (*Fig. 17a*). A mesocyclone was observed at the levels between 5.5 km and 6.5 km. TBSS was registered and lasted 35 minutes (*Fig. 17b*). Due to the passage of the cell over a mountainous area, there was no information of the size of hailstones based on ground observation. Bearing in mind the high values of the radar characteristics, it could have been expected to have hailstones larger than 2 cm.

Fig. 16. Formation and development of Velingrad thunderstorm (a) at 10:45 UTC, the storm is showed by an arrow ; a) at 15:03 UTC (18:03 LT); (b) at 15:36 UTC (18:36 LT); (c) at 16:12 UTC (19:12 LT) when supercell was formed (showed by an arrow). Radar information is obtained by S-band radar.
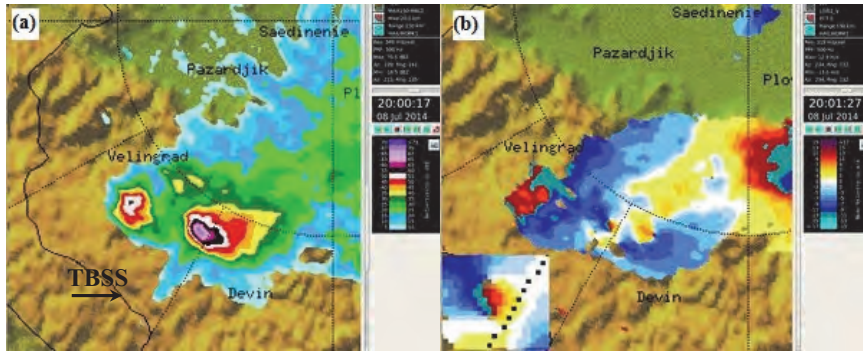
*Fig. 17*. (a) Maximun radar reflectivity of SC Velingrad with TBSS observation at 17:00 UTC (20:00 LT). (b) PPI at 7.0° elevation of Doppler velocity of SC Velingrad at 17:01 UTC (20:01 LT). A zoom image of the mesocyclon rotation is given in the left corner of the image. Radar information is given by S-band radar.

5. *Model simulation*

This section deals with numerical simulations of the supercells. 24-hour simulations were carried out with initial conditions at 00:00 UTC on July 8, 2014. In the first six hours, the model fields were spin-upped. The time frame of interest was between 13:00 and 16:00 UTC.

The initial and boundary conditions for air temperature, wind speed, humidity, pressure, and total cloud cover were taken from the operational GFS distributed by the NCEP with a spatial resolution of 0.5°. The model configuration uses the non-hydrostatic approximation. The model domain is resolved by a grid in Lambert conformal projection with three nests, correspondingly with a spatial resolution of 15:5:1.8 km. The two-way nesting technique is used for better boundary conditions. The domain covers Bulgaria and adjacent regions, and the third domain with the finest resolution is selected in a way to cover the mountain chains in the western part of the country, and the center is located in Sofia, where atmosphere sounding is performed every day at 12:00 UTC. The vertical coordinate system is sigma terrain-following, with 65 levels. Several numerical experiments are performed to configure and tune the model parameters in order to obtain adequate mode results. The most important parameters are related to the parameterization of the sub-grid physical processes (*Penchev.* and *Peneva,* 2013). The following parameterization schemes are used in the model:

- for microphysical processes in the clouds: WRF Double-Moment 6 class scheme (*Lim* and *Hong,* 2010),
- longwave radiation processes: RRTM (Rapid Radiative Transfer Model) (*Mlawer et al.,* 1997),
- shortwave radiation processes: Dudhia scheme (*Dudhia, J.,* 1989),

196

- air-surface exchange processes: Noah Land-Surface Model,
- planetary boundary layer parameterization: Yonsei University scheme, and
- convective processes parameterization: Kain-Fritsch scheme (*Kain, 2004*). This scheme is used only in the first and second domains, and in the third domain, where resolution is 1.8 km, the convection is not parameterized.

The aerological diagram (not shown), calculated by the WRF model, shows the presence of wind shear in the layer at altitude of about 2 km, a not very well defined layer of dry air, and a layer, in which the presence of significant CAPE can be expected. The analysis of some convective parameters such as CAPE and CIN (convective inhibition) (*Fig. 18*) indicates, that in the afternoon of July 8, in the western part of Bulgaria, the weather conditions were unstable with CAPE more than 1300 J kg^{-1} and CIN close to 0 m^2 s^{-2}. The combination of both parameters shows that the best conditions for convection were in the period between 11:00 UTC and 14:00 UTC.
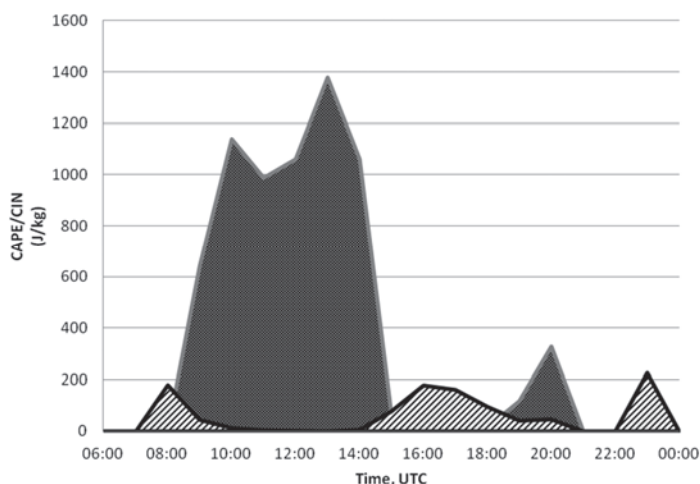

Fig. 18. CAPE and CIN time series based NWP model calculations for Sofia.

Evidences for the presence of deep convection was the development of three convective cells – two of them north of Sofia and one over Rhodope Mountains, as shown on the image of maximum 10 cm radar reflectivity field (*Fig. 19a*).
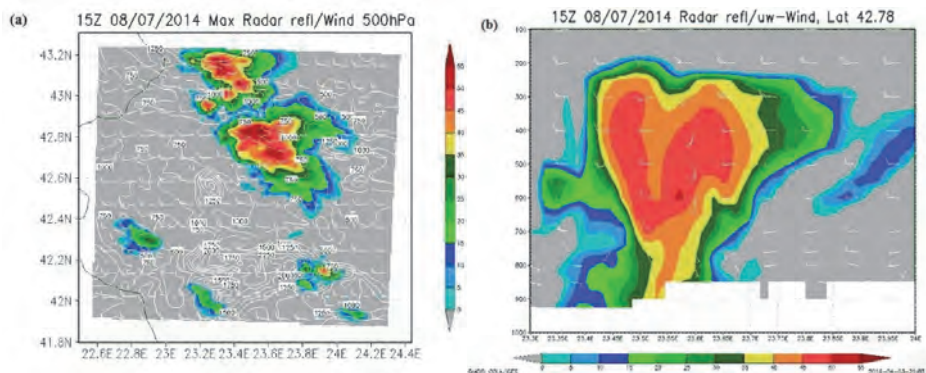
Fig. 19. a) Modeled radar reflection in dBz, for wavelength of 10 cm, combined with the field of wind of 500hPa; b) elevation of the reflection on AB axis, combined with the field of wind in the vertical plane of the section (wind barbs show the direction of movement vertically and horizontally).

In the simulation, SC Sofia is shifted northeastwardly and the impact of hydrometeors in the simulated radar image was lower than the observed one. The model convection occurred with an about two-hour delay. Well-developed cells appear at 15:00 UTC and lasted until 19:00 UTC, when they were still about 50 dBz. As the observed phenomena were commensurate with the resolution of the model, the latter failed to completely simulate the evolution of the formation of the first supercell. However, the numerical model successfully generated the convective phenomena, but with less intensity. For example, the amount of rain fallen for one hour in the period of maximum development of supercell did not exceed 8 mm. Also, the measured vertical speeds in the areas with maximum impact reached 17 m s^{-1}. The motion of SC Sofia and the shape of its radar reflectivity are shown in *Fig. 19b*. This corresponds very well to the convective events observed in the late afternoon on this day near Sofia.

6. *Analysis of damage data*

The giant hail stones in Sofia had diameter up to 10 cm size and irregular shape. The hail path was about 30 km long and more than 10 km wide and passed trough the central parts of the city. According to the meteorological station data, the duration of continuous hail was about 20 min and the measured precipitation amount during the process was above 35% of the monthly normal. The severe hail with rain and very strong wind (wind gust up to 23 m s^{-1}) caused substantial damage to infrastructure, buildings, and vehicles. More than 40 people were injured by hail stones or colaterally broken windows in Sofia. One man was

killed by a falling tree. In Sofia alone, the reported damage was worth more than 123 million euro according to data from insurance companies (*Viktor et al.*, 2015).

The hail stones in the region of Montana were sized from walnut to egg, and the duration of the hailfall was about 13 min. The hail storm stroked 4 municipalities in the district of Montana. The severe hail with torrential rain and strong wind (wind gust 17–20 m s^{-1}) caused damage to infrastructure, roofs, vehicles, and agriculture. More than 45% of corn crops, vegetables, and fruits were destroyed in fields and villages in the region. About 10 villages were left without electric supply for more than 12 hours after the storm. Many houses were flooded.

There is less available data for damage related to the passage of the third storm over the Western Rhodopes. This is mainly due to the sparse network of weather stations and the small number of settlements in the area. The peak of the storm was over the mountainous woodland. Nevertheless, the hailstorm was registered by three meteorological stations (rain gauges) in the region. There were also a few damage reports from Devin, where heavy rain (30 mm per=2 hours) caused local floods.

7. Conclusions

This study shows the splitting of convective cells over West Bulgaria on July 8, 2014, which was detected on S-band and C-band Doppler radar and satellite images. Three supercell storms formed and developed over Bulgaria on that day. One of them (over Montana) exhibited anticyclonic rotation.

Thermodynamic analysis showed high instability of the atmosphere on July 8, 2014. CAPE reached extreme instability values (CAPE > 2500 J kg^{-1}) pointing to strong updraft – a precondition for severe hail formation. Highly negative LI (between –5.6 ºC and –7.1 ºC) conformed to the same conclusion. Wind shear indices were in line with the existence and evolution of the supercells. The BRN index was 57 m^2 s^{-2} (SC Sofia), 30 m^2 s^{-2} (SC Montana), and 18 m^2 s^{-2} (SC Velingrad). The values of SRH$_{0-3}$ concerning the environments of the three examined supercells were higher than the threshold of 100 m^2 s^{-2} for the supercell development. The shapes of wind hodographs at low levels of 0–6 km matched a wind profile that would support rotating convection.

The radar signatures illustrated, that during the hailfall, VIL was greater than 65 mm and was linked to reflectivity larger than 65 dBZ near the surface. The area of radar reflectivity factor of 60 dBz reached a height higher than the –20 °C isotherm and lasted for 90 minutes, which confirms the criterion of *Blair et al.* (2011) for the existence of giant hailstones. Hailstones with sizes up to 10 cm of diameter were registered. VILD had values higher than 3 g m^{-3}, which is the threshold for severe hail obtained for Bulgaria (*Dimitrova et al.,* 2013).

They lasted for more than 1 hour. TBSS was observed about 30 minutes before severe hail fell on ground in all of the 3 analyzed supercell cases. The values of the horizontal wind shear (combination of the so-called radial shear and the azimuthal shear) for the Sofia supercell were above 14 m s^{-1} km^{-1}. These values exceeded the threshold of 8 m s^{-1} km^{-1} (*Holleman*, 2008), for the existence of microburst.

The hailstorm of July 8, 2014 in Sofia has been the strongest in terms of both duration and strength for the last 75 years – according to national weather-data archives. The damage to infrastructure, buildings, and vehicles was extreme. One man was killed by a falling tree. The insurance claims, after the Sofia hailstorm, were worth more than 120 million Euros.

The WRF-ARW numerical model successfully simulated the convective processes, but, because of the lower intensity of the dynamic processes in the model, the convective flows formed slowly, and this resulted in a delay of the formation of the simulated convection cells, which also had lower intensity compared to the real ones. Due to the small size of the initial convective cells, the model failed to simulate well the initial stages of their evolution.

References

Amburn, S.A. and *Wolf, P.L.,* 1997: VIL density as a hail indicator. *Weather Forecast. 12*, 473–478. https://doi.org/10.1175/1520-0434(1997)012<0473:VDAAHI>2.0.CO;2

Blair, S., Deroche, D., Boustead, J., Leighton, J., Barjenbruch, B., and *Gargan, W*., 2011: A Radar-Based Assessment of the Detectability of Giant Hail, *E-J. Severe Storms Meteorol. 6*, 7, 1–30.

Bocheva, L., Simeonov, P., and *Marinova T.,* 2013: Variations of thunderstorm activity in non-mountainous regions of Bulgaria (1961 – 2010). *BJMH 18*, 38-47.

Bocheva L. and *Simeonov P.,* 2015: Spatio-temporal variability of hailstorms for Bulgaria during the period 1961–2010. 15th International Multidisciplinary Scientific GeoConference SGEM 2015, ISBN 978-619-7105-38-4 / ISSN 1314-2704, June 18-24, 2015, Book4, 1065–1072.

Browning, K.A., 1977: The structure and mechanics of hailstorms, Hail: A Review of Hail Science and Hail Suppression. *Meteorol. Monogr., No 38*, Amer. Meteorol., Soc., 1–43.

Bunkers, M.J., 2002: Vertical wind shear associated with left-moving supercells. *Weather Forecast 17*, 845–855. https://doi.org/10.1175/1520-0434(2002)017<0845:VWSAWL>2.0.CO;2

Carbunaru, D.V., Burcea S., Sasu, M., Antonescu B., and *Bell, A.,* 2010: Three Body Scatter Signature climatology in Romania. ERAD 2010 - The sixth European conference on radar in meteorology and hydrology.

Davies-Jones, R., Burgess, D., and *Foste,r M.,* 1990: Test Of Helicity As A Tornado Forecast Parameter. Preprints, 16th Conf. on Severe Local Storms, Kananaskis Park, Alberta, Canada, Amer. Meteor. Soc., 588–592.

Dimitrova, Ts., Mitzeva, R., Pisarova, Y., Betz, H.D., and *Peneva, E.,* 2013: Relationship between lightning characteristics and radar estimated parameters during pre-severe and severe stages of hail producing thunderstorms developed over Bulgaria. 7th European Conference on Severe Storms (ECSS2013), 3–7 June, Helsinki, Finland.

Doswell, C.A. III and *Burgess, D.W.*, 1993: Tornadoes and tornadic storms: A review of conceptual models. In (Eds. *Church et al.*) The Tornado: Its Structure, Dynamics, Prediction, and Hazards Amer. Geophys. Union*, Geophys. Monogr. 79,* 161–172.

Dudhia, J., 1989: Numerical study of convection observed during the Winter Monsoon Experiment using a mesoscale two–dimensional model. *J. Atmos. Sci. 46*, 3077–3107.

https://doi.org/10.1175/1520-0469(1989)046<3077:NSOCOD>2.0.CO;2

Edwards, R. and *Thompson, R.*, 1998: Nationwide Comparisons of Hail Size with WSR-88D Vertically Integrated Liquid Water and Derived Thermodynamic Sounding Data, *Weather Forecast. 13*, 277–285.
https://doi.org/10.1175/1520-0434(1998)013<0277:NCOHSW>2.0.CO;2

Gospodinov, I., Dimitrova, Ts., Bocheva, L., Simeonov, P., and *Dimitrov, R.*, 2015: Derecho-like event in Bulgaria on 20 July 2011. *Atmos. Res. 158*, 254–273.
https://doi.org/10.1016/j.atmosres.2014.05.009

Grasso, L.D. and *Hilgendorf, E.R.,* 2001: Observations of a severe left moving thunderstorm. *Weather Forecast. 16*, 500–511.
https://doi.org/10.1175/1520-0434(2001)016<0500:OOASLM>2.0.CO;2

Hart, J.A., and *Korotky, W.* 1991: The SHARP workstation v1.50 users guide. National Weather Service, NOAA, U.S. Department of Commerce.

Holleman, I., 2008. Wind observations with Doppler weather radar. TECO-2008 — WMO Technical Conference on Meteorological and Environmental Instruments and Methods of Observation, St. Petersburg, Russian Federation, 27–29 November 2008.
http://www.wmo.int/pages/prog/www/IMOP/publications/IOM-96_TECO-2008/P1(28)_Holleman_Netherlands.pdf

House, R.A, Schmid, W., Fovell, R.G., and *Schiesser, H.,* 1993: Hailstorms in Switzerland: Left Movers, Right Movers, and False Hooks, *Month. Weather Rev. 121*, 3345–3370.
https://doi.org/10.1175/1520-0493(1993)121<3345:HISLMR>2.0.CO;2

Kain, J.S., 2004: The Kain–Fritsch convective parameterization: An update. *J. Appl. Meteor.*, 43, 170–181. https://doi.org/10.1175/1520-0450(2004)043<0170:TKCPAU>2.0.CO;2

Kalnay, E., Kanamitsu, M., Kistler, R., Collins, W., Deaven, D., Gandin, L., Iredell, M., Saha, S., White, G., Woollen, J., Zhu, Y., Chelliah, M., Ebisuzaki, W., Higgins, W., Janowiak, J., Mo K.C., Ropelewski, C., Wang, J., Leetmaa, A., Reynolds, R., Jenne, R., and *Joseph, D.,* 1996: The NCEP/NCAR Reanalysis 40-year Project. *Bull. Amer. Meteor. Sosc 77*, 437–471.
https://doi.org/10.1175/1520-0477(1996)077<0437:TNYRP>2.0.CO;2

Klemp, J. and *Wilhelmson, R.,* 1978: Simulations of right- and left-moving storms produced through storm splitting. *J. Atmos. Sci. 35*, 1097–1110.
https://doi.org/10.1175/1520-0469(1978)035<1097:SORALM>2.0.CO;2

Lemon L., 1998: The Radar ''Three-Body Scatter Spike'': An Operational Large-Hail Signature, *Weather Forecast. 13*, 327–340.
https://doi.org/10.1175/1520-0434(1998)013<0327:TRTBSS>2.0.CO;2

Lindsey, D.T., and *Bunkers, M.J.,* 2005: Observations of a severe, left-moving supercell on 4 May 2003. *Month. Weather Rev. 20*, 15–22. https://doi.org/10.1175/WAF-830.1

Lim, K.–S.S. and *Hong*, *S.–Y.,* 2010: Development of an effective double–moment cloud microphysics scheme with prognostic cloud condensation nuclei (CCN) for weather and climate models. *Month. Weather. Rev. 138*, 1587–1612. https://doi.org/10.1175/2009MWR2968.1

Manros K., Ortega K., and *Pietrycha A.*, 2010: Examining radar 'sidelobe spikes' for severe hail identification. https://ams.confex.com/ams/pdfpapers/175930.pdf

Mlawer, Eli. J., Steven. J. Taubman, Patrick. D. Brown, M.J. Iacono, and *S. A. Clough*, 1997: Radiative transfer for inhomogeneous atmospheres: RRTM, a validated correlated–k model for the longwave. *J. Geophys. Res. 102*, 16663–16682. https://doi.org/10.1029/97JD00237

NCEP, 2014: User's Guide for the ARW WRF Modeling System Version 3.5
http://www2.mmm.ucar.edu/wrf/users/docs/user_guide_V3.5/ARWUsersGuideV3.pdf

Nielsen-Gammon, J. and *Read, W.*, 1995: Detection and Interpretation of Left-Moving Severe Thunderstorms Using the WSR-88D: A Case Study, *Weather Forecast. 10*, 127–140.
https://doi.org/10.1175/1520-0434(1995)010<0127:DAIOLM>2.0.CO;2

Penchev R., Peneva E, 2013: Numerical simulation of extreme convective events during 2012 in Bulgaria using the weather forecast model WRF, Proceedings of the 2nd National Congress in Physical Sciences, 25-29 September 2013, Sofia (in Bulgarian)

http://optics.phys.uni-sofia.bg/disk_CONGRESS/html/pdf/S0751.pdf

Rasmussen, E.N., 2003: Refined supercell and tornado forecast parameters. *Weather Forecast. 18,* 530–535. https://doi.org/10.1175/1520-0434(2003)18<530:RSATFP>2.0.CO;2

Rasmussen, E.N., and *Blanchard, D.O.,* 1998: A Baseline Climatology Of Sounding-Derived Supercell And Tornado Forecast Parameters. *Weather Forecast. 13*, 1148–1164. https://doi.org/10.1175/1520-0434(1998)013<1148:ABCOSD>2.0.CO;2

Simeonov P., Bocheva L., and *Gospodinov I.,* 2013: On space-time distribution of tornado events in Bulgaria (1956-2010) with brief analyses of two cases. *Atmos.Res. 123*, 61–70. https://doi.org/10.1016/j.atmosres.2012.07.003

Viktor E., Reese S., and *Zimmerli P.,* 2015: Hail losses under the microscope - Comparing losses from three major hail events of the recent past. 8th European Conference on Severe Storms, 14-18 September 2015, Wiener Neustadt, Austria
http://meetingorganizer.copernicus.org/ECSS2015/ECSS2015-19.pdf

Weisman, M.L. and *Klemp, J.B.,* 1982: The dependence of numerically simulated convective storms on vertical wind shear and buoyancy. *Mon. Weather Rev. 110,* 504–520. https://doi.org/10.1175/1520-0493(1982)110<0504:TDONSC>2.0.CO;2

Weisman, M. L, and *Klemp, J.B.,* 1984: The structure and classification of numerically simulated convective storms in directionally varying wind shears. *Mon. Weather Rev. 112*, 2479–2498. https://doi.org/10.1175/1520-0493(1984)112<2479:TSACON>2.0.CO;2

Weisman, M.L. and *Klemp, J.B.,* 1986: Characteristics of isolated convective storms. In (Ed. *P.S. Ray*) Mesoscale Meteorology and Forecasting. Amer. Meteor. Soc., 331–358 https://doi.org/10.1007/978-1-935704-20-1_15

Zamfirov I., Georgiev Ch.G., and *Stotanova, J.,* 2014: Case study of two splitting hailstorms over Bulgaria on 20 May 2013. ERAD 2014 – The Eight European Conference on Radar in Meteorology and Hydrology.
http://www.pa.op.dlr.de/erad2014/programme/ExtendedAbstracts/053_Zamfirov.pdf

Zrnić, D., 1987: Three-body scattering produces precipitation signature of special diagnostic value. *Radio Sci. 22*, 76–86. http://ready.arl.noaa.gov/READYamet.php

IDŐJÁRÁS

Parametric or non-parametric: analysis of rainfall time series at a Hungarian meteorological station

Tímea Kocsis[1*] and **Angéla Anda**[2]

[1] *Budapest Business School College of Commerce,*
Catering and Tourism Department of Methodology,
Alkotmány Str. 9-11, H-1054 Budapest, Hungary

[2] *University of Pannonia Georgikon*
Faculty Department of Meteorology and Water Management,
Festetics Str. 7. H-8360 Keszthely,Hungary

*Corresponding author E-mail: JakuschneKocsis.Timea@uni-bge.hu

Abstract— Parametric methods (linear trend, t-test for slope) for analyzing time series are the simplest methods to get insight to the changes in a variable over time. These methods have a requirement for normal distribution of the population that can be a limit for application. Non-parametric methods are distribution-free methods, and investigators can have a more sophisticated view to the variable tendencies in time series. 144-year-long time series of precipitation data measured at the meteorological station in Keszthely, Hungary (latitude: 46°44′, longitude: 17°14′, elevation: 124 m above Baltic sea level) were analyzed by Mann-Kendall trend test for detecting tendencies in the time series. Sen's slope estimator was applied to estimate the slope of the linear changes. In average, 44 mm decline can be shown for 100 years in the annual sum, 29.7 mm and 25.7 mm in the precipitation sum of spring and autumn (in 100 years), respectively. The rainfall sum of winter increased by 15.4 mm. Sums of April, May, and October declined by 10.8 mm, 13 mm, and 20.9 mm, respectively, according to one-tailed Mann-Kendall tests. These results were compared to the previous results of the authors carried out by parametric methods. Results of two-tailed tests of parametric and non-parametric methods are easily comparable. Parametric method (linear trend) proved significant decreasing tendencies for spring, April, and October. Non-parametric Mann-Kendall tests show significant declining tendencies for spring, autumn, and October.

Key-words: Kendall's tau, Mann-Kendall trend test, Sen's slope estimator, precipitation changes, Keszthely, Hungary

1. Introduction

Climate change is one of the problems that mankind should face in the 21st century. According to the last *IPCC* report (2013), human role in the process has no doubt (95% is the probability that human influence has been dominant on the present changes of climate system). Climate change will probably affect all parts of the Earth, and in the center of Europe, the Carpathian Region will be influenced as well. In some cases, the volume and direction of the changes in climate model simulations are uncertain. Hydrological cycle is an element of the climate system that is expected to change, and the signs of these amendments can already be detected. Precipitation in average over mid-latitude land areas of the Northern Hemisphere has increased from 1901 (medium confidence) according to *IPCC* AR5 (2013). Heavy precipitation events and increase in intensity and frequency of rainfall are very likely (90% probability) over mid-latitude land masses (*IPCC*, 2013). Precipitation strongly influences the water cycle from local to global scales. Any modification in the amount or distribution of rainfall has significant impact on the water availability, and therefore, water management. Hungary, which occupies the middle of the Carpathian-Basin, has long-experienced significant temporal and spatial variations in precipitation. In recent decades, due to the hardships faced by the state complying with decreasing rainfall amount, studies related to precipitation events are extremely beneficial.

The prediction of the effects of climate change on the Carpathian Region (including Hungary) requires regional climate scenarios with adequate temporal and spatial resolution, capable of translating global phenomena to a local scale. *Bartholy et al*. (2004) applied regional models to estimate the regional effects of climate change in the Balaton Lake – Sió Canal catchment area, using ECHAM/GCM outputs. This catchment area (which also includes Keszthely meteorological station) is one of the most vulnerable regions in Hungary because of its economical and touristic importance and unique treasure of nature. According to *Bartholy et al.* (2005), the amount of precipitation will decline by 25–35% in the summer half-year and by 0–10% in the winter half-year on the Balaton Lake – Sió Canal catchment area. The regional model runs for the Carpathian Basin (RCMs) using the A2 and B2 global emission scenarios of the *IPCC AR4* (2007), expect more than 2.5 and less than 4.8 °C temperature rise for all seasons and both scenarios (*Bartholy et al*., 2007). A 20–33% decrease in precipitation is predicted for the summer half-year and there is high uncertainty for the rainfall for the winter half-year (*Bartholy et al*., 2007). The earlier results of the authors harmonizes with their latest projection carried out in the PRUDENCE European Project's model application (*Bartholy et al.,* 2009). These statements were enhanced by *Bartholy et al.* (2008) and by the Hungarian Meteorological Service (*OMSZ*, 2010) according to further regional climate model simulations. *Pongrácz et al.* (2011) and *Kis et al.* (2014) communicated similar results for projection of the future climate in Hungary. *Pongrácz et al.* (2014) project significant increase in drought-related indices in summer by the end of the 21st

century. *Bartholy et al.* (2015) examined precipitation indices and project that frequency of extreme precipitation will increase in Central Europe, except of summer, when decreasing tendency is very likely. For the tendencies of the past, *Szalai et al.,* (2005) stated that the annual precipitation amount decreased by 11% between 1901 and 2004, according to the analysis of the Hungarian Meteorological Service. The biggest decline could be experienced in spring; it was 25% for the above mentioned period. *Bodri* (2004) suggested that slow decrease of precipitation with a noticeable increase in precipitation variability are characteristic for the 20th century. While the northern and western part of Europe gets more precipitation in parallel with the warming tendency, Hungary, similarly to the region of the Mediterranean Sea, gets less rainfall. The water balance has deficit, since the difference between water income and outflow is increasing. Between 1901 and 2009, the highest precipitation decline over the territory of Hungary occurred in the spring, nearly 20% (*Lakatos* and *Bihari,* 2011). *Bartholy* and *Pongrácz* (2005, 2007, 2010) examined several precipitation extreme indices and suggested that regional intensity and frequency of extreme precipitation increased in the Carpathian Basin in the second half of the last century, while the total precipitation decreased.

The goal of this study is to analyze the long-term data series of the meteorological measurements of precipitation amount at the meteorological station at Keszthely, Trans-Danubia, Hungary (N 46°44', E 17°14', *Fig. 1*) from the point of view of climate and statistics. Our aim is to analyze the dataset by non-parametric methods and compare the results to our previous findings derived from parametric time series analyses. A non-parametric method, the Mann-Kendall trend test, that was applied in this research, is widespread for analyzing meteorological (such as precipitation sums) and hydrological data. The Sen's slope estimator was applied as non-parametric method for determining the slope of the tendencies.
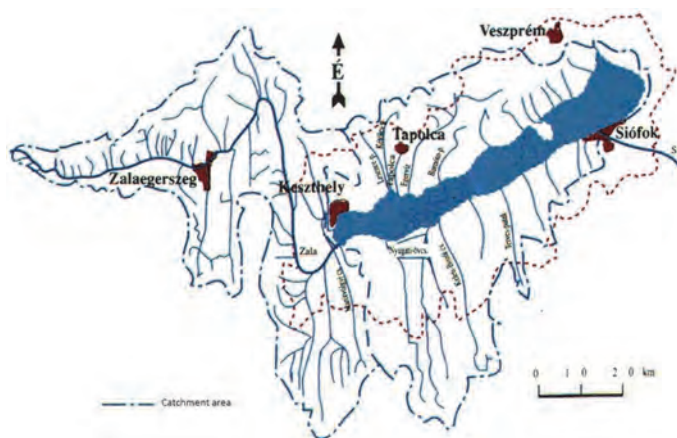
Fig. 1. Catchment area of the Balaton Lake.
(source: website of the Hungarian Water Inspectorate)

Several examples can be found in the literature for application of the Mann-Kendall trend test, e.g., *Patle* and *Libang* (2014) argued on trend analysis of annual and seasonal rainfall the northeastern region of India, *Salmi et al.* (2002) analyzed the trends of atmospheric pollutants in Finnland. Meteorological applications can be read in *Rahman* and *Begum* (2013), who determined trends of rainfall of the largest island in Bangladesh. *Ganguly et al.* (2015) investigated the tendencies of rainfall in Himachal Pradesh (state in North India) between 1950 and 2005. *Gavrilov et al.* (2015a, 2015b, 2016) examined trends of air temperature by Mann-Kendall test in Vojvodina, Serbia. *Salami et al.* (2014) applied this non-parametric trend test for the analysis of hydro-meteorological variables in Nigeria. *Mapurisa* and *Chikodzi* (2014) made an assessment of trends of monthly and seasonal rainfall in Southeast Zimbabwe. *Karmeshu* (2012) investigated the temperature- and precipitation changes in the northeastern part of United States. Hydrological utilization is given by *Hamed* (2008). *Burn* and *Hag Elnur* (2002) estimated the trends and variability of 18 hydrological variables by Mann-Kendall trend test. *Hirsch et al.* (1991) used the method for investigation of stream water quality.

2. Data and methods

Monthly amounts of precipitation were analyzed from 1871 to 2014 measured at the beginning in the territory of the ancient Georgikon Academy of Agriculture at Keszthely, then at the meteorological station of the Hungarian Meteorological Service. The dataset was provided by the Department of Meteorology and Water Management of University of Pannonia Georgikon Faculty (Keszthely). This dataset is special, because few stations in Hungary have continuous measurements of more than 140 years with detailed historical background (*Kocsis* and *Anda,* 2006). The dataset was analyzed in three sessions: annual amounts, seasonal amounts and monthly precipitation sums. Seasons of temperate climate were performed as common in meteorology, e.g., spring: March, April, May, etc.

2.1. The Mann-Kendall trend test

Mann-Kendall trend test is widespread in climatological and hydrological time series analysis, because it is simple and robust, it can cope with missing values and values under detection limit (*Gavrilov et al.*, 2016). This non-parametric test is commonly used to detect monotonic tendencies in series of environmental data, too (*Pohlert,* 2016). This method has no requirement for the distribution of the population, as the regression method has a requirement for normal distribution. No assumption of the normality is required (*Helsel* and *Hirsh*, 2002). *Hirsch et al.* (1982) and *Hirsch* and *Slack* (1984) developed the method and introduced seasonal Mann-Kendall test for data that are serially dependent. *Hamed* and *Rao*

(1998) developed a modified Mann-Kendall test for autocorrelated data. *Yue et al.* (2002) investigated the power of the Mann-Kendall test in hydrological series.

The Mann-Kendall trend test is based upon the work of *Mann* (1945) and *Kendall* (1975), and is closely related to the Kendall's rank correlation coefficient. The methodology is introduced following the detailed descriptions given by *Gilbert* (1987) and *Hipel* and *McLeod* (1994) as follows:

In case of determining the presence of monotonic trend in a time series, the null hypothesis (H0) of the Mann-Kendall test is that the data come from a population where random variables are independent and identically distributed. The alternative hypothesis (Ha) is that the data follow a monotonic trend over time. The Mann-Kendall test statistic is given as

$$S = \sum_{k=1}^{n-1} \sum_{j=k+1}^{n} sign(x_j - x_k), \qquad (1)$$

where $j > k$, and

$$sign(x) = \begin{cases} +1, x > 0 \\ 0, x = 0 \\ -1, x < 0 \end{cases} . \qquad (2)$$

Kendall (1975) proved that S is asymptotically normally distributed with the following parameters (mean and variance):

$$E[S] = 0$$
$$Var[S] = \{n(n-1)(2n+5) - \sum_{j=1}^{p} tj(tj-1)(2tj+5)\}/18, \qquad (3)$$

where p is the number of the tied groups in the data set, tj is the number of data in the jth tied group, and n is the number of data in the time series.

Positive value of S means that there is an increasing trend, negative value of S means the opposite, there is a decreasing trend with time. It was proven that if the number of data is above 10, the standard normal variate Z can be used for hypothesis test:

$$Z = \begin{cases} \frac{S-1}{[Var(S)]^{1/2}}, if\ S > 0 \\ 0, if\ S = 0 \\ \frac{S+1}{[Var(S)]^{1/2}}, if\ S < 0 \end{cases} . \qquad (4)$$

During the hypothesis test, α=5% significance level was used in the two-tailed and one-tailed tests as well, and statistical significance was determined. S is closely related to the Kendall's rank correlation coefficient (τ):

$$\tau = \frac{S}{D},\qquad(5)$$

where D is the possible number of data pairs from n members of the dataset:

$$D = \binom{n}{2}.\qquad(6)$$

After detecting the non-parametric trend, the Sen's slope estimator was applied. This is a non-parametric method that can calculate the change per time unit (direction and volume). Detailed description of the method is given by *Sen* (1968). Not only the value of the slope, but also the confidence interval was estimated under $1-\alpha=95\%$ probability level.

SPSS 17.0 and Addinsoft's *XLSTAT* (2016) was used for carrying out the computations.

3. Results

Our previous studies focused on linear trend approximation for analyzing the long-time series of precipitation measured at Keszthely station (Hungary) (*Kocsis,* 2008; *Kocsis* and *Anda,* 2016). Results are summarized in *Table 1.* It can be stated that statistically significant changes could be detected by linear regression method with parametric test for the slope by two-tailed t-test for spring, and among the monthly data of April and October. *Table 2* presents that the requirements for the normal distribution for the population are fulfilled, tested by the Kolmogorov-Smirnov test for distribution. However, in some cases (February, March, July, and November), the distribution cannot be accepted as normal distribution according to p-value (α=5%). For this reason, non-parametric methods were used to analyze all the data set (annual sums, seasonal and monthly sums).

Table 1. Summary of the previous findings using linear trend and two tailed t-test for testing the significance of the slope

	Significant tendency in 100 years		
	1871–2000 (*Kocsis,* 2008)	1871–2010 (*Kocsis,* 2015)	1871–2014 (*Kocsis* and *Anda,* 2016)
Changes in annual sum	none	none	none
Changes in seasonal sums	Spring (–35 mm)	Spring (–29 mm)	Spring (–31.5 mm)
Changes in monthly sums	October (–26 mm)	October (–25 mm)	April (–14 mm) and October (–23.5 mm)

Table 2. Results of the test of normal distribution

Distribution (Kolmogorov-Smirnov test)		
H0: The sample follows a normal distribution		
Ha: The sample does not follow a normal distribution		
	Hypothesis accepted at α=5%	p-value
Annual sum	H0	35.2%
Spring	H0	42.1%
Summer	H0	80.0%
Autumn	H0	53.1%
Winter	H0	91.0%
January	H0	34.7%
February	*Ha*	4.7%
March	*Ha*	3.6%
April	H0	5.3%
May	H0	28.6%
June	H0	75.2%
July	*Ha*	2.5%
August	H0	25.6%
September	H0	47.4%
October	H0	5.7%
November	*Ha*	3.1%
December	H0	7.1%

As the first step, the Kendall's tau rank correlation coefficient was determined to show the sign of the relationship between time and the variables. Tau was first tested by the two-tailed test (*Table 3*). Significance level was stated at $\alpha=5\%$. In two-tailed tests, p-values proved significant negative relationships for spring, autumn, and among the monthly sums, for October. P-values of some other monthly sums were near to the limit, so one-tailed tests according to the sign of Kendall's tau were also used. P-values in one-tailed tests show the presence of negative relationship in the annual sum, precipitation sums in spring, autumn, April, May, and October, and positive relationship for the winter (*Table 3*).

Table 3. Values of Kendall's rank correlation coefficient and their significance

	Kendall τ	Two-tailed test (τ≠0) p-value	One-tailed test (τ<0 or τ>0) p-value
		*significant at α=5%	
Annual sum	−0.096	8.9%	**4.5%***
Spring	−0.159	**0.5%***	**0.2%***
Summer	−0.036	51.9%	26.0%
Autumn	−0.112	**4.6%***	**2.3%***
Winter	0.096	8.8%	**4.4%***
January	0.042	45.2%	22.6%
February	0.063	26.1%	13.0%
March	−0.054	33.9%	16.9%
April	−0.107	5.7%	**2.8%***
May	−0.104	6.4%	**3.2%**
June	0.01	86.3%	43.1%
July	−0.018	74.4%	37.2%
August	−0.042	45.3%	22.7%
September	−0.054	33.4%	16.7%
October	−0.153	**0.7%***	**0.3%***
November	0.012	83.4%	41.7%
December	0.061	27.7%	13.9%

Based on the Kendall's tau (τ), the Mann-Kendall trend test was used to detect monotonic trends in the time series. First two-tailed (*Table 4*) and then one-tailed z-tests were applied according to the sign of the calculated S value, respectively (*Table 5*). Decision about the statistical significance was made using

empirical significance level (p-value) compared to α=5%. The two-tailed Mann-Kendall test (with the alternative hypothesis that there is no trend in the time series) gave significant result for spring, autumn, and October in concordance with the results for the tests for τ. Seasonally in spring and autumn, while among the months, in October the presence of significant monotonic trend could be found. One-tailed tests have an alternative hypothesis, that in the time series, a negative/positive trend is present according to the sign of computed S statistics, respectively. These tests gave the results in accordance to the one-tailed tests for τ, as S and τ statistics are related. According to p-values, significant declining trend can be experienced in the annual sum, precipitation sums in spring, autumn, April, May, and October, and increasing trend can be shown for the winter.

Table 4. Results of the two-tailed Mann-Kendall trend test

Mann–Kendall trend test (two-tailed) H0: There is no trend in the series *Ha: There is a trend in the series*		
	Hypothesis accepted at α=5%	**p-value**
Annual sum	H0	9.0%
Spring	*Ha*	0.5%
Summer	H0	52.1%
Autumn	*Ha*	4.6%
Winter	H0	8.8%
January	H0	45.3%
February	H0	26.1%
March	H0	33.9%
April	H0	5.7%
May	H0	6.4%
June	H0	86.4%
July	H0	74.5%
August	H0	45.4%
September	H0	33.5%
October	*Ha*	0.7%
November	H0	83.6%
December	H0	27.8%

Table 5. Results of the one-tailed Mann-Kendall trend test

Mann-Kendall trend test (one-tailed)		
H0: There is no trend in the series		
Ha: There is a positive or negative trend according to the sign of S		
Hypothesis accepted at α=5%	**p-value**	**S**
Annual sum	*Ha*	4.5%	−983
Spring	*Ha*	0.2%	−1633
Summer	H0	26.0%	−373
Autumn	*Ha*	2.3%	−1154
Winter	*Ha*	4.4%	988
January	H0	22.7%	435
February	H0	13.1%	651
March	H0	17.0%	−554
April	*Ha*	2.8%	−1103
May	*Ha*	3.2%	−1073
June	H0	43.2%	100
July	H0	37.3%	−189
August	H0	22.7%	−434
September	H0	16.8%	−559
October	*Ha*	0.3%	−1568
November	H0	41.8%	121
December	H0	13.9%	629

The Sen's slope estimator was used to determine the slope of the trend (linear change per time unit). Confidence interval is also given for the slope. This interval contains the real value of the slope of the tendency in the population by the probability of 95% (*Table 6*). According to the one-tailed Mann-Kendall test, the decreasing tendencies are the follows for 100 years on average: the annual sum decreased by 44 mm, the precipitation sum of spring and autumn declined by 29.7 mm and 25.7 mm, respectively. The rainfall sum of winter increased by 15.4 mm. Sums of April, May, and October declined by 10.8 mm, 13 mm, and 20.9 mm, respectively.

Table 6. Values of the Sen's slope and their confidence interval

	Sen' slope	Lower	Upper
		boundary of the confidence interval at 1–α=95% probability level	
Annual sum	–0.444	–0.703	–0.207
Spring	–0.3	–0.396	–0.2
Summer	–0.095	–0.231	0.046
Autumn	–0.26	–0.38	–0.148
Winter	0.156	0.075	0.23
January	0.028	0	0.063
February	0.047	0.008	0.089
March	–0.043	–0.082	0
April	–0.109	–0.163	–0.059
May	–0.131	–0.192	–0.067
June	0.013	–0.063	0.08
July	–0.022	–0.098	0.036
August	–0.068	–0.139	0.011
September	–0.074	–0.13	–0.002
October	–0.211	–0.274	–0.144
November	0.012	–0.041	0.073
December	0.05	0.005	0.095

4. Discussion

Parametric methods (linear trend, t-test for slope) for analyzing time series are the simplest methods to get insight to the changes of a variable over time. These methods have a requirement for normal distribution of the population that can be a limit for application. Non-parametric methods are distribution-free methods, and researchers can have a more sophisticated view to the changing tendencies. Our previous results can be accepted, but the Mann-Kendall trend test proved other signs of precipitation changes at the examined meteorological station. One-tailed Mann-Kendall trend tests gave the evidence that decreasing tendencies can be statistically proven in the annual sum by 44 mm for 100 years on average, in the precipitation sum of spring and autumn by 29.7 mm and 25.7 mm, respectively. The rainfall sum of winter increased by 15.4 mm. Sums of April, May, and

October declined by 10.8 mm, 13 mm, and 20.9 mm, respectively. These results are parallel to the literature in the direction of the precipitation changes, but are not clearly in accordance regarding the volume of the changes estimated for the region of the examined meteorological station (Keszthely, Trans-Danubia, Hungary). Results of two-tailed tests of previous parametric and recent non-parametric methods are easily comparable. Parametric method (linear trend) proved significant tendencies for spring, April, and October (deceasing tendencies). Two-tailed non-parametric Mann-Kendall trend tests show significant tendencies for spring, autumn, and October (declining trends). Advantage of the non-parametric methods, that is fewer requirements for application, and the results derived from this research are more consistent with the literature. Declining tendencies of precipitation sums in spring and autumn possibly have unfavorable effect on the water-budget of the soil and Balaton Lake.

References

Barhtoly, J. and *Pongrácz, R.* 2005: Extremes of ground-based and satellite measurements in the vegetation period for the Carpathian Basin. *Phys. Chem. Earth 30*, 81–89. https://doi.org/10.1016/j.pce.2004.08.012

Barhtoly, J. and *Pongrácz, R.* 2007: Regional analysis of extreme temperature and precipitation indices for the Carpathian Basin from 1946 to 2001. *Glob. Planet. Change 57*, 83–95. https://doi.org/10.1016/j.gloplacha.2006.11.00

Bartholy, J., Mika, J., Pongrácz, R., and *Schlanger, V.* 2005: A globális felmelegedés éghajlati sajátosságai a Kárpát-medencében. In (ed.: *Takács-Sánta A.*) Éghajlatváltozás a világban és Magyarországon. Budapest. 105–139. (in Hungarian)

Bartholy, J. and *Pongrácz, R.,* 2010: Analysis of precipitation conditions for the Carpathian Basin based on extreme indices in the 20th century and climate simulation for 2050 and 2100. *Phys. Chem. Earth 35*, 43–51. https://doi.org/10.1016/j.pce.2010.03.011

Bartholy, J., Pongrácz, R., and *Gelybó, Gy.,* 2007: Regional climate change in Hungary for 2071–2100. *Appl. Ecol. Environ. Res. 5*, 1–17. https://doi.org/10.15666/aeer/0501_001017

Bartholy, J., Pongrácz, R., Gelybó, Gy., and *Szabó, P.,* 2008. Analysis of expected climate change in the Carpathian Basin using the PRUDENCE results. *Időjárás 112*, 249–264.

Bartholy, J., Pongrácz, R., Gelybó, Gy., and *Szabó, P.* 2009: Analysis of expected climate change in the Carpathian Basin using the PRUDENCE results. *Időjárás Special Issue 112 (3-4)*: 249-265

Bartholy, J., Pongrácz, R., and *Kis, A.* 2015: Projected changes of extreme precipitation using multi-model approach. *Időjárás 119*. 129–142.

Bartholy, J., Pongrácz, R., Matyasovszky, I., and *Schlanger, V.* 2004. A XX. Században bekövetkezett és a XXI. századra várható éghajlati tendenciák Magyarország területére. *AGRO-21 Füzetek 33*, 3–18. (in Hungarian)

Bodri, L., 2004: Tendencies in variability of gridded temperature and precipitation in Hungary (during the period of instrumental record). *Időjárás 108,* 141–153.

Burn, D.H. and *Hag Elnur M.A.,* 2002: Detection of hydrological trends and variability. *J. Hydrol 255*, 107–122. https://doi.org/10.1016/S0022-1694(01)00514-5

Ganguly, A., Chaudhuri, R.R., and *Sharma, P.,* 2015: Analysis of trend of the precipitation data: a case study of Kangra District, Himachal Pradesh. *Int. J. Res. – Granthaalayah 3 (9)*: 87–95.

Gavrilov, M.B., Markovic, S.B., Janc, N., Nikolic, M., Valjarevic, A., Komac, B., Zorn, M., Punisic, M., and *Bacevic, N.* 2015a: Assessing average annual air temperature trends using Mann-Kendall test in Kosovo. *Acta Geographica Slovenica 58,* 7–25. https://doi.org/10.3986/AGS.1309

Gavrilov, M.B., Markovic, S.B., Jarad, A., and *Korac, V.M.,* 2015b: The analysis of temperature trends in Vojvodina (Serbia) from 1949 to 2006. *Thermal Sci. 19 Suppl. 2:* S339–S350. https://doi.org/10.2298/TSCI150207062G

Gavrilov, M.B., Tosic, I., Markovic, S.B., Unkasevic, M., and *Petrovic, P.,* 2016: Analysis of annual and seasonal temperature trends using the Mann- Kendall test in Vojvodina, Serbia. *Időjárás 120,* 183–198.

Gilbert, R.O., 1987: Statistical Methods for Environmental Pollution Monitoring. Van Nostrand Reinhold Company, NY, USA. 208–224.

Hamed, K.H., 2008: Trend detection in hydrological data: The Mann-Kendall trend test under the scaling hypothesis. *J. Hydrol. 349,* 350–363. https://doi.org/10.1016/j.jhydrol.2007.11.009

Hamed, K.H. and *Rao, A.R.,* 1998: A modified Mann-Kendall trend test for autocorrelated data. *J. Hydrol. 204,* 182–196. https://doi.org/10.1016/S0022-1694(97)00125-X

Helsel, D.R. and *Hirsh, R.M.,* 2002: Trend analysis. In Techniques of Water-Resources Investigations of the United States Geological Survey Book 4, Hydrologic Analysis and Interpretation Chapter A3: Statistical Methods in Water Resources. Chapter 12: 327.

Hipel, K.W. and *McLeod, A.I.,* 1994: Time series modelling of water resources and environmental systems. Elsevier, Amsterdam, The Netherlands. 864–866, 924–925.

Hirsch, R.M., Alexander, R.B., and *Smith, R.A.,* 1991: Selection of methods for the detection and estimation of trends in water quality. *Water Resour. Res. 27,* 803–813. https://doi.org/10.1029/91WR00259

Hirsch, R.M. and *Slack, J.R.,* 1984: A nonparametric trend test for seasonal data with serial dependence. *Water Resour. Res. 20,* 727–732. https://doi.org/10.1029/WR018i001p00107

Hirsch, R.M., Slack, J.R., and *Smith, R.A.* 1982: Techniques of trend analysis for monthly water quality data. *Water Resour. Res. 18,* 107–121.

IPCC 2007: Summary for Poicymakers. In (Eds.: Solomon, S., D. Qin, M. Manning, Z. Chen, M. Marquis, K.B. Averyt, M.Tignor and H.L. Miller) Climate Change 2007: The Physical Science Basis. Contribution of Working Group I to the Fourth Assessment Report of the Intergovernmental Panel on Climate Change Cambridge University Press, Cambridge, United Kingdom and New York, NY, USA, www.ipcc.ch: 5, 7.

IPCC 2013: Summary for Policymakers. In (Eds.: *Stocker, T.F., D. Qin, G.-K. Plattner, M. Tignor, S.K. Allen, J. Boschung, A. Nauels, Y. Xia, V. Bex* and *P.M. Midgley*) Climate Change 2013: The Physical Science Basis. Contribution of Working Group I to the Fifth Assessment Report of the Intergovernmental Panel on Climate Change Cambridge University Press, Cambridge, United Kingdom and New York, NY, USA.

Karmeshu, N., 2012: Trend detection in annual temperature and precipitation using the Mann-Kendall Test – A case study to assess climate change on select states in the Northeastern United States. MSc Thesis, University of Pennsylvania.

Kendall, M.G., 1975: Rank correlation methods. Charles Griffin, London.

Kis, A., Pongrácz, R., and *Bartholy, J.,* 2014: Magyarországra becsült csapadéktrendek: hibakorrekció alkalmazásának hatása. *Légkör 59,* 117–120. (in Hungarian)

Kocsis, T., 2008: Az éghajlatváltozás detektálása és hatásainak modellezése, PhD Thesis.

Kocsis, T., 2015: A keszthelyi csapadékösszegek éghajlat-statisztikai jellemzése 1871-2010 között. 10. Magyar Ökológus Kongresszus, Veszprém. (in Hungarian)

Kocsis, T. and *Anda, A.,* 2006: A keszthelyi meteorológiai megfigyelések története. Published by University of Pannonia Georgikon Faculty, Keszthely ISBN 963 9639 07 9 (

Kocsis, T. and *Anda, A.,* 2017: Analysis of precipitation time series at Keszthely, Hungary (1871–2014). *Időjárás 121,* 63–87.

Lakatos, M. and *Bihari, Z.* 2011: Temperature- and precipitation tendencies observed in the recent past. In (Eds.: *Bartholy, J., Bozó, L., Haszpra, L.*) Klímaváltozás 2011. 159–169. (in Hungarian)

Mann, H.B., 1945: Nonparametric tests against trend. *Econometrica 13*, 245–259. https://doi.org/10.2307/1907187

Mapurisa, B. and *Chikodzi, D.,* 2014: An assessment of trends of monthly contributions to seasonal rainfall in South-Eastern Zimbabwe. *Amer. J. Climate Change 3*, 50–59. https://doi.org/10.4236/ajcc.2014.31005

OMSZ, 2010: Klímamodellezési tevékenység – Eredmények (2010). OMSZ. (inHungarian)

Patle, G.T. and *Libang, A.,* 2014: Trend analysis of annual and seasonal rainfall to climate variability in North-East region of India. *J. Appl. Nat. Sci. 6,* 480–483. https://doi.org/10.31018/jans.v6i2.486

Pohlert, T. 2016: Non-parametric trends and change-point detection. https://cran.r-project.org/web/packages/trend/vignettes/trend.pdf

Pongrácz, R., Bartholy, J., and *Kiss, A.,* 2014: Estimation of future precipitation conditions for Hungary with special focus on dry periods. *Időjárás 118,* 305–321.

Pongrácz, R., Bartholy, J., and *Miklós, E.,* 2011: Analysis of projected climate change for Hungary using ENSEMBLES simulations. *Appl. Ecol. Environ. Res. 9,* 387–398. https://doi.org/10.15666/aeer/0904_387398

Rahman, A. and *Begum, M.,* 2013: Application of non-parametric test for trend detection of rainfall in the largest island of Bangladesh. *ARPN J. Earth Sci. 2 (2),* 40–44.

Salami, A.W., Mohammed, A.A., Abdulmalik, Z.H., and *Olanlokun, O.K.,* 2014: Trend analysis of hydro-meteorological variables using the Mann-Kendall trend test: application to the Niger River and the Benue sub-basins in Nigeria. *Int.l J. Technol. 2,* 100–110. https://doi.org/10.14716/ijtech.v5i2.406

Salmi, T., Maatta, A., Anttila, P., Ruoho-Airola, T., and *Amnell, T.* 2002: Detecting trends of annual values of atmospheric pollutants by the Mann-Kendall test and Sen's slope estimates – the Excel template application makesens. Finnish Meteorological Institute, Helsinki, Finland

Sen, P.K., 1968: Estimates of the regression coefficient based on Kendall's tau. *J. Amer. Statistic. Assoc. 63 (324),* 1379–1389. https://doi.org/10.1080/01621459.1968.10480934

SPSS 17.0: Statisctics, IBM Software, USA.

Szalai, S., Bihari, Z, Lakatos, M., and *Szentimrey, T.,* 2005: Magyarország éghajlatának néhány jellemzője 1901-től napjainkig. OMSZ. (in Hungarian)

Website of the Hungarian Water Inspectorate https://www.vizugy.hu/index.php?module=content&programelemid=42

XLSTAT 2016: Addinsoft https://www.xlstat.com/en/

Yue, S., Pilon, P., and *Cavadias, G.,* 2002: Power of the Mann-Kendall and Spearman's rho test for detecting monotonic trends in hydrological series. *J. Hydrol. 259,* 254–271. https://doi.org/10.1016/S0022-1694(01)00594-7

INSTRUCTIONS TO AUTHORS OF *IDŐJÁRÁS*

The purpose of the journal is to publish papers in any field of meteorology and atmosphere related scientific areas. These may be

- research papers on new results of scientific investigations,
- critical review articles summarizing the current state of art of a certain topic,
- short contributions dealing with a particular question.

Some issues contain "News" and "Book review", therefore, such contributions are also welcome. The papers must be in American English and should be checked by a native speaker if necessary.

Authors are requested to send their manuscripts to

Editor-in Chief of IDŐJÁRÁS
P.O. Box 38, H-1525 Budapest, Hungary
E-mail: journal.idojaras@met.hu

including all illustrations. MS Word format is preferred in electronic submission. Papers will then be reviewed normally by two independent referees, who remain unidentified for the author(s). The Editor-in-Chief will inform the author(s) whether or not the paper is acceptable for publication, and what modifications, if any, are necessary.

Please, follow the order given below when typing manuscripts.

Title page should consist of the title, the name(s) of the author(s), their affiliation(s) including full postal and e-mail address(es). In case of more than one author, the corresponding author must be identified.

Abstract: should contain the purpose, the applied data and methods as well as the basic conclusion(s) of the paper.

Key-words: must be included (from 5 to 10) to help to classify the topic.

Text: has to be typed in single spacing on an A4 size paper using 14 pt Times New Roman font if possible. Use of S.I.

units are expected, and the use of negative exponent is preferred to fractional sign. Mathematical formulae are expected to be as simple as possible and numbered in parentheses at the right margin.

All publications cited in the text should be presented in the *list of references*, arranged in alphabetical order. For an article: name(s) of author(s) in Italics, year, title of article, name of journal, volume, number (the latter two in Italics) and pages. E.g., *Nathan, K.K.,* 1986: A note on the relationship between photosynthetically active radiation and cloud amount. *Időjárás 90,* 10–13. For a book: name(s) of author(s), year, title of the book (all in Italics except the year), publisher and place of publication. E.g., *Junge, C.E.,* 1963: *Air Chemistry and Radioactivity.* Academic Press, New York and London. Reference in the text should contain the name(s) of the author(s) in Italics and year of publication. E.g., in the case of one author: *Miller* (1989); in the case of two authors: *Gamov* and *Cleveland* (1973); and if there are more than two authors: *Smith et al.* (1990). If the name of the author cannot be fitted into the text: *(Miller,* 1989); etc. When referring papers published in the same year by the same author, letters a, b, c, etc. should follow the year of publication. DOI numbers of references should be provided if applicable.

Tables should be marked by Arabic numbers and printed in separate sheets with their numbers and legends given below them. Avoid too lengthy or complicated tables, or tables duplicating results given in other form in the manuscript (e.g., graphs). *Figures* should also be marked with Arabic numbers and printed in black and white or color (under special arrangement) in separate sheets with their numbers and captions given below them. JPG, TIF, GIF, BMP or PNG formats should be used for electronic artwork submission.

More information for authors is available: journal.idojaras@met.hu